Distribution of Windblown Sediment in Small Craters on Mars

by

Rebekah Kienenberger

A Thesis Presented in Partial Fulfillment
of the Requirements for the Degree
Master of Science

Approved April 2011 by the
Graduate Supervisory Committee:

Ronald Greeley, Chair
Kelin Whipple
Philip Christensen

ARIZONA STATE UNIVERSITY

May 2011

ABSTRACT

Many shallow craters near the Spirit Mars Exploration Rover landing site contain asymmetric deposits of windblown sediments which could indicate the predominant local wind direction at the time of deposition or redistribution. Wind tunnel simulations and field studies of terrestrial craters were used to determine trends in deposition as a function of crater morphometry and wind direction. Terrestrial analog field work at the Amboy lava field, Mojave Desert, California, included real-time wind measurements and assessments of active sediment deposition in four small (<100 m) craters. Preliminary results indicate that reverse flow or stagnant wind and deposition on the upwind side of the crater floor occurs in craters with depth-to-diameter (d/D) ratios ≥0.05. Measurements taken within a crater of d/D of ~0.02 do not indicate reverse flow. Therefore, reverse flow is expected to cease within a d/D range of 0.02 to 0.05, resulting in wind movement directly over the crater floor in the downwind direction with no asymmetric sediment deposition. Wind tunnel simulations using six crater models, including a scaled model of a crater from the Amboy lava field, were completed to assess the wind flow in and around craters as a function of crater morphometry (depth, diameter). Reverse flow occurred in craters with d/D ratios ≥0.033, resulting in sediment deposition in the upwind portion of the crater floor. Visual observations of a crater with a d/D of ~0.020 did not indicate reverse flow, similar to the results of field studies; therefore, reverse flow appears to cease within a d/D range of 0.020 to 0.033. Craters with asymmetric aeolian deposits near the Mars Spirit landing site have d/D ratios of 0.034 to 0.076, suggesting that

reverse flow occurs in these craters. Thus, the position of windblown sediments in the northwest parts of the crater floors would indicate prevailing winds from the northwest to the southeast, consistent with late afternoon winds as predicted by the Mars Regional Atmospheric Modeling System (MRAMS) circulation model.

DEDICATION

Thank you to Mr. Richard Snyder for encouraging me to pursue something different and exciting. I would not have made it here without you. To my family (Julie, RD, Sarah, and Jared) who always knew that I could accomplish my goals, thank you for believing in me. Finally, I must thank my husband, Brandon, for his sacrifice and support. I greatly appreciate everything you have done to help me through this process.

ACKNOWLEDGMENTS

Sincere thanks to my advisor, Dr. Ronald Greeley, for providing me the opportunity to work with him on this project and my committee members, Dr. Philip Christensen and Dr. Kelin Whipple, for their time and advice. I would also like to express my gratitude to the School of Earth and Space Exploration at Arizona State University including all the professors who have contributed to my education. I thank Charles Bradbury, Andrew Britton, Nick DiCarlo, Rebecca Dorsey, Kayla Iacovino, Brandon Kienenberger, Leon Manfredi, Stefanie Musiol, and Amy Zink for their participation in field research and Charles Bradbury and Shuo Yuan for help with the statistical analysis of the wind data. Additional thanks to Mark Abel, Daniel Ball, Jonathon Benton, Michael Blessington, Charles Bradbury, Rebecca Dorsey, and Amy Zink for their help with wind tunnel simulations and Melissa Bunte, Stephanie Holaday, Mary Pendleton-Hoffer, Devin Waller, and Dave Williams for their contributions to this work. This research was funded by the NASA Planetary Geology and Geophysics Program and the JPL Mars Exploration Rover and Mars Express projects.

TABLE OF CONTENTS

Page

LIST OF TABLES viii

LIST OF FIGURES ix

CHAPTER

1 INTRODUCTION 1

Objective 1

Background 2

Flow Dynamics and Aeolain Processes 8

Previous Research 11

Research Approach 14

2 ANALOG FIELD STUDIES AT AMBOY CRATER 17

Approach 17

Results and Discussion 27

Conclusions 37

3 WIND TUNNEL SIMULATIONS 42

Approach 42

Results and Discussion 46

Conclusions 54

4 APPLICATION TO MARS 56

Approach 56

Results and Discussion 60

Conclusions and Future Research 68

Page

REFERENCES 72

APPENDIX

A ASOS USER'S GUIDE 81

B WIND TUNNEL MODEL PREPARATION 94

C TABLES 96

LIST OF TABLES

Table		Page
1.	Morphometric data for endogenic craters, Amboy lava field	19
2.	Weather data for Amboy lava field, California	28
3.	Weather data for Barstow, California	28
4.	Morphometric properties of wind tunnel models	44
5.	Summary of wind tunnel simulations	97
6.	Morphometric data for craters in Gusev Crater, Mars	98
7.	Characteristics of bedforms within craters in Gusev Crater, Mars	99
8.	Flow reattachment lengths within craters in Gusev Crater, Mars	100

LIST OF FIGURES

Figure		Page
1.	Gusev Crater, Mars	2
2.	Shallow craters in Gusev Crater, Mars	3
3.	Bedforms in Gusev Crater, Mars	5
4.	Wind tunnel model with zones of erosion and deposition	12
5.	MRAMS model for Gusev Crater, Mars	13
6.	Amboy lava field, Mojave Desert, California	16
7.	Real-time wind measurements, map of Crater 6, Amboy lava field	20
8.	Real-time wind measurements, map of Crater 7, Amboy lava field	21
9.	Map of Crater 11, Amboy lava field	22
10.	Map of Crater 20, Amboy lava field	22
11.	Crater map units, Amboy lava field	23
12.	Real-time wind measurement apparatus	24
13.	Sediment drift patterns in Craters, 6, 7, 11 and 20, Amboy lava field	25-26
14.	Sediment drift patterns in Craters 7 and 20, Amboy lava field	27
15.	Wind direction from May to November 2010, Amboy lava field	33
16.	Wind direction from May to November 2010, Barstow, California	33
17.	Locations of Barstow, Amboy, and Blythe, California weather stations	34
18.	Wind direction from May to November 2010, Blythe, California	35
19.	Wind speeds from May to November 2010, Amboy and Barstow	36

Figure Page

20. Crater 7 with wind streaks, Amboy lava field 38

21. Crater 6 with wind streaks, Amboy lava field 38

22. Craters 6, 7, and 11 with wind streaks, Amboy lava field 39

23. Arizona State University Planetary Geology Group wind tunnel facility 43

24. Wind tunnel crater model profiles 45

25. Wind tunnel grid run (CA_10_005) with Model #1 47

26. Wind tunnel deposition run (CA_10_001) with Model #1 48

27. Wind tunnel erosion run (CA_10_002) with Model #1 48

28. Wind tunnel deposition run (CA_10_025) with Model #2 49

29. Wind tunnel deposition run (CA_10_013) with Model #3 51

30. Wind tunnel deposition run (CA_10_018) with Model #5 51

31. Wind tunnel deposition run (CA_10_020) with Model #6 51

32. Wind tunnel deposition run (CA_10_014) with Model #4 (Amboy) 53

33. HiRISE stereo pair in Gusev Crater, Mars 57

34. Topographic profile locations for Crater 28, Gusev Crater, Mars 58

35. Crater morphometric parameters 59

36. d/D and r/D ratio vs the area of the crater floor with bedforms, Gusev Crater, Mars 62

37. Reverse flow over a backward-facing slope and over a crater 65

38. Crater wall slopes 66

Figure Page

39. Bedforms in Gusev Crater, Mars with possible wind directions 69

Chapter 1

INTRODUCTION

The Spirit and Opportunity rovers landed on the surface of Mars in Gusev Crater (Fig. 1) and Meridiani Planum, respectively, in January 2004 [*Squyres et al.*, 2004]. These areas have been studied intensely with rover instrumentation as well as from orbit [*Golombek et al.*, 2003, 2006b; *Christensen et al.*, 2004]. Shallow craters (<200 m in diameter) or "hollows" [*Golombek et al.*, 2006a] are prevalent near the rover landing sites and are thought to be eroded secondary impact craters [*Grant et al., 2006*; *McEwen et al.*, 2005]. These craters often contain asymmetric deposits of windblown (aeolian) sediments (Fig. 2). By studying the location and characteristics of these deposits with respect to the crater morphometry, it could be possible to infer the predominant local wind direction during deposition or redistribution.

1.1 Objective

The objective of this research is to understand how wind patterns and the resulting aeolian deposition in and around small craters (<200 m in diameter) vary as a function of crater morphometry (depth-to-diameter ratio, circularity) and determine if other parameters, such as rim height, affect the wind flow in and around craters. These results will be compared to craters on Mars to determine the prevailing depositional winds near the Spirit rover landing site in Gusev Crater. The three components of this research included: 1) field studies of terrestrial analog craters, 2) wind tunnel simulations with craters of known depths

and diameters for comparison to field studies, and 3) application of results to Mars.

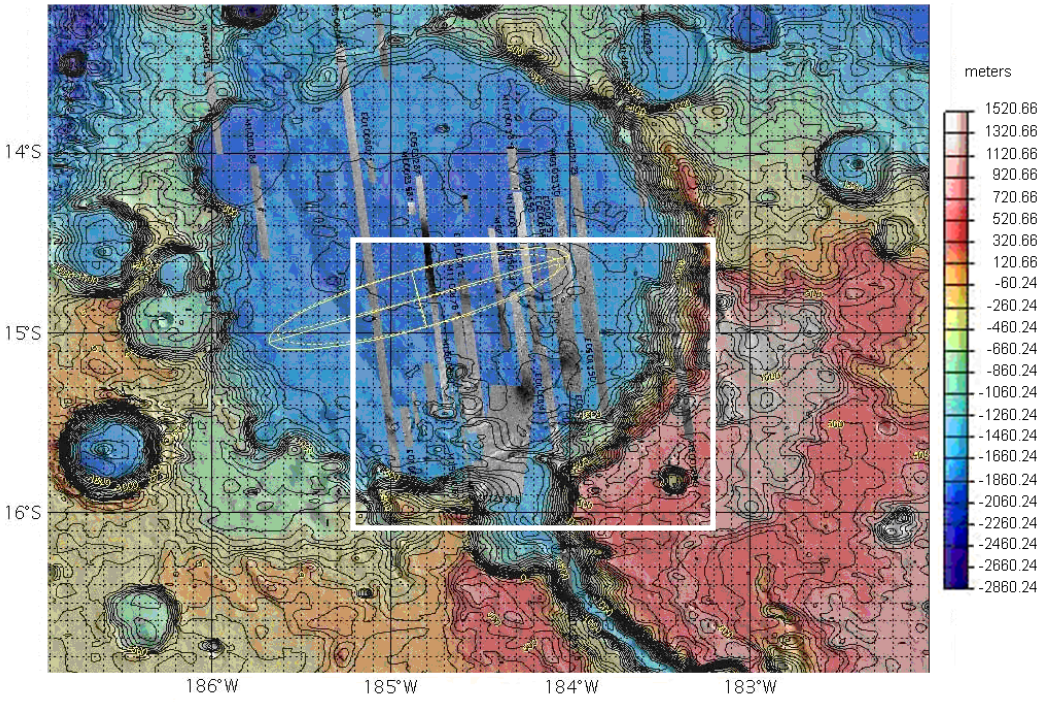

Figure 1: *Mars Orbiter Laser Altimeter (MOLA) map showing Gusev Crater, Mars and the approximate location of Mars Regional Atmospheric Modeling System data illustrated in Fig. 5. Image from the USGS.*

1.2 Background

Nearly all missions to Mars have indicated the presence of aeolian features, indicating that wind is a significant geologic process on the surface of the planet. These features were first observed in Mariner 9 images which revealed the presence of dunes and albedo features such as wind streaks caused by sediment-moving winds on Mars following a global dust storm in 1971 [*Sagan et al., 1972; Arvidson*, 1974]. The wind streaks, which point in the downwind

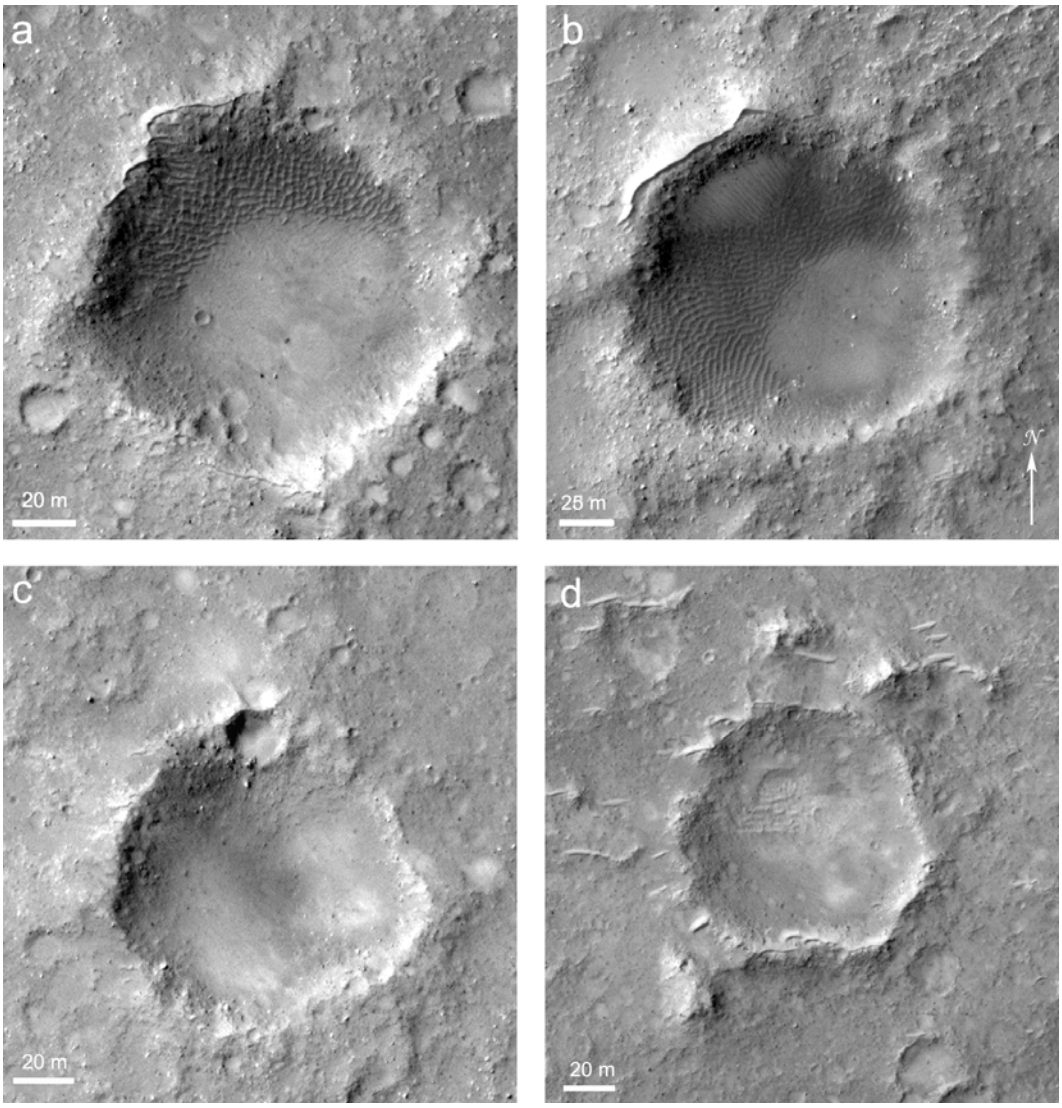

Figure 2: *Mars Reconnaissance Orbiter High Resolution Imaging Science Experiment (HiRISE) image (PSP_001513_1655) showing (a) Crater 1 and (b) Crater 3 with asymmetric windblown deposits and (c) Crater 32 and (d) Crater 38 with no asymmetric windblown deposits, all near the Spirit landing site in Gusev Crater, Mars.*

direction, occur in the lee of obstacles such as crater rims and represent deposition or erosion of material [*Greeley et al.*, 1974; *Thomas et al.*, 1981]. The dunes [*Cutts and Smith*, 1973] indicated that saltation is an important surface process. Slip-faces (steeper slopes) identified from the asymmetry of dunes can be used to

distinguish the windward (upwind) and leeward (downwind) sides of bedforms [*Bagnold*, 1941]. However, the images returned from the Mariner 9 mission did not provide the resolution necessary to infer the wind patterns associated with the dunes. Yardangs (elongated ridges which run parallel to the wind direction) were also discovered [*McCauley*, 1973], indicating that wind erosion occurs on Mars. The study of wind streaks and bedforms (aeolian features such as ripples or dunes that cannot be definitively classified) can lead to a determination of local wind regimes on Mars at the time of their formation [*Arvidson*, 1974]. However, the bedforms on the plains of Gusev Crater (Fig. 3) are small (<50 meters) and cannot be used to infer wind direction because most have ambiguous profiles [*Greeley et al.*, 2006a, 2008].

The Viking mission consisted of two orbiters and two landers which arrived at Mars in 1976. Areas on the surface of the planet which appeared as dark bands in Mariner 9 images were studied in detail with Viking images, including a large dune field in the polar region extending over an area roughly $5x10^5$ km^2 [*Tsoar et al.*, 1979]. The Viking spacecraft also observed relative stability for wind streaks with the exception of an area in the southern hemisphere which experienced seasonal variations in wind streaks [*Thomas and Veverka*, 1979]. In addition to large-scale features, small-scale aeolian features identified in Viking lander images included pitted rocks [*McCauley et al.*, 1979], wind tails, and drifts [*Mutch et al.*, 1976]. Estimated erosion rates from the relationship between pedestal craters and the surrounding terrain were shown to be much too

high based on the evidence provided by the Viking landers and *Arvidson* [1979] concluded that the yardangs likely formed in friable deposits such as volcanic ash.

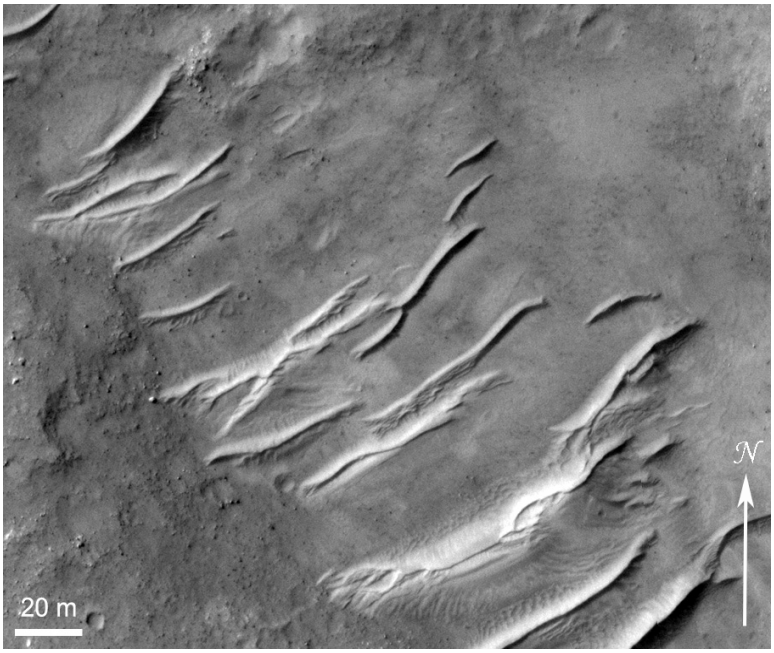

Figure 3: *Mars Reconnaissance Orbiter High Resolution Imaging Science Experiment (HiRISE) image (PSP_001513_1655) showing typical bedforms in Gusev Crater and the difficulty of identifying the slip faces.*

The Viking landers each carried meteorological instruments which allowed the collection of wind speed, wind direction, temperature, and atmospheric pressure data at the landing sites. These measurements, along with wind tunnel experiments under martian conditions, revealed that wind speeds at the landing sites were generally too low (<20 m/s) to induce grain saltation [*Greeley et al.*, 1980] but gusts up to 28 m/s were recorded [*Ryan et al.*, 1978] which might have induced saltation. However, the environment was conducive to the formation of dust devils which were positively identified at the Viking landing sites in subsequent analyses [*Ryan and Lucich*, 1983].

The Mars Global Surveyor (MGS) Mars Orbiter Camera (MOC) went into orbit around Mars in 1997 [*Malin et al.*, 1998]. High resolution images returned from the spacecraft indicated changes with time in the amount of aeolian activity based on the presence of active and inactive dunes. *Edgett and Malin* [2000] presented evidence for a more active aeolian regime in the past based on the presence of active and inactive dunes. In addition, the study of wind-related crater modification as seen in MOC images allowed an interpretation of seasonal wind regimes near the Pathfinder landing site [*Kuzmin et al.*, 2001]. The Pathfinder lander and its Sojourner rover also arrived on Mars in 1997 [*Golombek et al.*, 1997]. Although the Viking landers imaged numerous small-scale aeolian features, data from Mars Pathfinder provided evidence for features which were not present at either Viking site, including small barchan dunes and ventifacts [*Greeley et al.*, 1999]. The orientations of these features and wind tails in the area were combined to analyze the local wind regime near the Pathfinder landing site [*Greeley et al.*, 1999, 2000]. Following its arrival, MGS obtained images with multiple dark streaks on the surface of Mars which were attributed to dust devils [*Greeley et al.*, 2003] as previously suggested by *Grant and Schultz* [1987] from linear features in Viking images. However, this was not confirmed with ground images until the Mars Exploration Rovers (MER) arrived in 2004.

The MER, Spirit and Opportunity [*Squyres et al.*, 2004], have provided data on aeolian features including the dark streaks described above. In 2005, Spirit collected the first ground observation of an active dust devil with a dark

streak in its wake [*Greeley et al.*, 2006b]. Multiple wind-related features were observed, including ventifacts, ripples, drifts, and perched rocks, indicating small-scale aeolian features are common on the surface of Mars. The analysis of these features near the Spirit landing site have led to the interpretation of the local wind regime [*Greeley et al.*, 2006a] with competing winds from the northwest and southeast, related to the diurnal patterns due to local topography.

Over the past decade, several instruments orbited Mars with sophisticated remote sensing instruments, including the Thermal Emission Imaging System (THEMIS) in 2001 [*Christensen et al.*, 2004], Visible and Infrared Mineralogical Mapping Spectrometer (OMEGA) in 2003, High Resolution Stereo Camera (HRSC) in 2004 [*Bellucci et al.*, 2004], the Compact Reconnaissance Imaging Spectrometer for Mars (CRISM) in 2006 [*Murchie et al.*, 2007], and High Resolution Imaging Science Experiment (HiRISE) in 2006 [*McEwen et al.*, 2007]. These missions provide the highest resolution for features on the surface allowing identification of small aeolian bedforms [*Bridges et al.*, 2007] and compositional information for surface materials [*Christensen and Ruff*, 2004]. With these data, it is possible to infer the wind patterns associated with dunes located within craters [*Fenton et al.*, 2003; *Fenton*, 2006]. However, much of the research involving dunes within craters has been conducted on craters >100 km in diameter with considerable raised rims which are much larger than the craters that occupy most of the Gusev Crater floor.

In summary, aeolian activity is the dominant surface-modifying processes currently active on Mars. Multiple orbiting spacecraft have provided images which led to the identification of depositional and erosional features. In addition, these data have been compared to small features seen in lander (Viking 1 and 2) and rover (Sojourner, Spirit and Opportunity) images. An analysis of aeolian features from orbital and ground truth data can lead to a determination of regional wind patterns. These patterns can then be compared to the Mars General Circulation Model (MGCM) [*Pollack et al.*, 1990; *Greeley et al.*, 1993; *Haberle et al.*, 1993] and Mars Regional Atmospheric Modeling System (MRAMS) [*Rafkin et al.*, 2001] to allow for a geologic comparison to atmospheric modeling.

1.3 Flow Dynamics and Aeolian Processes

There are three types of grain movement by the wind: creep, saltation, and suspension [*Bagnold*, 1941]. Saltation, the bouncing of grains along a surface, is often self-perpetuating once started. Sand-sized particles ~100 μm in diameter are the easiest to move by saltation [*Greeley and Iversen*, 1987] on Earth, Mars and Venus. Particles with smaller grain sizes are harder to move due to moisture, van der Waal's forces, electrostatic charges and other inter-particle forces [*Iversen and White*, 1982], while the mass of larger particles inhibits movement.

Saltation occurs when particles are acted on solely by the force of the wind or are aided by impacting particles from an upwind source. The type of flow (laminar or turbulent) plays a major role in the movement of particles. Laminar flow is smooth, running parallel to a surface at a constant speed and is

characterized by the exchange of momentum between individual gas molecules. With increased velocity, groups of gas molecules exchange momentum creating eddies and turbulent flow, which accounts for near-surface wind flow in nature [*Bagnold*, 1941]. Increased turbulent flow often occurs in the lee of obstacles, causing an increase in the shear stress, τ, at the surface.

The Reynolds number, Re, characterizes the type of fluid flow (laminar or turbulent) and is based on the ratio of inertial forces to forces caused by kinematic viscosity as developed by Reynolds [1883] in studies of water flow through a pipe. Re is defined as:

$$Re = \rho U_{\infty} c/\mu \qquad \text{(Eq. 1)}$$

where ρ is equal to the density of the flow, U_{∞} is the fluid velocity, c is a characteristic length, and μ is the absolute viscosity. A large Reynolds number (200 for air flow through a pipe) indicates the presence of turbulent flow [*Bagnold*, 1941]. A surface can be characterized as aerodynamically "smooth" or "rough" depending on the value of the surface friction Reynolds number, Re_*, defined as:

$$Re_* = U_{\infty} d/\nu \qquad \text{(Eq. 2)}$$

where d is the particle diameter and ν is the kinematic viscosity [*Bagnold*, 1941].

For values of $Re_* = <70$ (aerodynamically smooth), a laminar sublayer, ranging in thickness from <1 mm on Earth to <9 mm on Mars [*White*, 1981], forms at the ground surface. Above this layer, the velocity can be determined by the following equation:

$$U_{\infty} = U_{*t}[(1/k)\ln(9U_{*t}/\nu)] \quad \text{(Eq. 3)}$$

where k is the Von Karman's constant, which has been shown empirically to be ~0.4, and U_{*t} is the threshold shear velocity (the velocity needed to move particles) represented by:

$$U_{*t} = (\tau_t/\rho)^{1/2} \quad \text{(Eq. 4)}$$

where τ_t is the threshold shear stress [*Bagnold*, 1941]. The shear velocity is directly related to the fluid velocity and can be calculated if a range of velocity measurements are collected at varying heights.

In contrast, for an aerodynamically rough surface, $Re_* \geq 70$, the laminar sublayer does not exist because the size of the surface grains are larger than the thickness of the sublayer. The velocity can be calculated as:

$$U_{\infty} = (U_{*t}/k)\ln(z/z_o) \quad \text{(Eq. 5)}$$

where z is the height above the surface and z_o is the roughness height [*Bagnold*, 1941]. When the surface changes from smooth to rough, a boundary layer forms. A boundary layer represents an area where the velocity is trying to regain equilibrium following an abrupt change in surface roughness. Although the change in velocity occurs instantaneously at the surface, it will take time to travel upward and thus, the thickness of the boundary layer increases with distance from the roughness boundary. The height of the boundary layer can be determined from a semi-log plot of the fluid velocity U_{∞}.

1.4 Previous Research

Raised-rim craters with deep floors have been shown to exhibit reverse flow in wind tunnel experiments for comparison with Mars [*Greeley et al.*, 1974]. As wind moves over the crater, a point of detachment forms allowing sand particles to move: 1) up and over the crater 2) around the sides of the crater forming a horseshoe vortex and/or 3) downward, forming a point of re-attachment and resulting in reverse flow across the crater floor. Reverse flow causes the erosion of particles from the downwind side of the crater floor producing a deposit on the upwind side in an area of stagnant wind (Fig. 4). The shallow craters within Gusev Crater have low rims and might not exhibit flow separation and reattachment, presenting a second possibility for a wind pattern: in the opposite direction, resulting in deposition of sediment against the downwind crater wall.

The overall topography of Gusev Crater and the presence of the Columbia Hills produce a complex wind regime within Gusev Crater [*Greeley et al.*, 2006a; *Sullivan et al.*, 2008]. Estimated wind patterns (Fig. 5) include winds from the northwest to southeast during the nighttime and from southeast to northwest during the daytime [*Rafkin et al.*, 2001]. Profiles from bedforms present on the plains of Gusev cannot be used reliably to infer wind direction due to their ambiguous shapes. Therefore, a thorough evaluation of sites of aeolian deposition as a function of crater morphometry is needed in order to characterize the prevailing depositional wind direction.

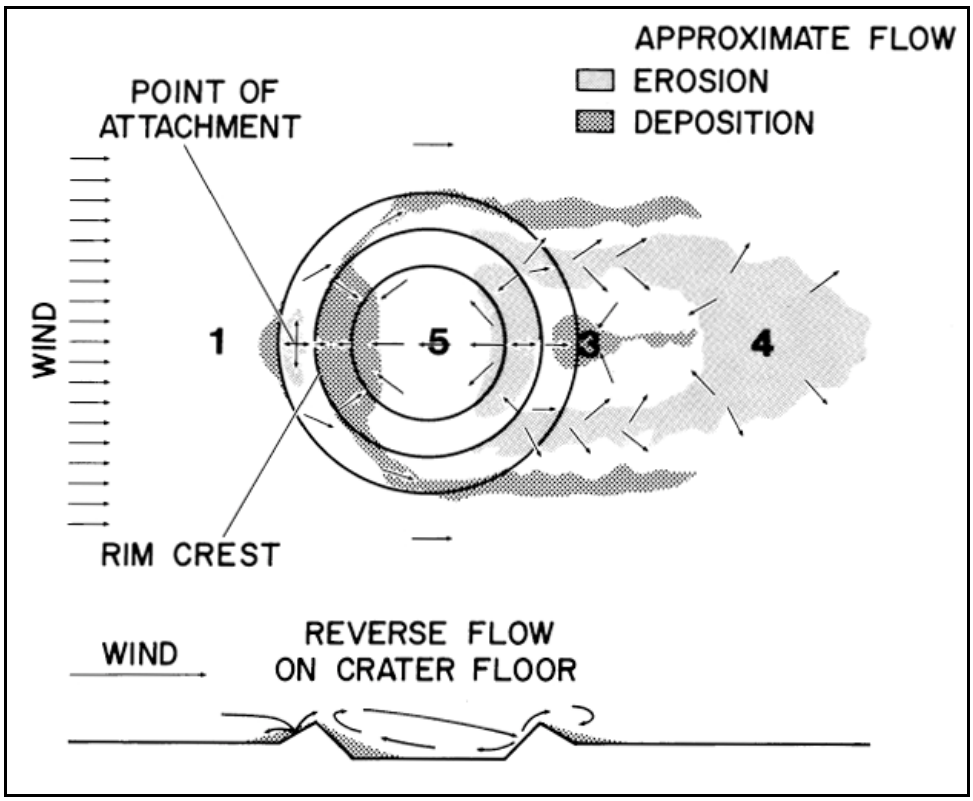

Figure 4: *Raised rim crater with arrows representing the direction of sand movement in and around the crater. Zone 1 represents the estimated location of the point of attachment, Zone 3 represents an area of deposition, Zone 4 represents an area of high erosion due to the presence of a horseshoe vortex which wraps around the crater on both sides and converges in Zone 4, and Zone 5 represents an area of erosion (leeward) and deposition (windward); from Greeley et al. [1974].*

A study of crater morphometry includes several parameters, such as the depth to diameter (d/D) ratio, rim height, and circularity. The d/D ratio has been used to study craters for more than 100 years, originally introduced for lunar craters by G. K. Gilbert in 1893 [*Melosh*, 1989]. Based on his findings, he was one of the first supporters of an impact origin for craters. Additional work from *Pike* [1980] included the use of photoclinometry (shadow measurement) to determine depths for several craters on Mars.

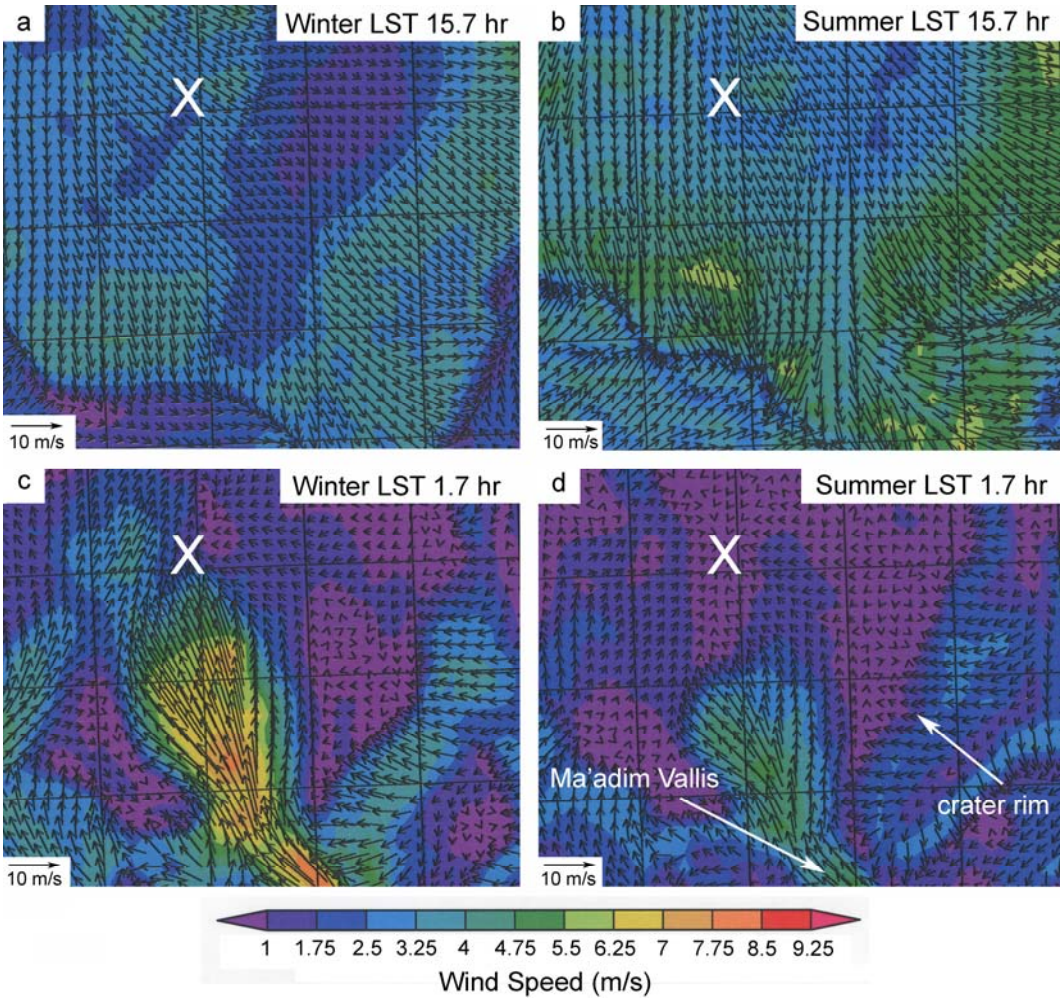

Figure 5: *Estimated wind patterns in southeastern Gusev Crater from the MRAMS for late afternoon (a) winter and (b) summer and nighttime (c) winter and (d) summer. Arrows point in the direction the wind is blowing toward at a height of 2 m and the Spirit landing site is designated as X. Images from Rafkin et al. [2001].*

The Mars Orbiter Laser Altimeter (MOLA) began orbiting Mars on MGS in 1997 and provided elevation data allowing crater d/D ratios to be studied more accurately. However, the spacing of MOLA data only provided a means to study craters with diameters larger than ~5-6 km [*Boyce et al.*, 2004]. Therefore, much of the d/D research to date has been conducted for craters of this size [*Boyce et al.*, 2005, 2006; *Garvin et al.*, 2000; *Parsons and Nimmo*, 2009]. Recent

advancements in the study of crater morphology were enabled by the High Resolution Imaging Science Experiment (HiRISE) camera, which has returned images with resolutions of 25-32 cm per pixel [*McEwen et al.*, 2007]. Utilizing stereogrammetry of HiRISE images [*Kim and Muller*, 2009] and the previously collected MOLA data allows a more precise map of the topography, aiding in the study of d/D ratios for smaller craters.

Crater circularity has been used to study differences in crater formation processes (volcanic or impact) and stages of degradation or deformation (crustal stresses) for lunar craters [*Ronca and Salisbury*, 1966; *Adler and Salisbury*, 1969] and Mars craters [*Oberbeck et al.*, 1972]. As a crater is degraded over time by erosion of the rim and infilling of sediment within the crater floor, the depth, diameter and circularity change. As these parameters are adjusted, the location and characteristics of aeolian deposition within the crater will also change. Therefore, in order to characterize the location of aeolian deposition as a function of crater morphometry, each parameter was measured/calculated for craters on Mars and in the field studies at Amboy lava field.

1.5 Research Approach

The first component of this research included field studies with full scale craters under natural conditions. A field area in the Mojave Desert of California provided an analog for the surface of Mars. The Amboy lava field (Fig. 6) consists of ~70 km^2 of vesicular pahoehoe basalt with an estimated age of 6,000 years [*Parker*, 1963]. Several endogenic craters (Fig. 6b) are located on the flow and provide good analogs for secondary impact craters on Mars because they have

similar morphometric (depth, diameter, circularity) properties. Field research consisted of real-time wind measurements, assessments of active sediment deposition in four small (<100 m) craters, and a preliminary determination of long-term wind patterns at the site.

The second component of this research included wind tunnel simulations which were conducted under ideal conditions for comparison to the results of field research with full-scale terrestrial analog craters under natural conditions. Six crater models, including a scaled model of an endogenic crater from Amboy lava field, were produced for experimentation in the wind tunnel. The wind flow patterns and areas of sediment deposition and/or erosion in and around the craters were compared to the crater morphometries (depth, diameter).

Morphometric data for small craters near the Spirit rover landing site were collected using a digital elevation model [*Kirk et al.*, 2008]. These data and the locations and characteristics of windblown deposits within the craters as seen from HiRISE images were compared to the results of field studies and wind tunnel simulations. Initial applications were used to infer the local predominant wind direction at the time of deposition near the Spirit rover landing site.

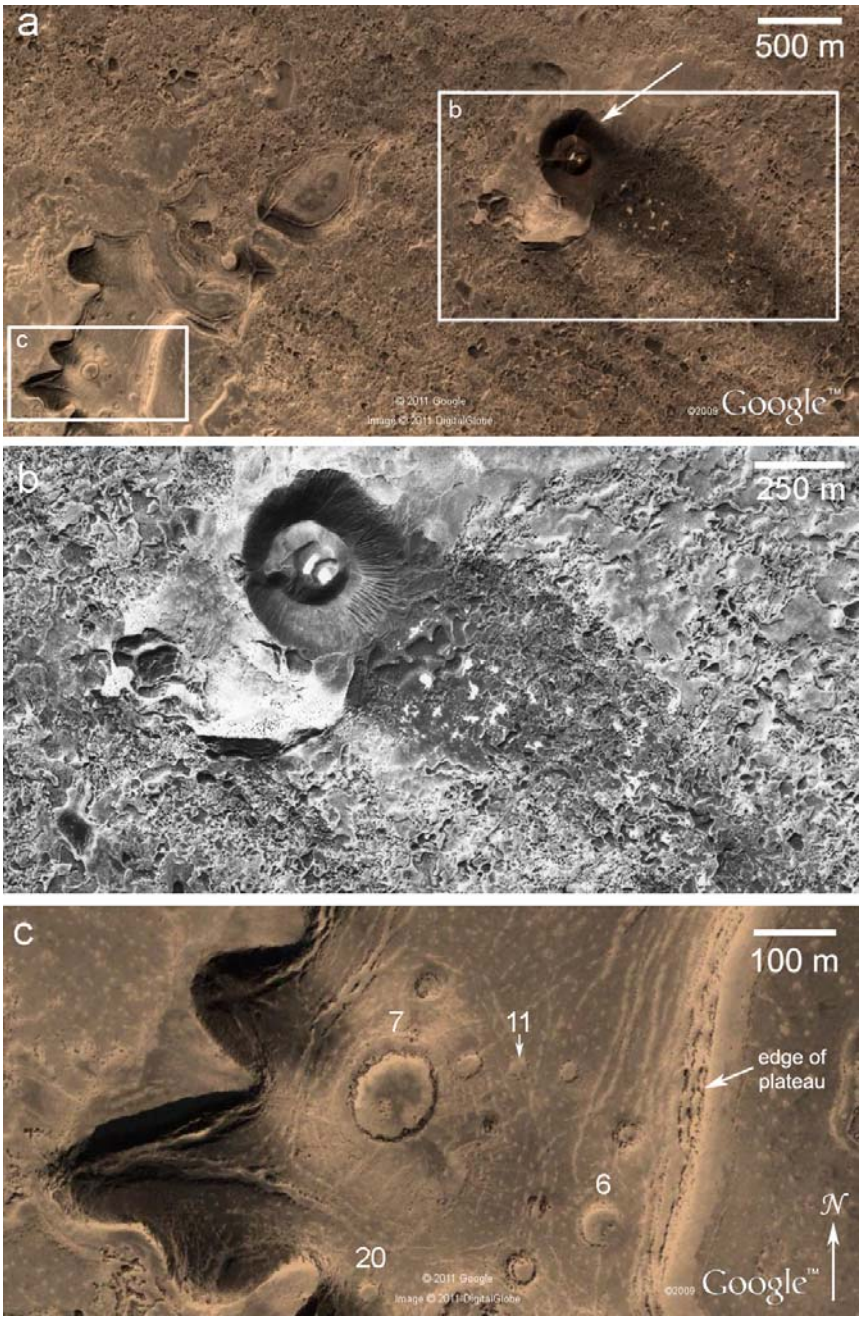

Figure 6: *(a) Part of Amboy lava field, Mojave Desert, California including cinder cone (arrow) and wind streak. Source: 34°32'07'' N and 115°48'05'' W. Google Earth. February 17, 2003. November 23, 2010. (b) Aerial photograph of the cinder cone and wind streak from 1953. Source: Dr. Ronald Greeley. (c) Enlargement with endogenic craters 6, 7, 11 and 20 on a lava pressure plateau. Source: 34°31'57'' N and 115°49'24'' W. Google Earth. February 17, 2003. November 23, 2010. Twenty craters were initially identified for study but this research focused on the four craters noted.*

Chapter 2

ANALOG FIELD STUDIES AT AMBOY CRATER

The Amboy lava field in the Mojave Desert, California (Fig. 6) has been used as an analog for many applications to Mars, including the interaction of aeolian and volcanic processes [*Greeley and Iversen*, 1986; *Iverson and Greeley*, 1978]. The lava field consists of ~70 km^2 of vesicular pahoehoe basalt with an estimated age of 6,000 years [*Parker*, 1963]. A dark wind streak in the lee of a large cinder cone extends ~4 km to the southeast (Fig. 6a), indicating prevailing winds from the northwest. Alluvial deposits upwind of the lava field provide a source for sand particles which are transported across the lava and provide a contrast to the basalt flow. Lag deposits are common at Amboy and form due to the sorting of particles by the wind. Sand particles have lower threshold velocities and are carried away [*Bagnold*, 1941] while basalt fragments are left in place. Desert pavement is also common at the Amboy field site and represents a combination of the process for lag deposits as well as the presence of silt and clays which expand, forcing the larger (gravel-sized) basalt particles to the surface [*Greeley and Iversen*, 1978]. These basalt particles provide a protective surface and if disturbed, will reveal underlying silt and clay particles.

2.1 Approach

Small endogenic craters (likely formed by collapse as lava moved forward along the flow front) ~20 to 110 m in diameter (Fig. 6c) provide good analogs for secondary impact craters on Mars because they have similar morphometric

properties (depths and diameters) and are partly mantled by aeolian material. Morphometric data for 20 craters at the Amboy site were collected in the field and from aerial photographs. Those shown in Figure 6c were the focus of the study because they have similar morphometries to the craters in Gusev (Table 1). The rim-to-rim diameters of the craters were obtained following the method of *De Hon* [1981] by tracing the outline of the rim from a Google Earth image and overlaying perfect circles of different sizes to obtain a best-fit diameter. The rim-to-floor depths were collected in the field using a laser level placed on the crater rim and a measuring rod located in the deepest part of the crater floor. Craters 6, 7, 11 and 20 were mapped (Fig. 7-10) to illustrate prominent features such as active sand deposits, lag deposits, transitional zones (from sandy to lag surfaces), and desert pavement (Fig. 11). Bushes and large rock piles (~0.5 meters high), which could interfere with wind patterns in the crater, were also mapped.

Topographic profiles for Craters 6 and 7 (Fig. 7-8) were completed with a laser level, measuring rod and measuring tape. The profiles were extended past the crater rims to determine the slope of the surrounding terrain. An azimuth of 155° was used for the profile of Crater 7, which represented the wind direction during the site visit in February 2009. An azimuth of 130° was used for Crater 6, which corresponded with the inferred predominant wind direction in the field area, as suggested by the wind streak in the lee of the cinder cone (Fig. 6a). Bushes and large rock piles were avoided to ensure that the topographic data were indicative of the crater floor.

Crater	Depth (m)	Circle Diameter (m)	Measured Diameter (m)	d/D Ratio (Circle)	d/D Ratio (Measured)	Circularity
1	1.67	37.04	31.85	0.045	0.052	1.23
2*	2.11	37.27	36.43	0.057	0.058	1.10
3	2.43	50.00	44.05	0.049	0.055	1.22
4	1.39	35.00	34.07	0.040	0.041	1.21
5	1.56	39.05	41.58	0.040	0.038	1.06
6*	3.00	52.63	57.33	0.057	0.052	1.02
7*	5.40	102.17	111.32	0.053	0.049	1.05
10	2.22	37.50	30.67	0.059	0.072	1.12
11*	0.53	27.78	25.00	0.019	0.021	1.03
12	0.63	27.86	23.38	0.023	0.027	1.09
13	2.50	41.86	37.88	0.060	0.066	1.13
15	1.00	40.91	34.43	0.024	0.029	1.17
16	0.62	32.05	29.71	0.019	0.021	1.15
17	1.37	32.73	27.65	0.042	0.050	1.19
18	0.57	24.00	19.00	0.024	0.030	1.04
19	1.22	44.68	38.66	0.027	0.032	1.20
20*	2.08	25.32	25.41	0.082	0.082	1.04
21	1.74	24.35	21.17	0.071	0.082	1.10
22	0.84	34.64	26.68	0.024	0.031	1.10
23	0.67	33.96	31.73	0.020	0.021	1.09

Table 1: *Morphometric properties of endogenic craters, Amboy lava field, Mojave Desert, California. d, D, r, and m represent the following parameters in order: depth, diameter, rim height, meters. * Indicates sand piles were placed in the crater for long-term wind observations.*

Real-time wind patterns were determined for Crater 6 in October and December 2009 and for Crater 7 in April 2010 using metal rods and suspended weighted styrofoam balls (Fig. 12) placed in the ground at ~35 locations in and around each crater. As the wind blew, the styrofoam balls moved in the downwind direction, the azimuth of which was determined with a Brunton compass (surveyed downwind from the apparatus so the wind was not disrupted). Measurements were taken within 30 minutes to obtain a "snapshot" of the overall wind regime for the craters.

Sediment drift patterns indicative of sediment-moving wind were derived from conical piles of dyed sand placed within Craters 6, 7, 11, and 20 and monitored over a period of ~1 year. Each pile consisted of 2.4 liters of purple-

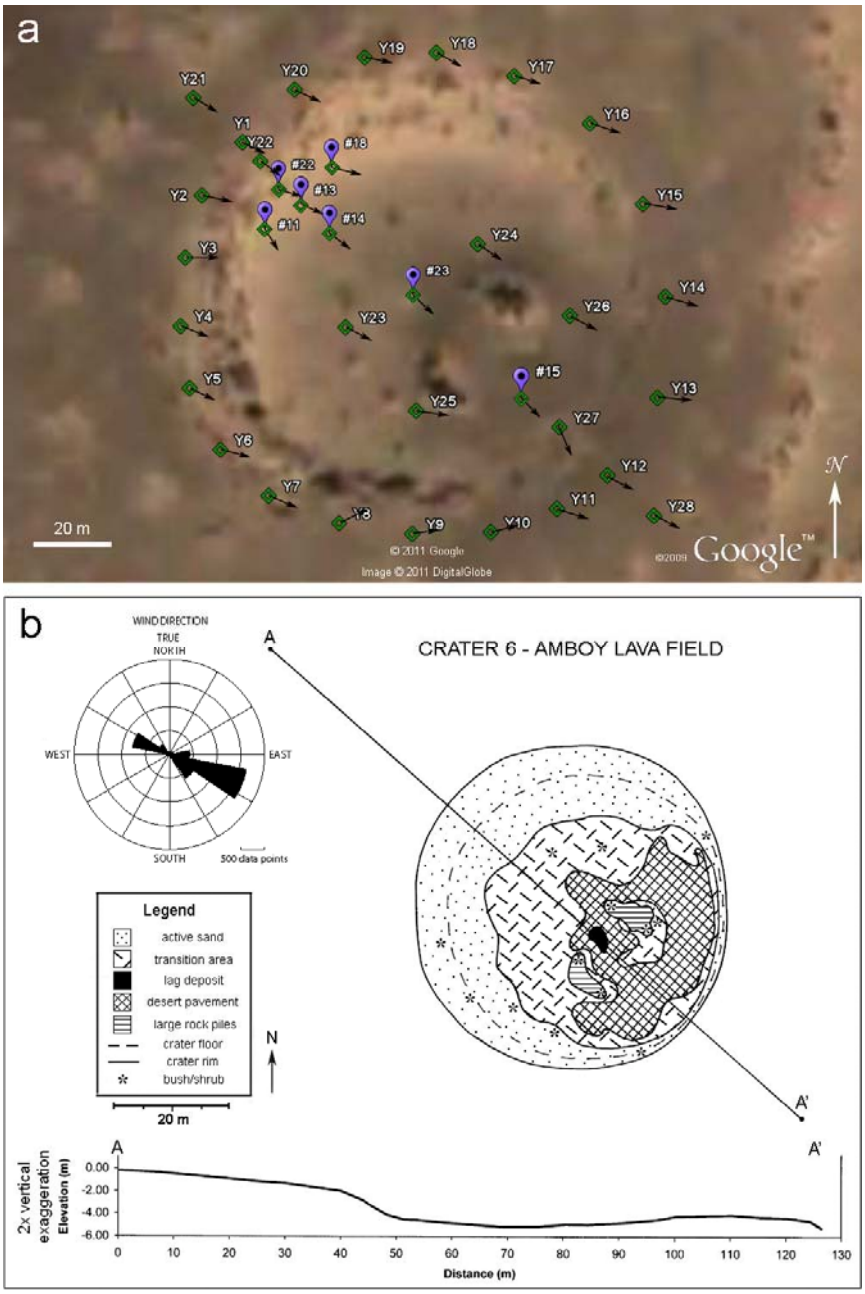

Figure 7: *Crater 6 with d/D of 0.052. (a) Real-time wind vectors taken within 30 minutes in December 2009. Real-time wind measurements within the crater floor were taken near the purple sand piles used for long-term wind observations (# locations) while measurements on the perimeter of the crater are denoted by Y locations. Source: 34°31'57'' N and 115°49'24'' W. Google Earth. February 17, 2003. November 23, 2010. (b) Map and topographic profile showing asymmetric distribution of aeolian deposits and other material on the crater floor. The rose diagram shows downwind directions for May through November 2010 from measurements in the field.*

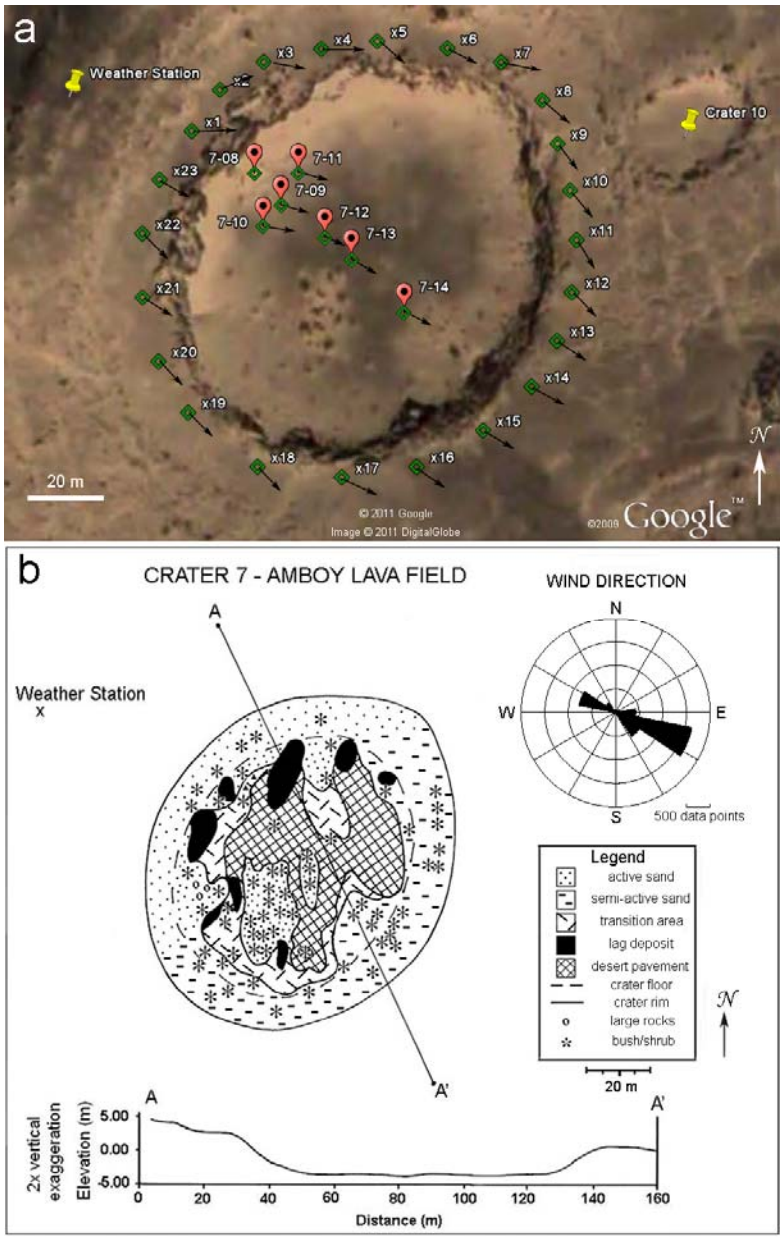

Figure 8: *Crater 7 with a d/D of 0.049. (a)* Real-time wind vectors taken within *30 minutes in April 2010. Real-time wind measurements within the crater floor were taken near the red sand piles used for long-term wind observations while measurements on the perimeter of the crater are denoted by X locations. There was an area of stagnant wind in the northwest portion of the crater floor near sand pile 7-08. Source: 34°31'57'' N and 115°49'24'' W. Google Earth. February 17, 2003. November 23, 2010. (b) Map and topographic profile showing the distribution of aeolian deposits and other material on the crater floor. The rose diagram shows downwind directions for May through November 2010 from measurements in the field.*

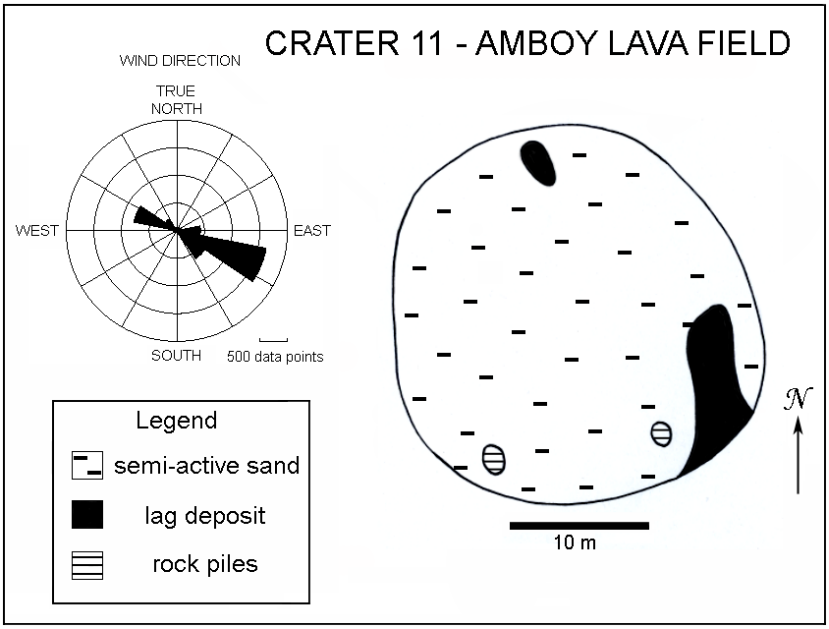

Figure 9: *Crater 11 (d/D = 0.021) map showing the distribution of aeolian deposits and other material on the crater floor. The rose diagram shows downwind directions for May through November 2010 from measurements in the field.*

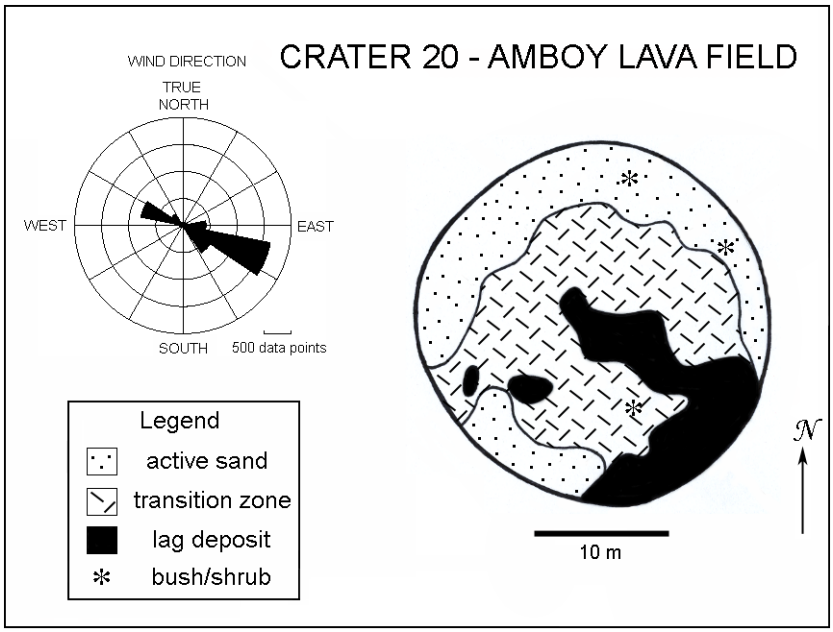

Figure 10: *Crater 20 (d/D = 0.082) map showing the distribution of aeolian deposits and other material on the crater floor. The rose diagram shows downwind directions for May through November 2010 from measurements in the field.*

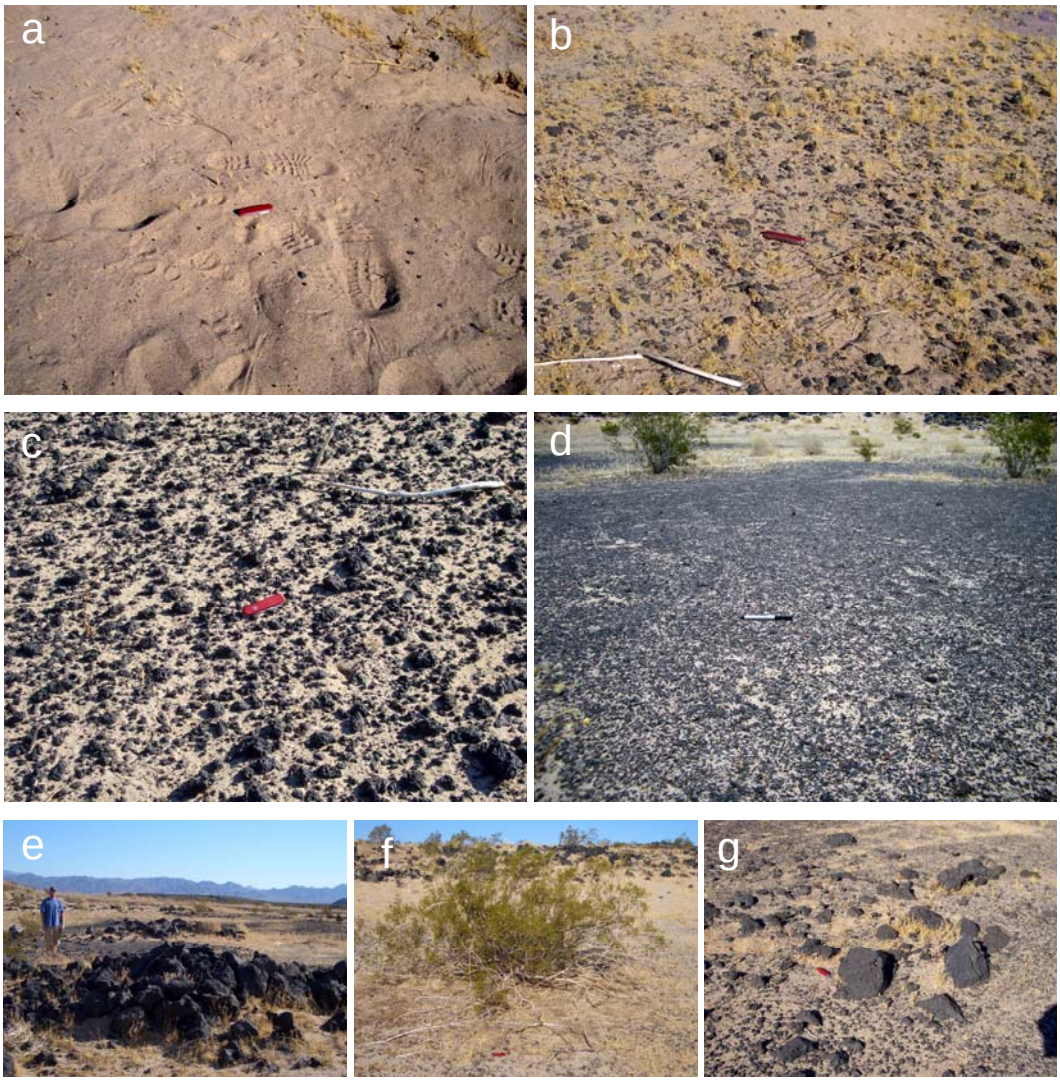

Figure 11: *Representative pictures of Craters 6 and 7 map units (a) sandy area (b) transition area (c) lag deposit (d) desert pavement (e) large rock piles (f) bush/shrub and (g) large rocks with Swiss Army knife and marker for scale.*

dyed sands ~300-600 μm in diameter and placed in seven locations within each crater. Five sand piles were placed in a line parallel to the predominant strike of the wind direction (NW-SE) and two piles were placed on either side of this line (Fig. 7-8). As winds blew over the crater, the dyed sand was eroded from the pile and redeposited downwind (Fig. 13-14). Craters 6 and 7 contained two sets of sand piles, a purple set placed during the winter, 2009 and a red set placed in the

Figure 12: *Real-time wind azimuths were determined from an array of sensors placed in and around the crater. Each sensor consisted of (a) a metal rod (b) line and (c) a weighted styrofoam ball; as the wind blew, the ball moved downwind (d) and the azimuth of the direction was measured. Also shown is the pile (e) of dyed sand (with flag) used to track the trend of redeposited sand.*

summer, 2010. Each sand pile was numbered with a flag which was placed in the center of the pile. During subsequent visits to the field, measurements were taken to document the changes in the piles over time. The lengths and azimuths of the redeposited sand were measured from its numbered flag.

Meteorological data were collected at Amboy in January and February 1976 [*Iversen and Greeley*, 1978] to monitor wind patterns. Primary data were collected from four 15 m-high towers which recorded wind direction at the top of each tower and wind speeds at 10 heights above the surface. These data enabled characterization of the lower boundary layer and the resulting surface shear stress and showed that the prevailing wind direction is from the west northwest, consistent with the wind streak in the lee of the cinder cone (Fig. 6a). Following this research, the towers were dismantled in 1976 and the collection of meteorological data at the Amboy field site ceased until this study in 2009-2010,

when a temporary Davis Vantage Vue weather station was placed in the field in May 2010 ~50 m northwest of Crater 7 (Fig. 8) to measure wind speed and direction over each one-hour interval were collected from 11 May to 27 November, 2010 (Table 2).

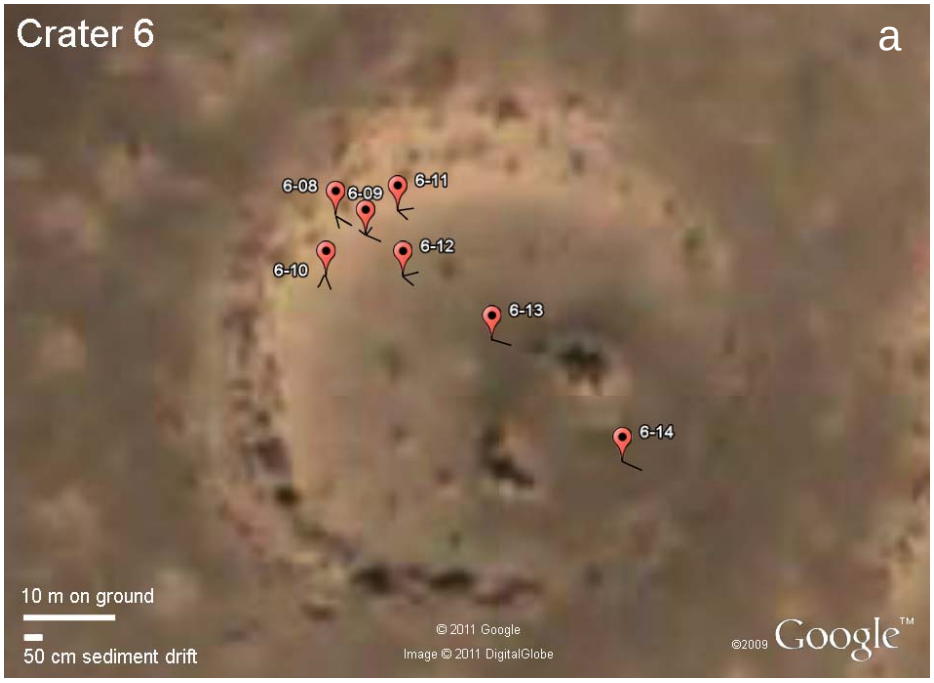

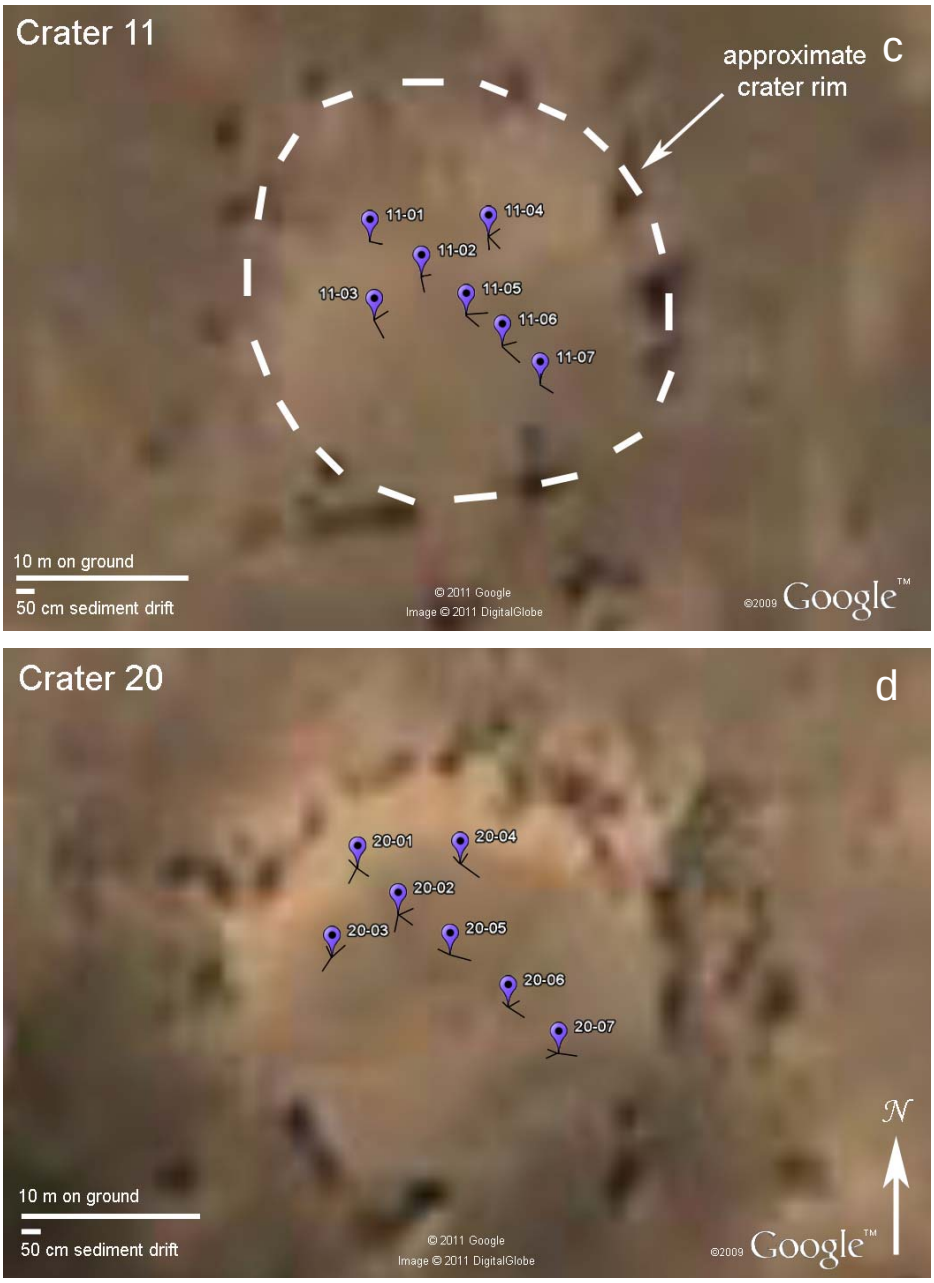

Figure 13: *Sediment drift results for (a) Crater 6 (b) Crater 7 (c) Crater 11 and (d) Crater 20. The labeled markers represent the locations of sand piles and the measurements represent the length and corresponding azimuth of the sediment drift pattern in cm from the center of the pile (numbered flag). The sand piles were placed in the craters on April 17, April 10, March 21, and April 10 of 2010, respectively. These measurements were taken ~1 month after the initial placement and additional measurements were collected during four subsequent visits. Source: 34°31'57'' N and 115°49'24'' W. Google Earth. February 17, 2003. November 23, 2010.*

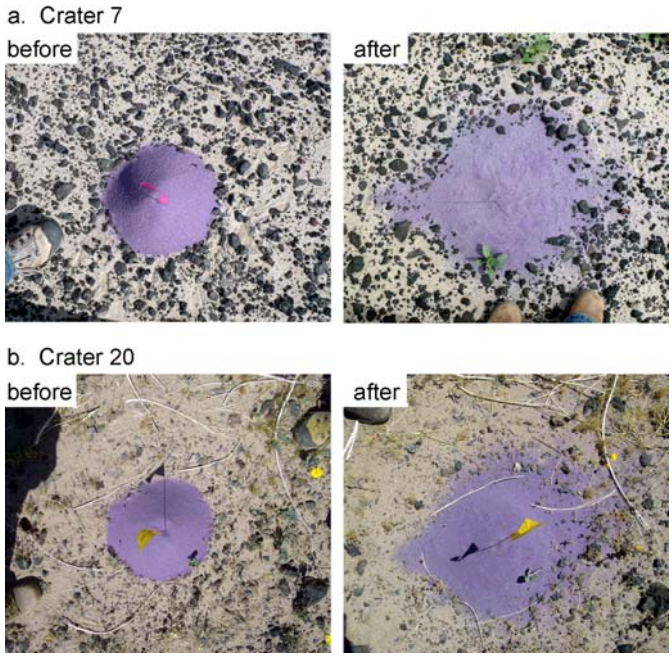

Figure 14: *Sediment drift observations for (a) sand pile 7-03 (near sand pile 7-10) in Crater 7 in January and March 2010 and (b) sand pile 20-05 in Crater 20 in April and May 2010 showing downwind and upwind movement (likely due to reverse flow). The right of each image is to the southeast (downwind).*

The nearest permanent weather station is located at the Barstow-Daggett airport, California, ~120 km to the northwest of Amboy. Historic weather data from this station are available from 1948 to the present and include wind directions and speeds collected at a height of 10 m (Table 3). The wind data collected at the Amboy field site were compared to the Barstow data to enable an assessment of prevailing winds for a longer period of time than the data from the temporary station at the field site.

2.2 Results and Discussion

Crater 6 is located on the eastern edge of the lava plateau (Fig. 6b) on terrain sloping ~4° to the southeast (facing away from the predominant wind direction). This crater is very circular in planform with no raised rim. Based on

Month	Ave. max. temp. (°F)	Ave. humidity (%)	Ave. barometric pressure (inches)	Ave. dew point temp. (°F)	Ave. wind speed (m/s)	Dominant wind azimuth	Max. speed (m/s)	Max. wind speed azimuth
May*	89	17	29.74	25	5.07	ESE	23.7	ESE
June	104	14	29.64	31	4.03	ESE	18.3	ESE
July	110	15	29.60	41	3.69	ESE	18.8	N
August	107	17	29.63	38	3.94	ESE	20.1	ESE
September	103	14	29.67	28	4.40	ESE	15.2	WNW
October	86	33	29.88	40	4.47	ESE	24.1	ESE
November*	75	27	30.01	25	5.48	ESE	21.0	ESE

Table 2*: Meteorological data from Amboy lava field in 2010 taken at a height of 0.9 meters above the ground surface over one hour intervals. Azimuths represent the direction the wind is blowing toward. * indicates data is not available for the full month.*

Month	Ave. max. temp. (°F)	Ave. humidity (%)	Ave. barometric pressure (inches)	Ave. dew point temp. (°F)	Ave. wind speed (m/s)	Dominant wind azimuth	Max. speed (m/s)	Max. wind speed azimuth
May*	83	26	29.84	29	6.97	E	20.6	E
June	99	23	29.77	35	6.75	E	34.5	E
July	107	17	29.75	37	5.61	E	19.5	N
August	103	19	29.77	36	5.35	E	19.0	NW
September	98	19	29.79	31	4.91	E	25.7	NE
October	80	41	29.96	40	4.57	E	16.5	NE
November*	68	39	30.05	28	4.97	E	16.5	E

Table 3*: Meteorological data from Barstow, California in 2010 taken at a height of 10 meters above the ground surface over one hour intervals. Azimuths represent the direction the wind is blowing toward. * indicates data is not available for the full month.*

the topographic profile (Fig. 7b), the crater wall slopes on the northwest and southeast sides of the crater are significantly different, with the steeper slope on the northwest side of the crater (facing away from the predominant wind direction). The depth-to-diameter ratio (d/D) for Crater 6 is 0.052. Real-time wind measurements (Fig. 7a) for this crater were completed in December 2009 during a time when the wind was moving in the predominant direction from northwest to southeast. These measurements show that the wind moves in the downwind direction in and around all parts of the crater except in the northwest part of the floor where wind was relatively stagnant. Sediment drift deposits from the piles of dyed sand show southeast-trending movement with some northwest-trending redeposition in the northwest portion of the crater floor (Fig. 13a) suggesting reverse flow. This trend is consistent with the location of windblown deposits on the northwest side of the crater (Fig. 7b), indicating long-term deposition. A large area of desert pavement within the crater floor indicates an area of equilibrium between erosion and deposition.

Crater 7 is located on the western edge of the lava plateau (Fig. 6b) on terrain sloping ~4° to the southeast (facing away from the predominant wind direction). This crater is slightly elongated in the southwest to northeast direction. Based on the topographic profile (Fig. 8b), Crater 7 has little to no raised rim above the surrounding terrain and a d/D of 0.049. The crater wall slopes on the northwest and southeast sides of the crater are similar at ~14° and 11°, respectively, with the steeper side facing away from the predominant wind

direction. Real-time wind measurements were made in April 2010 when the wind was moving in the predominant wind direction from the northwest. These measurements show that the wind generally moves across the crater (Fig. 8a) and has reverse flow and a stagnant zone in the northwest crater floor following wind gusts. Sediment drifts of dyed sand show predominantly southeast-trending patterns with northwest-trending deposits in the middle and northwest portions of the crater floor (Fig. 13b and 14a), suggesting reverse flow. Results of crater mapping (Fig. 8b) revealed Crater 7 has equally distributed aeolian material around the edges of the crater floor, with active sand deposits on the northwest side of the floor, indicated by its high albedo in the aerial photo. A large area of desert pavement within the crater floor indicates an area relatively swept free of loose sand.

Crater 11 is located in the middle of the lava plateau (Fig. 6b) on relatively level terrain. It is fairly circular with no raised rim and has a d/D of 0.021. The crater wall slopes on the northwest and southeast sides are nearly equal. Although no real-time wind measurements were made for this crater, sediment deposition of the dyed sand show southeast-trending winds with no northwest-trending patterns (Fig. 13c), indicating a lack of reverse flow in this crater. Mapping of the crater floor (Fig. 9) shows uniform sand deposits and lag surfaces with no desert pavement.

Crater 20 is located on the southern edge of the lava plateau (Fig. 6b) on terrain sloping to the southeast (facing away from the predominant wind

direction). This crater is very circular in planform, lacks a raised rim, and has a d/D of 0.082. The wall slopes on the northwest and southeast sides of the crater are ~15° and 7°, respectively, with the steeper side facing away from the predominant wind direction. Real-time wind measurements were not made for this crater but sediment distributions of dyed sand show southeast and northwest-trending patterns (Fig. 13d and 14b) with nearly three times as many northwest-trending patterns than the other craters during the same period (April 2010). Mapping of the crater floor (Fig. 10) shows asymmetrically distributed aeolian material on the northwest part of the crater floor, similar to Crater 6, and lag deposits on the southeast part of the crater floor.

Results of real-time wind measurements, sediment drift patterns, and crater mapping indicate that reverse flow likely occurs in Craters 6, 7 and 20. The greatest number of northwest-trending streaks was observed in the deepest crater (Crater 20), suggesting that the area of the crater floor affected by reverse flow might be directly related to the crater depth. The shallowest crater, Crater 11, lacks evidence for reverse flow and we suggest that a d/D of $\leq$0.05 precludes this wind pattern.

Based on the wind data collected at Amboy, the predominant sand-moving wind direction is from northwest to southeast (Fig. 15), consistent with previous results [*Iversen and Greeley*, 1978]. In addition to the predominant wind direction, a secondary wind direction (from southeast to northwest) is common at Amboy, especially in the summer, accounting for 17% of the winds in May and

44% in August. The weather records from Barstow, the nearest weather station (~75 miles northwest of Amboy), during the same months of observation for Amboy indicate a predominant wind direction from west to east (Fig. 16) with no significant secondary wind direction. The state climatologist for Arizona, Nancy Selover, stated the topography of the Amboy site (located within a valley between two mountain ranges trending northwest to southeast) could play a major role in the reversal of winds during the summer months (personal communication). In Arizona, the winds generally blow from south to north during the summer months. These winds could be redirected through the valley, producing the secondary wind direction (southeast to northwest) observed at Amboy during the summer months. However, Barstow, located in a flat topographic setting is not influenced by the winds from the south due to the stronger winds from the west. To test this hypothesis, wind data from Blythe, California (Fig. 17) were collected to determine the prevailing wind direction from May through November 2010 (Fig. 18). Based on these data, the winds in Blythe blow from south to north during the summer months, and show a steady increase in dominance from May through July, as seen in the Amboy data (winds from southeast to northwest). Therefore, it is possible that the secondary wind direction observed at Amboy is caused by the south to north winds during the summer months.

The average wind speeds measured at the field site range from 3 to 5 m/s with the highest wind speeds reaching nearly 24 m/s (Fig. 19). These speeds are lower than the average Barstow winds of 5 to 7 m/s, likely due to the different

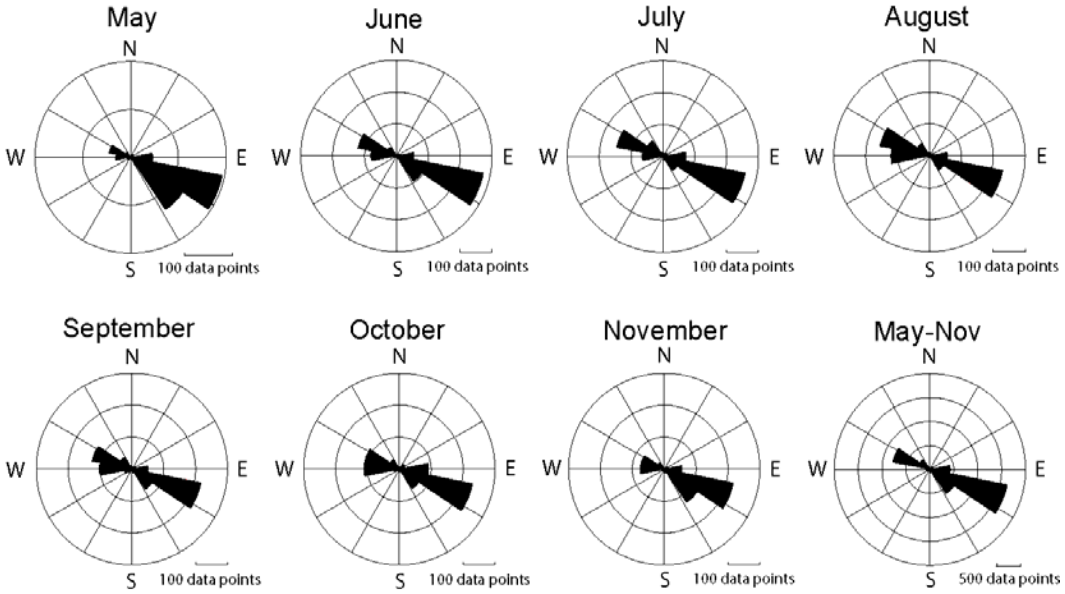

Figure 15: *Rose diagrams showing the downwind azimuths at Amboy lava field from May to November 2010. Measurements were taken at a height of 0.9 meters.*

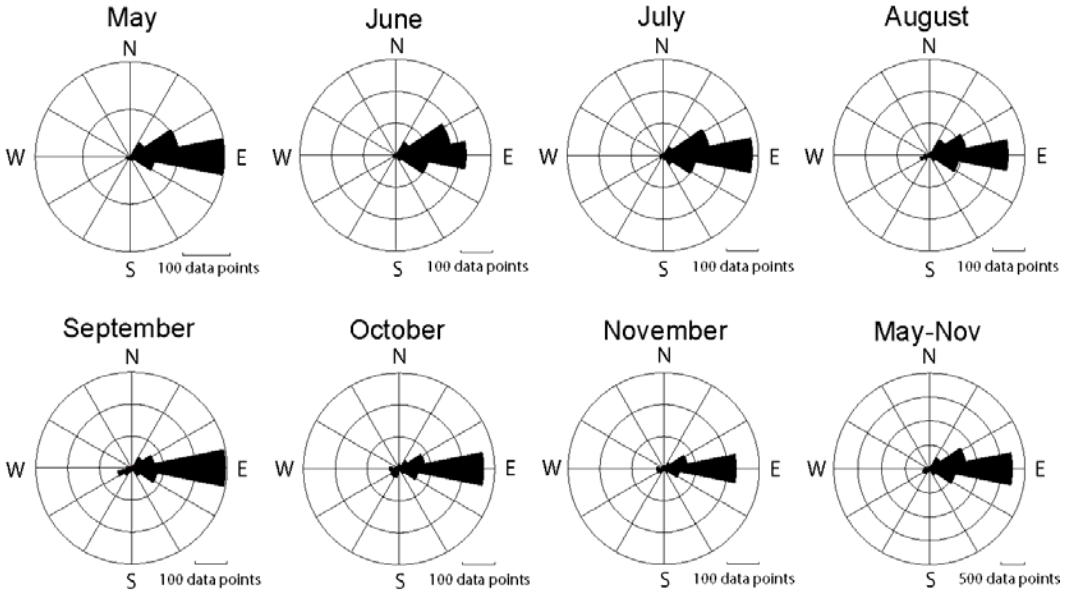

Figure 16: *Rose diagrams showing the downwind azimuths in Barstow, California from May to November 2010. Measurements were taken at a height of 10 meters.*

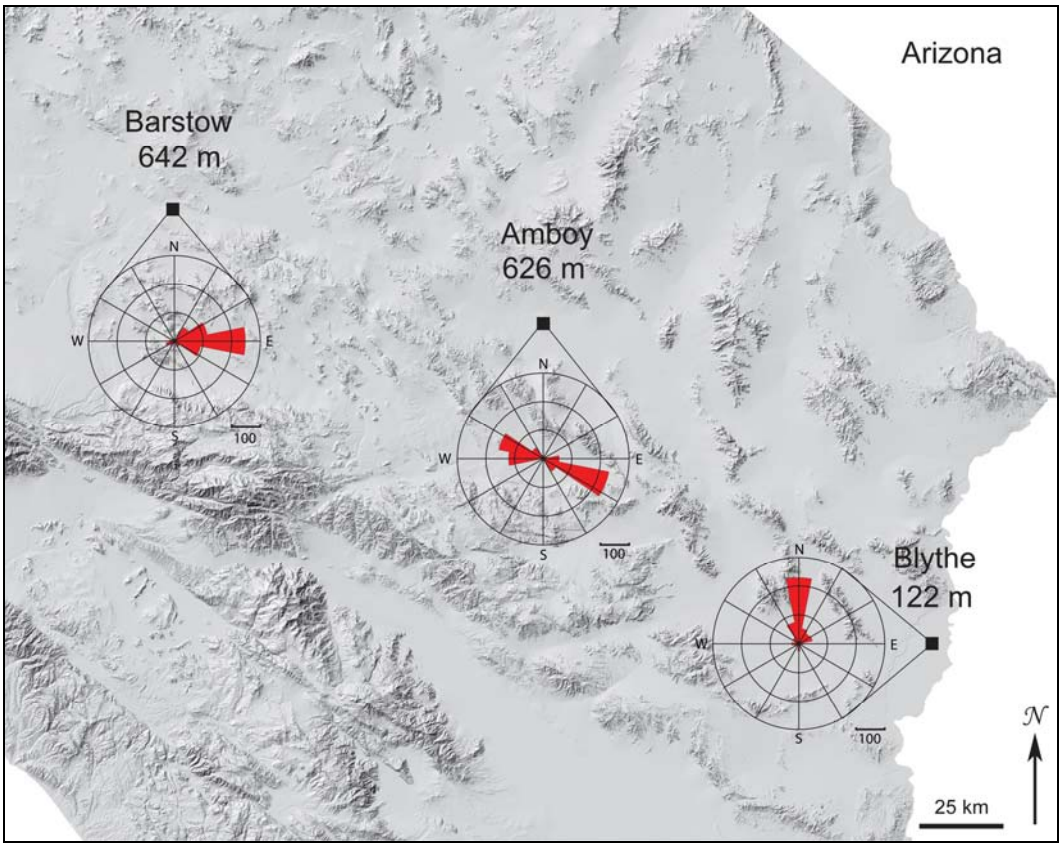

Figure 17: *Geographic and topographic settings of Barstow, Amboy, and Blythe, California with elevations and rose diagrams showing the downwind azimuths in each location during August 2010. Measurements were taken at heights of 10, 0.9, and 10 meters, respectively. Image from United States Geological Survey (USGS).*

heights of the weather stations (0.09 m at Amboy, 10 m at Barstow). During the summer months, the average wind speeds decrease slightly in both areas.

The wind records at the Amboy site are limited to less than one year, yet the accumulation of sediments in the craters reflects a longer period of time. The station in Barstow has weather records from 1948 to present and there is the possibility for extrapolating the wind records (Table 3) to the Amboy site. To determine the validity of the extrapolation, a statistical analysis compared the Amboy and Barstow wind speeds for the same period of time (May 11 to

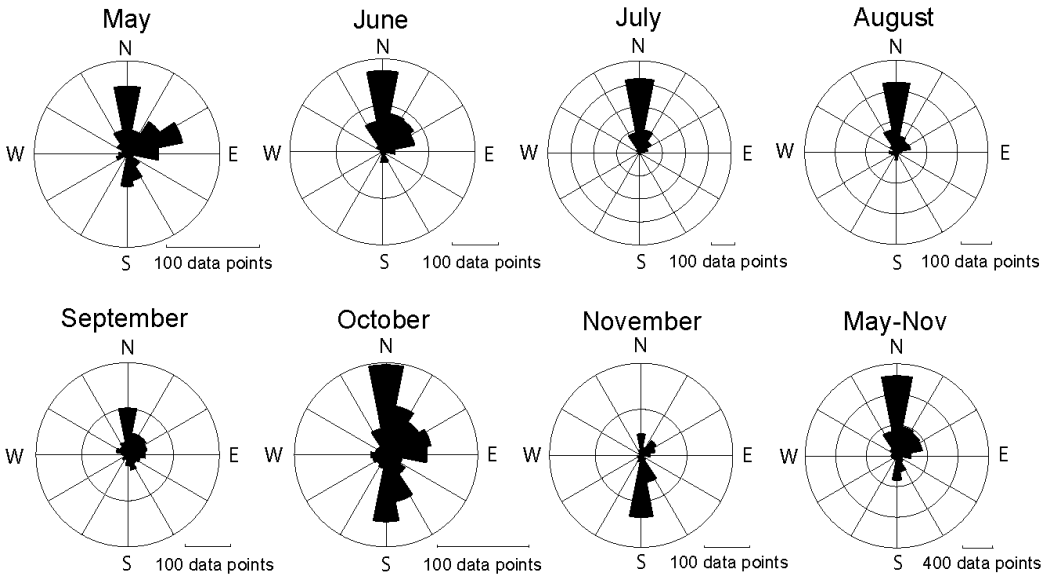

Figure 18: *Rose diagrams showing the downwind azimuths in Blythe, California in 2010. Measurements were taken at a height of 10 meters.*

November 27, 2010). A spline interpolation, using the R statistical software package [*Schultz*, 1973], was used to fill unavailable hourly data points for the Barstow data set. Raw Amboy (Fig. 19a) and Barstow data (Fig. 19b) were iterated 80 times using an exponentially weighted moving average (EWMA) filter [*Rudas*, 2008] to smooth fluctuations (Fig. 19c). Once a trend was graphically observed between the two data sets, a statistical analysis was completed with the smoothed EWMA data to assess a possible correlation. The Pearson correlation [*Kunter et al.*, 2005] technique was applied using SAS (statistical analysis system) to determine the linear dependence between the Amboy and Barstow data sets. Assuming a null hypothesis (that the two data sets are not correlated), the anticipated probability value (p-value) should be high. However, the p-value was determined to be 0.025, indicating the alternative hypothesis (that the data are

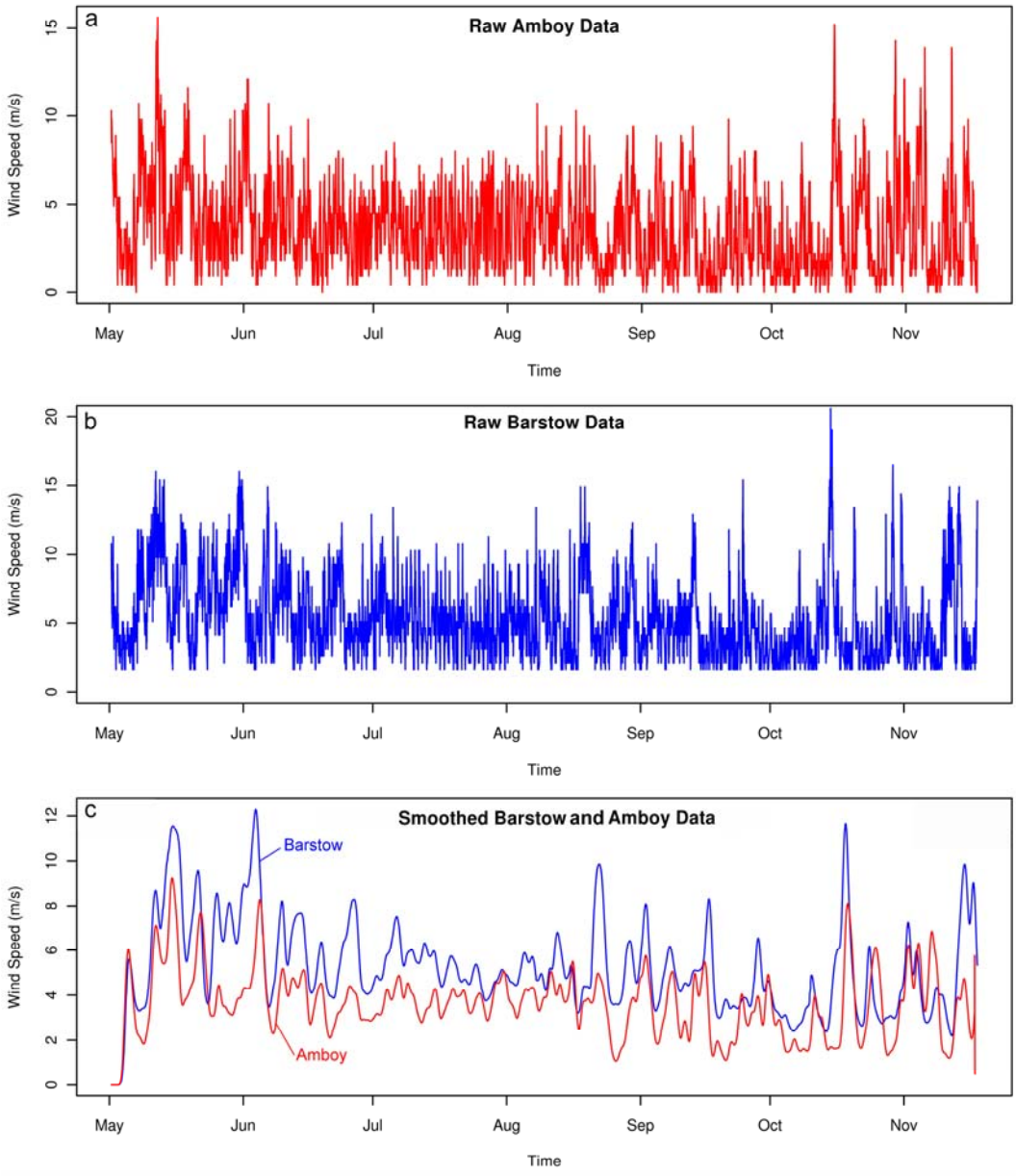

Figure 19: *Wind speeds for May through September 2010 at (a) Amboy field site (height of 0.9 m) and (b) Barstow, California (height of 10 m) and the (c) exponentially weighted moving average (EWMA) data for Amboy compared to Barstow.*

correlated) should be adopted. Thus, the wind speeds at Barstow and Amboy are closely correlated.

Weather data will continue to be collected at the Amboy field site in order to obtain information on seasonal variations in wind speed and direction. Based on the strong correlation between Amboy and Barstow data sets, it is possible to prepare a mathematical model to extrapolate previous Amboy data from archival Barstow weather records. This extrapolation will allow an analysis of long-term weather trends at the field site for comparison to zones of deposition within the craters. Although these long-term weather records are not available, aerial photographs of the area from the 1950s (Fig. 6b), 1970s (Fig. 20-22), and 2006 (Fig. 6a and 6c) allow a preliminary analysis of the stability of winds from the northwest. The large wind streak to the southeast of the cinder cone has changed very little (Fig. 6) and indicates prevailing winds from the northwest have been stable over the 50-year time interval. In addition, wind streaks trending northwest to southeast behind obstacles such as rock piles and bushes are present in the plateau area including streaks within the floors of Craters 6 and 7 (Fig. 20-22) in photographs from the 1970s. These wind streaks indicate prevailing winds from the northwest. Therefore, predominant winds from the northwest are considered to be stable in the area and have likely contributed to the accumulation of sediment in the northwest portion of the crater floors.

2.3 Conclusions

Wind records obtained at the field site in this study and from previous measurements, extrapolations of wind data from Barstow over several decades, and sediment drift patterns over the lava field all indicate that the prevailing sand-

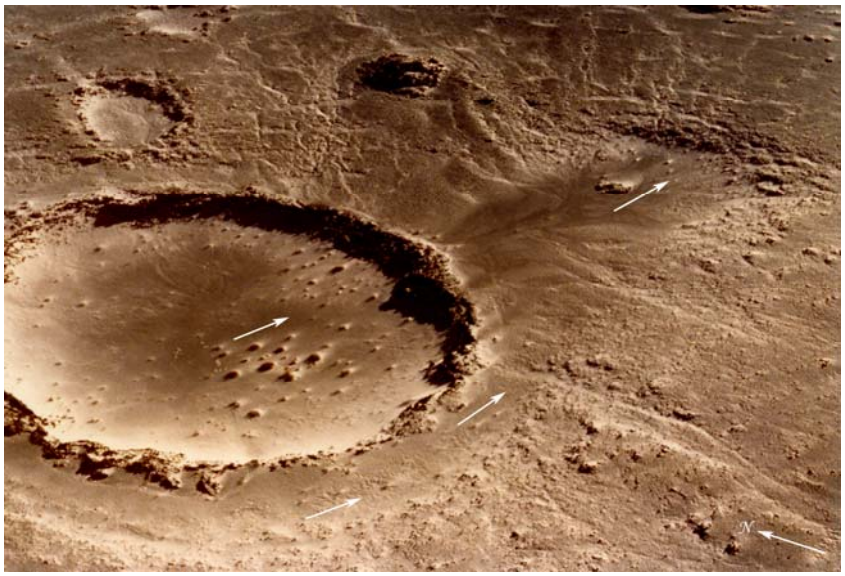

Figure 20: *Aerial photograph of Crater 7 in 1976 with wind streaks (arrows) trending northwest to southeast in the lee of rock piles and bushes indicating predominant winds from the northwest. Wind streaks can be seen on the surrounding terrain and within the crater. Photograph is courtesy of Dr. Ronald Greeley.*

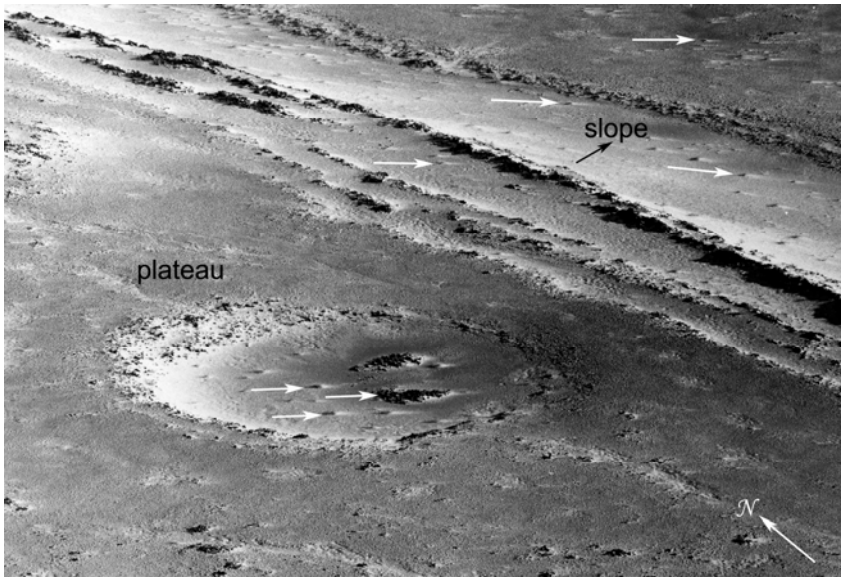

Figure 21: *Aerial photograph of Crater 6 in 1976 with wind streaks (arrows) trending northwest to southeast in the lee of rock piles and bushes indicating predominant winds from the northwest. Wind streaks can be seen on the surrounding terrain and within the crater. The general slope is to the southeast with the edge of the plateau (drop off) in the upper left corner. Photograph is courtesy of Dr. Ronald Greeley.*

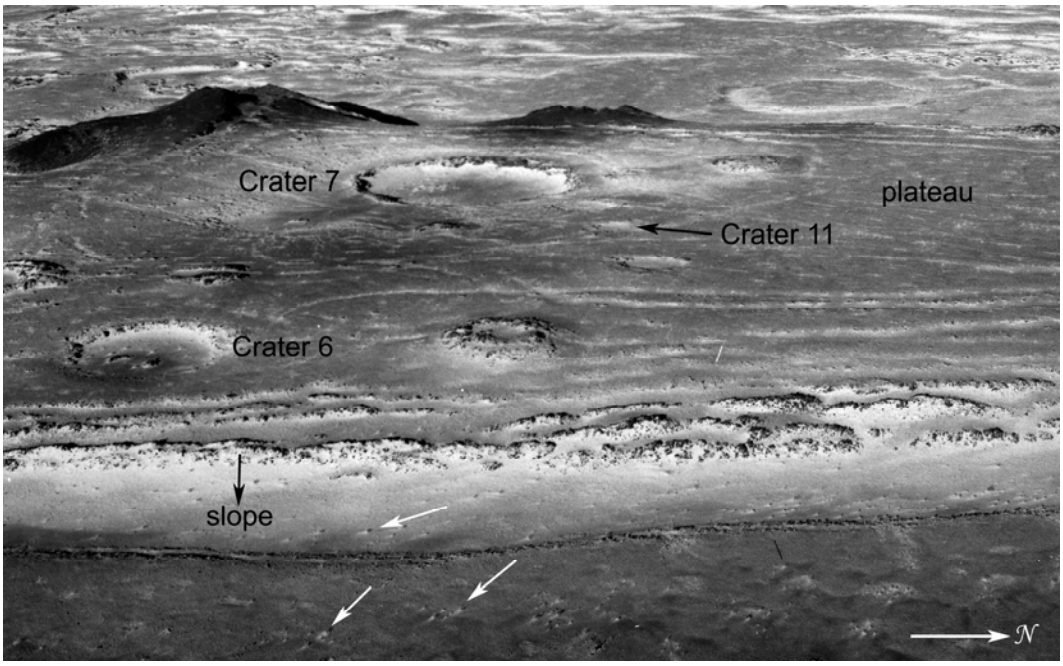

Figure 22: *Aerial photograph of Craters 6, 7, and 11 in 1976 with wind streaks (arrows) trending northwest to southeast in the lee of rock piles and bushes indicating predominant winds from the northwest. The general slope is to the southeast with the edge of the plateau (drop off) in the lower portion of the photograph. Photograph is courtesy of Dr. Ronald Greeley.*

moving winds are from the northwest. Real-time wind observations for Craters 6 and 7 and sediment drift patterns determined from the dyed sand for Craters 6, 7, 11, and 20 suggest that there is reverse wind flow across the floors of the craters. Maps of the distributions of sediments in Craters 6 and 7 also show dominant accumulations of sand on the northwest part of the crater floors, which is interpreted to result from the reverse flow. Although craters contain aeolian deposits on the upwind (relative to the predominant wind direction) side of the crater floor, the results of crater mapping are not conclusive evidence for reverse flow. It is possible that the sediment could be deposited on the downwind side of the crater floors during periods of wind flow from southeast to northwest

(opposite of the predominant wind direction). However, crater mapping coupled with the real-time wind measurements and sediment drift patterns indicate reverse flow.

Craters 6, 7, and 20 have depth-to-diameter ratios ranging from 0.049 to 0.082. In contrast, no reverse flow was observed in Crater 11 in either the real-time wind observations or in sediment drift patterns. This crater has a d/D value of 0.021 which we infer to be too shallow for flow separation, reattachment, and reversal across the floor; rather, the winds and the entrained sediments pass over the crater with no apparent asymmetric deposition within the crater. Consequently, we suggest that craters having a d/D value $\geq$0.05 will experience reverse flow across the floor, resulting in deposition on the upwind zone of the floor. We note that some winds recorded at Amboy in the summer months are from the southeast, which could influence the sediment distributions. We assume, however, that because these winds are not as strong as those from the northwest (average of 3.13 m/s for winds from the east-southeast, southeast, and south-southeast and 4.65 m/s for winds from the west-northwest, northwest and north-northwest for May to November 2010), the movement of sediment from these winds is minimal.

It is also necessary to note the presence of wind gusts which are important sediment-moving processes. According to the National Weather Service Automated Surface Observing System (ASOS) User's Guide Chapter 3 (Appendix A), "...a gust is reported when an observer sees rapid fluctuations in

sensor wind speed indications with a variation of 10 knots or more between peaks and lulls during the 10-minutes before the observation." (p. 16). Gust information for the ASOS weather station at Barstow is available during the May to November 2010 observation period. However, due to the limitations of the weather station located at the Amboy lava field, gust information comparable to that at Barstow is not available. Future research should include wind observation at Amboy over one-minute intervals which would allow a record of gusts for comparison to the Barstow data set.

Chapter 3

WIND TUNNEL SIMULATIONS

Wind tunnel simulations included visual observations of grain movement and depositional patterns within crater models under ideal conditions for comparison to the results of field research with full-scale terrestrial analog craters under natural conditions.

3.1 Approach

Six crater models were produced from acrylonitrile butadiene styrene (ABS), including a scaled model of one endogenic crater from the Amboy lava field, for experimentation in the Arizona State University Planetary Geology Wind Tunnel Facility. This facility consists of a 13.7 m long, 1.2 m wide, 0.7 m high wind tunnel (Fig. 23) in which wind is pulled from outside through two intake chambers and a "bell-mouth" entrance to the test section by a fan at the exit end of the wind tunnel. This design prevents the air from being disturbed by rotating fan blades prior to passage through the test section [*Bagnold,* 1941]. A honeycomb structure at the entrance to the wind tunnel smoothes out eddies; roughness elements (machine nuts) are placed just past this structure to "trip" the air flow and create a boundary layer. The pressure inside the wind tunnel is measured with a pitot which faces the oncoming wind and is connected to a water manometer. The output in inches of water can be used to calculate the free stream velocity (U_∞) inside the wind tunnel with the following equation:

$$U_\infty \text{ (m/s)} = \sqrt{\text{Inches of } H_20} \text{ x } 20.14 \qquad \text{(Eq. 6)}$$

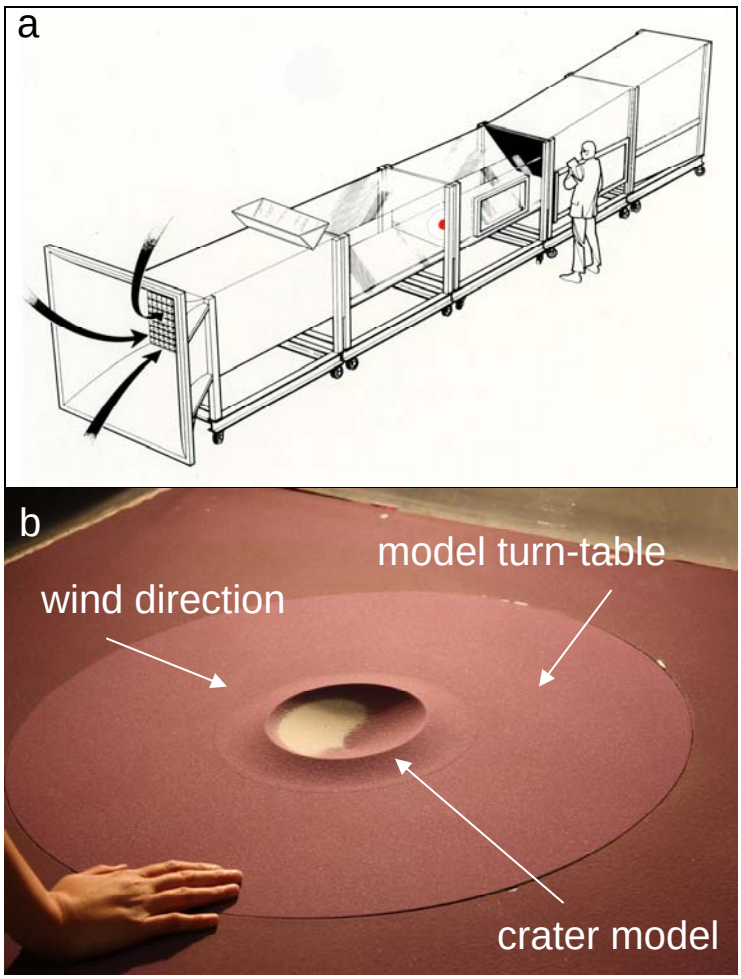

Figure 23: *(a) Arizona State University Planetary Geology Group Wind Tunnel Facility test section with approximate size of crater holder and crater model and (b) enlargement of crater holder and crater model.*

The morphometric properties of each crater model are listed in Table 4. In order to scale the models correctly to the size of the boundary layer and adjust for scaling of grain size and surface roughness, the models were produced with a vertical exaggeration of two [*Iversen et al.,* 1976]. Therefore, the actual rim heights and depths are presented in Table 4 for comparison to the scaled parameters used for d/D calculations. In addition, to simulate the horizontal scale of the craters, the runs were completed at low wind speeds (4 to 9.5 m/s) allowing

multiple grain saltation paths over, around, and within the crater rims and craters. The rim heights were chosen to represent the closest match to the average rim height-to-diameter (r/D) ratio observed for the craters on Mars. Model #1 was constructed to verify the previous results (reverse flow and deposition on the upwind side of the crater floor) of wind tunnel simulations for a deep crater with a pronounced raised rim [*Greeley et al.,* 1974]. Model #2 was constructed to simulate a shallower crater with a pronounced rim. Three of the models (#3, #5, and #6) were constructed with consistent diameters and rim heights but with different depths, which allowed an analysis of wind flow and sediment deposition as a function of the crater d/D ratio. Model #4 was constructed from the topographic profile of the largest endogenic crater at the Amboy field site (Fig. 8). Because this crater has different slopes on each wall, an average was used for the wind tunnel model. In addition, the model contains a flat floor and no pronounced rim raised above the surrounding terrain, as indicated by the topographic profile surveyed in the field. Profiles of the wind tunnel models are included in Fig. 24.

Crater	Depth (m)	Scaled Depth (m)	Diameter (m)	Rim Height (m)	Scaled Rim Height (m)	Scaled Depth/ Diameter Ratio
Model #1	0.032	0.0160	0.152	0.008	0.004	0.110
Model #2	0.020	0.0100	0.152	0.010	0.005	0.065
Model #3	0.013	0.0065	0.152	0.006	0.003	0.043
Model #4 (Amboy)	0.020	0.0100	0.253	0.000	0.000	0.040
Model #5	0.010	0.0050	0.152	0.006	0.003	0.033
Model #6	0.006	0.0030	0.152	0.006	0.003	0.020

Table 4: *Morphometric properties of wind tunnel models including scaled d/D ratio used for comparison to craters in Gusev Crater, Mars.*

A ridge of loose white quartz sand approximately 10 cm high and 35 cm wide was placed 1.2 m upwind of the wind tunnel test section and was roughened to allow the wind to easily move particles downwind. The crater models, crater holder (which allows for rotation of the models with little disturbance to the sediment deposit), and wind tunnel floor were coated with a water-soluble glue and dyed-purple sand in order to provide a rough surface to the floor (Appendix B). In addition, the purple sand provides a contrast between the floor and the white sand depositing within the craters. A grain size of 120 μm was used for the floor and model surface as well as the upwind source of loose sand.

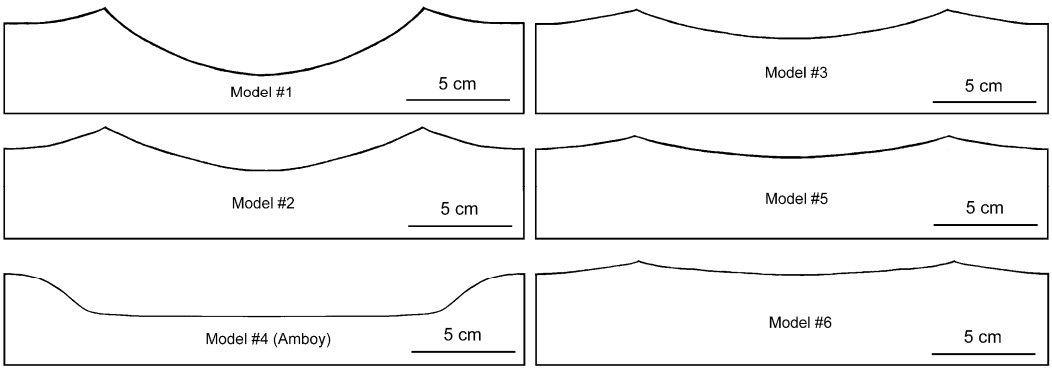

Figure 24: *Wind tunnel crater model profiles.*

During each simulation, the free stream velocity was slowly increased from 2.5 m/s until particles could be seen saltating through the tunnel (generally 4 m/s). This initial velocity was maintained until the unstable particles on the surface of the ridge were moved through the tunnel and the ridge reached equilibrium. At this time, the velocity was increased until particles began saltating. Velocities for these simulations ranged from 4 to 9 m/s (Table 5, Appendix C). The location and amounts of deposition on the floor were visually

observed and documented throughout the simulation. In addition, images of the craters were taken from above the tunnel through the plexiglass roof at intervals of 2-6 hours. These simulations will be referred to as the *deposition runs*.

Once the deposition simulation was complete, the sand upwind of the test section was removed and the models (#1 and #4) were rotated 180 degrees to determine the effect of the opposite wind direction on the deposited material. Due to time constraints, this simulation was only completed for two of the crater models (#1 and #4). These simulations are referred to as the *erosion runs*.

Although the deposition simulations provided overall results for the location of sediment for each crater morphometry, additional simulations were completed to determine how sediment moved in specific areas of the crater floor. A grid of small (8 mm in diameter by 3 mm high), conical sand piles was placed in and around the crater models (Fig. 25). Each pile was visually monitored for particle movement relative to the wind direction. Following this simulation for the first crater (Model #1), this procedure was adjusted to monitor one sand pile at a time for each location in Figure 25. These simulations are referred to as the *grid runs*.

3.2 Results and Discussion

Wind tunnel simulations were completed for six crater models including three models with different d/D ratios (scaled for comparison to craters in Gusev Crater, Mars) and one model scaled to the dimensions of the terrestrial analog crater at the Amboy lava field. During the runs, visual observations of grain

movement (upwind or downwind) were documented for each model. In addition, following each run, the overall location of any visible sediment inside the crater floor or outside the crater model was documented.

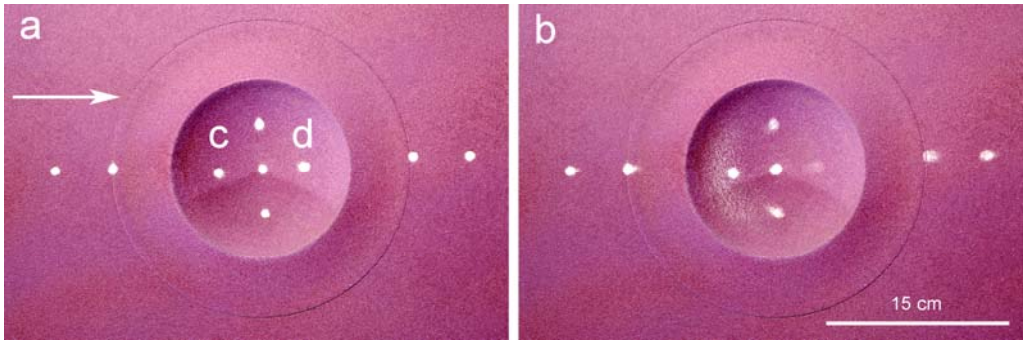

Figure 25: *Image numbers DSC_0366 (a) before and DSC_0378 (b) after for wind tunnel grid run (CA-10-005) with small conical sand piles in crater model #1. All piles outside the crater moved downwind and all piles within the crater moved upwind creating a deposit on the upwind side of the crater floor. Sand pile (c) had little movement and represented an area of nearly stagnant wind while sand pile (d) was eroded and represented an area of significant upwind movement. Illumination, wind direction, and time sequence is from left to right.*

Model #1 was the deepest with a d/D ratio of 0.110. Following the deposition run, sediment was located in the upwind portion of the crater floor (Fig. 26) in an asymmetric crescent pattern, indicating reverse flow. Once the area of deposition was noted, the model was rotated 180° and the erosion run was completed to determine the effect of the opposite wind direction on the deposit. During the erosion run, the sediment was observed migrating back to the upwind side of the crater floor (Fig. 27), indicating the entire crater floor was subject to reverse flow. Following this simulation, the grid run was completed (Fig. 25) to determine the relative areas of erosion and deposition within the crater. Based on the results, the downwind section of the crater floor represented an area of significant erosion which moved sediment in the upwind direction. The upwind

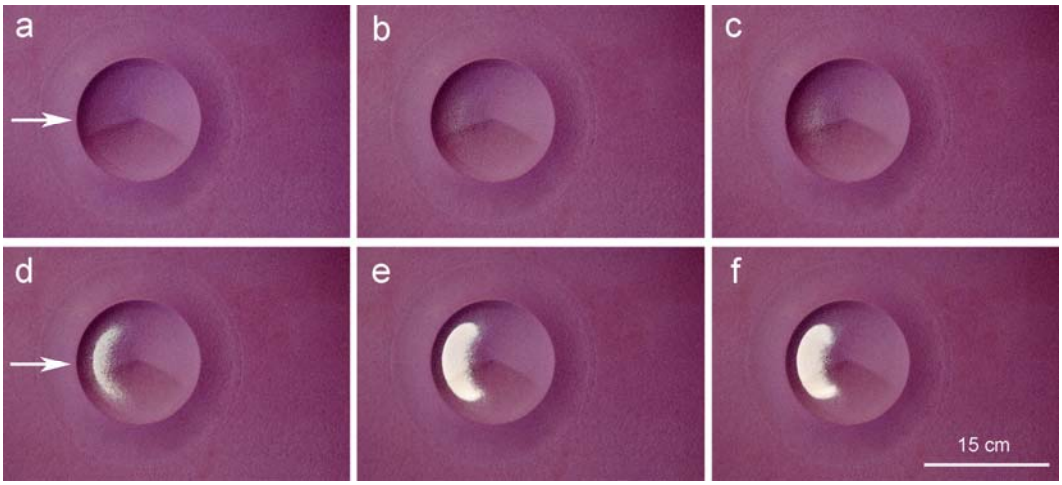

Figure 26: *Image numbers DSC_0038 (a) DSC_0043 (b) DSC_0044 (c) DSC_0052 (d) DSC_0090 (e) and DSC_0155 (f) for wind tunnel erosion run (CA-10-002) with crater model #1 showing sediment on the upwind portion of the crater floor due to reverse flow. Illumination, wind direction, and time sequence is from left to right.*

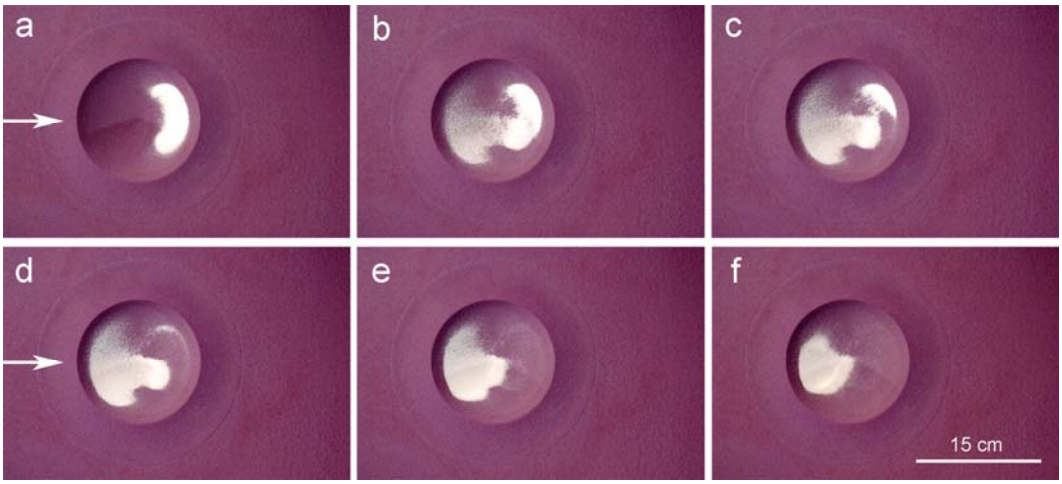

Figure 27: *Image numbers DSC_0038 (a) DSC_0043 (b) DSC_0044 (c) DSC_0052 (d) DSC_0090 (e) and DSC_0155 (f) for wind tunnel erosion run (CA-10-002) with crater model #1 showing sediment on the downwind portion of the crater floor moving back to the upwind side due to reverse flow. Illumination, wind direction, and time sequence is from left to right.*

section of the crater floor represented an area of stagnant wind with little to no sediment movement. Thus, a large eddy of reverse flow occurs in this model causing a large sediment deposit to form on the upwind portion of the crater floor.

Model #2 was the next deepest model with a d/D ratio of 0.065. Following the deposition run, sediment was located in the upwind portion of the crater floor (Fig. 28) in an asymmetric crescent pattern, indicating reverse flow. Visual observations during the grid run indicated the downwind section of the crater floor represented an area of significant erosion which moved sediment in the upwind direction. The upwind section of the crater floor represented an area of stagnant wind with little to no sediment movement. Similar to Model #1, a large eddy of reverse flow occurs in Model #2, causing sediment deposition in the upwind portion of the crater floor.

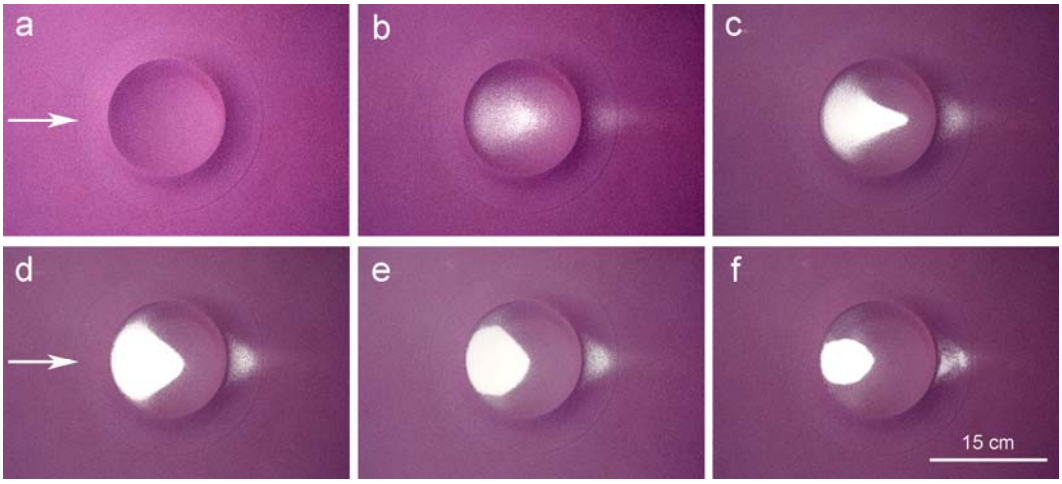

Figure 28: *Image numbers DSC_0040 (a) DSC_0059 (b) DSC_0085 (c) DSC_0101 (d) DSC_0125 (e) and DSC_0172 (f) for wind tunnel erosion run (CA-10-025) with crater model #2 showing sediment on the upwind portion of the crater floor. Illumination, wind direction, and time sequence is from left to right.*

In order to determine how wind patterns and the location of aeolian deposition within craters vary as a function of the d/D ratio, three models with d/D ratios of 0.043 (Model #3), 0.033 (Model #5), and 0.020 (Model #6) were run in the wind tunnel. Each model had the same diameter and rim height with

different depths. Model #3 experienced reverse flow in the upwind portion of the crater floor while downwind movement occurred throughout the rest of the crater. Therefore, the area within the crater experiencing reverse flow for Model #3 was much smaller than that for Model #1. Following the deposition run, a thin deposit was observed on the upwind side of the floor, extending nearly to the middle of the crater floor (Fig. 29). In addition, a small deposit was noted just beyond the downwind crater rim, indicating reverse flow might have occurred in two locations: within the crater due to the upwind crater rim and outside the crater due to the downwind crater rim.

Following the deposition run for Model #5 (d/D ratio = 0.033), a thin layer of sediment was present on the upwind portion of the crater floor (Fig. 30). This deposit was much smaller than that observed for Model #3. However, a slightly larger deposit was noted past the downwind crater rim. During the grid run, all sand piles within the crater floor moved in the downwind direction. However, the sand pile located in the upwind portion of the crater floor had a few unstable grains which moved in the upwind direction at the first sign of grain movement, indicating possible reverse flow. Thus, the area of the crater affected by reverse flow appeared to be nearly non-existent.

Following the deposition run for Model #6 (d/D ratio = 0.020), a very thin layer of sediment was present on the upwind portion of the crater floor (Fig. 31). This deposit was much smaller than previous simulations. In addition, a deposit was observed outside the crater past the downwind crater rim, similar to the

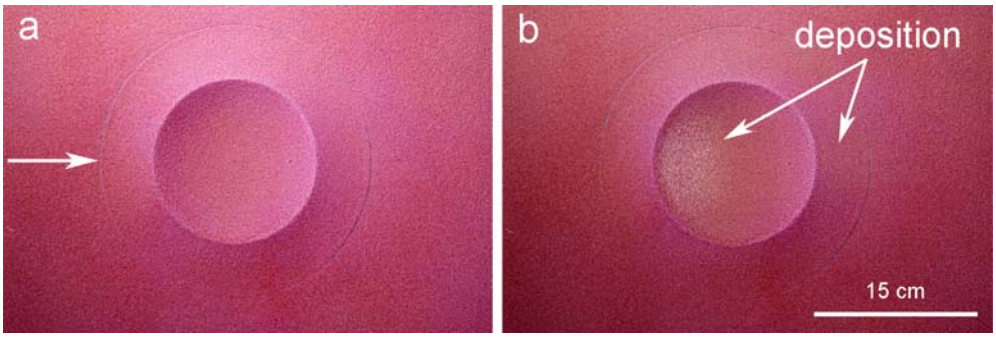

Figure 29: *Image numbers DSC_0086 (a) before and DSC_0371 (b) after for wind tunnel deposition run (CA-10-013) with crater model #3 showing sediment on the upwind part of the crater floor. Illumination, wind direction, and time sequence is from left to right.*

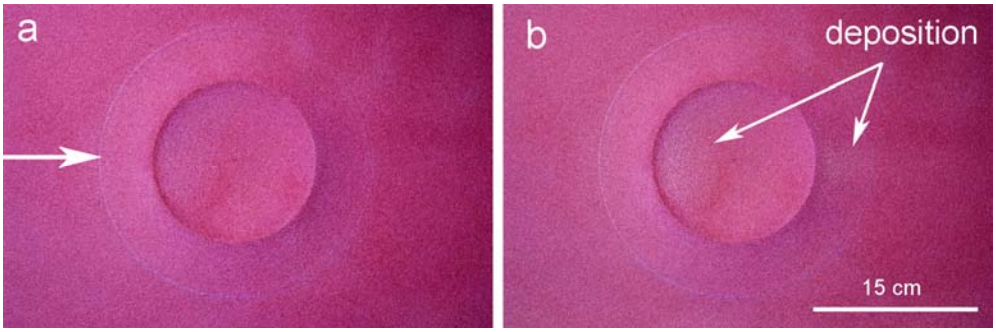

Figure 30: *Image numbers DSC_0193 (a) before and DSC_0359 (b) after for wind tunnel deposition run (CA-10-018) with crater model #5 showing sediment on the upwind portion of the crater floor and just after the downwind crater rim. Illumination, wind direction, and time sequence is from left to right. Note the size of the upwind deposit compared to that in Figure 29.*

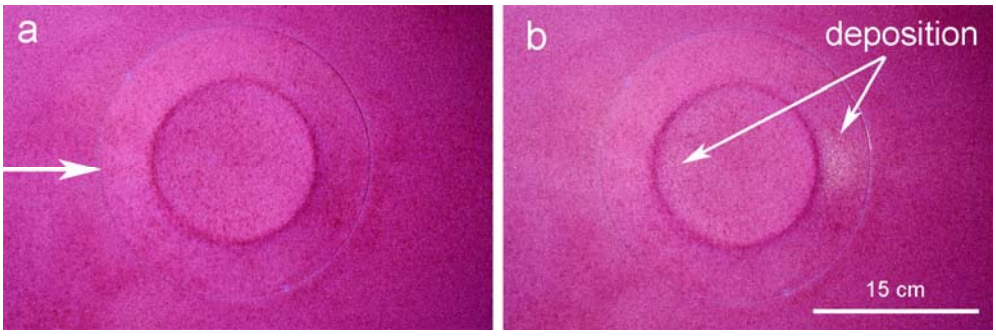

Figure 31: *Image numbers DSC_0030 (a) before and DSC_0137 (b) after for wind tunnel deposition run (CA-10-020) with crater model #6 showing sediment on the upwind portion of the crater floor and just after the downwind crater rim. Illumination, wind direction, and time sequence is from left to right. Note the size of the upwind deposit compared to that in Figures 30 and 31.*

previous simulations with Models #3 and #5. During the grid run for this model, all sand piles within the crater floor moved in the downwind direction, indicating reverse flow does not occur with this crater morphometry. Although this crater does not experience reverse flow, deposition on the upwind side of the crater floor is likely caused by an area of stagnant wind due to the raised rim.

Model #4 simulated a terrestrial analog crater at the Amboy lava field, which has a d/D ratio of 0.040 with a flat floor and no elevated rim above the surrounding terrain. During the deposition run, sediment initially accumulated on the downwind portion of the crater floor. However, over a period of 24 hours, sediment began depositing on the upwind side of the crater floor while no additional sediment deposited on the downwind side. Observations during the run indicated that erosion and deposition were occurring on the downwind side of the floor at the same time while only deposition was occurring on the upwind side. Therefore, over time, an asymmetric depositional pattern similar to that seen for Model #1 formed on the upwind side of the crater floor (Fig. 32).

Following the deposition run, the model was rotated 180° for the erosion run. Sediment that was previously deposited on the upwind side of the crater floor (now on the downwind side) was deflated and removed from the crater. In addition, an asymmetric deposit formed on the upwind side of the crater floor, similar to the deposition run. Thus, the resulting sediment patterns for the deposition and erosion runs were the same. During the grid run, stagnant wind was noted in the upwind section of the crater for wind speeds below 8.0 m/s.

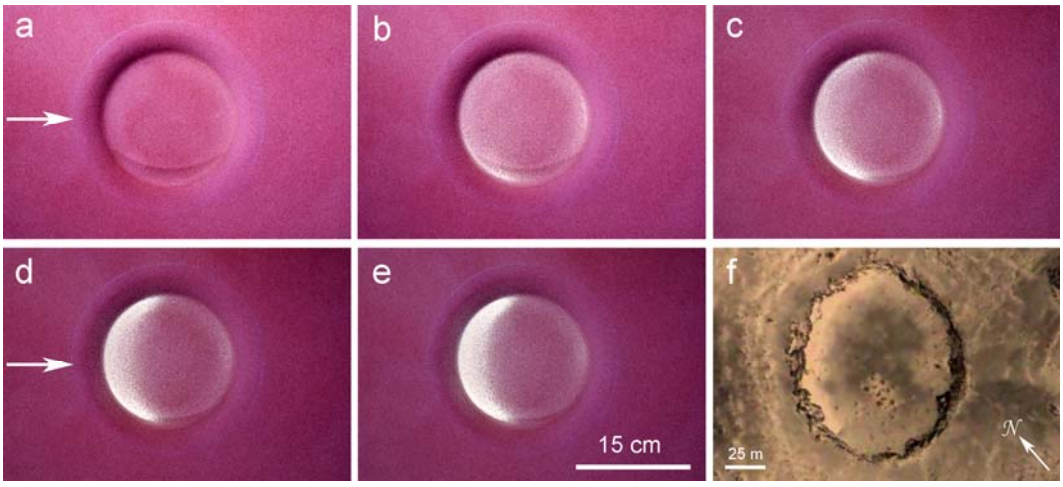

Figure 32: *Image numbers DSC_0054 (a) DSC_0071 (b) DSC_0088 (c) DSC_0105 (d) DSC_0122 (e) and Google Earth image of Crater 7 at the Amboy lava field (f) for wind tunnel deposition run (CA-10-015) with crater model #4 showing sediment on the upwind and downwind portion of the crater floor. Illumination, wind direction, and time sequence is from left to right.*

However, above this wind speed, sediment began to move in the upwind direction, indicating reverse flow occurs for this crater model. All other areas within the crater exhibited downwind sediment movement.

Crater mapping in the Amboy lava field indicated an equal distribution of sand around the edges of the crater floor with active sand deposits in an asymmetric pattern on the upwind side, similar to that observed in the wind tunnel simulation (Fig. 32). Although a more prominent deposit was observed in the upwind portion of the crater during wind tunnel simulation, a small deposit was also observed on the downwind side. With constantly changing wind directions, this deposit could build up over time and result in an equal distribution of sediment around the crater floor, similar to that seen in the field. In addition, the results of the grid run complemented the observations of stagnant wind and occasional reverse flow in the field.

3.3 Conclusions

Based on the results of wind tunnel simulations, reverse flow occurred in five of the six crater models (#1 through #5 with d/D ratios of 0.110 to 0.033) leading to sediment deposition on the upwind portions of the crater floors. Although Model #6 (d/D ratio of 0.020) did not exhibit reverse flow, as indicated by the grid run, a deposit was noted on the upwind portion of the crater floor. Therefore, an area of stagnant wind likely exists in this portion of the crater due to the elevated crater rim. Model #4 (d/D = 0.40) represents a scaled model of an endogenic crater from the Amboy lava field. Although this model did not include a raised rim above the surrounding terrain, reverse flow was observed in the upwind portion of the crater floor during the grid run. Thus, the depth of the crater might play a more important role than the rim height in the presence of reverse flow within craters. Previous field work at Amboy [*Kienenberger and Greeley*, 2011a, b] resulted in an estimation that reverse flow ceases within a d/D range of 0.02 to 0.05. Based on the wind tunnel simulations, reverse flow ceased at a d/D ratio $\leq$0.033. In addition, the area of the crater floor experiencing reverse flow decreases with shallower craters, leading to smaller deposits on the upwind side.

Craters near the Spirit landing site with asymmetric aeolian deposits in the northwest portions of the craters have d/D ratios of 0.034 to 0.076, indicating that reverse flow occurs in these craters. The location of windblown sediments in these craters suggests a prevailing depositional wind from the northwest to the

southeast. Craters with low d/D ratios (<0.03) do not contain asymmetric deposits (Fig. 2), indicating the sediments move directly over the crater floor in the downwind direction. However, the atmospheric pressure and gravity on Mars may play a role in the separation and reattachment of the wind flow. Therefore, these experiments should be conducted under Mars conditions to determine the effect of these parameters on the location and characteristics of the sediment deposits.

Chapter 4

APPLICATION TO MARS

The following section presents morphometric data for small craters (<200 m in diameter) near the Spirit rover landing site and the locations and characteristics of windblown deposits within the craters as seen from HiRISE images for comparison to the results of field studies and wind tunnel simulations. Initial comparisons were used to infer the local predominant wind direction at the time of deposition or redistribution near the Spirit rover landing site.

4.1 Approach

Mars Reconnaissance Orbiter (MRO) HiRISE images of the terrain within Gusev Crater were acquired from the HiRISE website (http://hirise.lpl.arizona.edu). Prospective craters with and without asymmetrically distributed aeolian sediment were chosen in an area of overlap of two HiRISE images forming a stereo pair (Fig. 33). A total of 41 shallow craters with diameters between 50 and 210 meters were selected based upon the availability of topographic data.

Following the selection of craters, one to three topographic profiles across each crater (Fig. 34) were collecting using a digital elevation model (DEM) with a horizontal resolution of 1 m/pixel and vertical resolution of ~0.5 m [*Kirk et al.*, 2008] provided by the United States Geological Survey (USGS), Flagstaff, Arizona. The locations of the profiles were chosen to avoid features around the craters which could affect the morphometry of the impact crater (rim height,

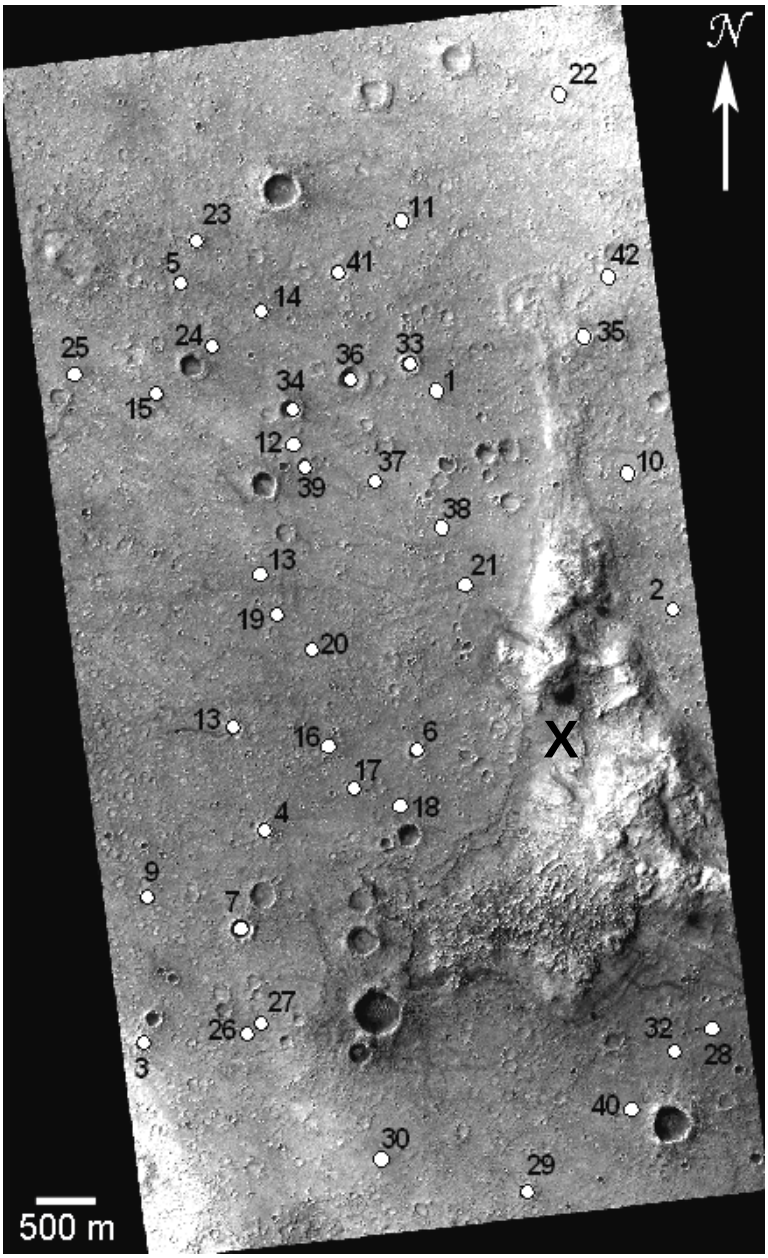

Figure 33: *Area of overlap of Mars Reconnaissance Orbiter High Resolution Imaging Science Experiment (HiRISE) images PSP_001513_1655 and PSP_001513_1655 forming a stereo pair of the Gusev Crater terrain near the Columbia Hills (lower right) with chosen craters. The current location of the Spirit rover is labeled with an X.*

diameter). These features include aeolian bedforms on the northwest portions of the crater rims and areas where subsequent craters were superimposed on the

rims. The topographic profiles were extended onto the surrounding terrain to provide a frame of reference for the morphometry of the crater compared to the slope of the plains.

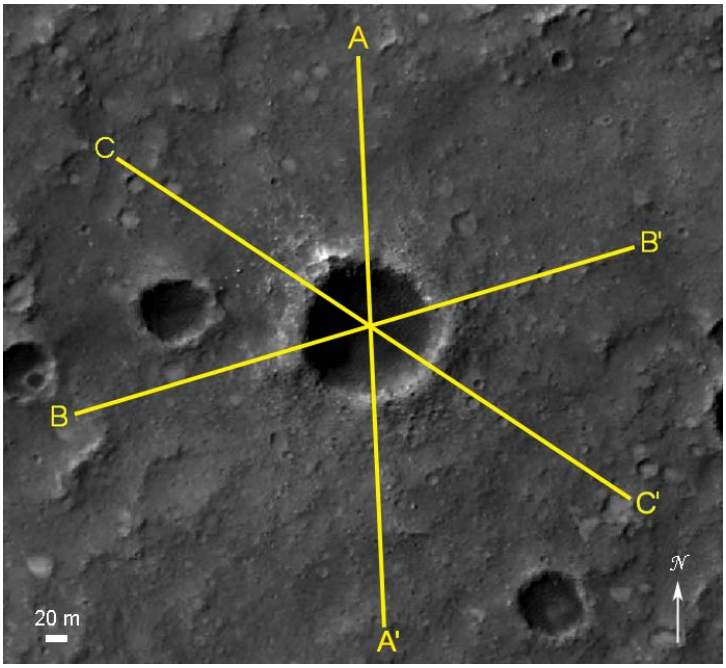

Figure 34: *Location of topographic profiles across Crater 28 near the Spirit landing site in Gusev Crater, Mars.*

To measure the depth for each crater, a line was drawn from rim to rim on the topographic profile. The rim-to-floor depth measurements were taken perpendicularly from this line to the deepest part of the crater floor (Fig. 35) following the method of *Cintala* [1976]. A mean depth for each crater was calculated by averaging the measured depths from each topographic profile across the crater. The rim-to-rim diameter of the crater was obtained by tracing the outline of the crater rim from the HiRISE image and overlaying perfect circles of different sizes to obtain a best-fit circle following the method of *De Hon* [1981]. This diameter measurement will hereafter be referred to as the *circle diameter*.

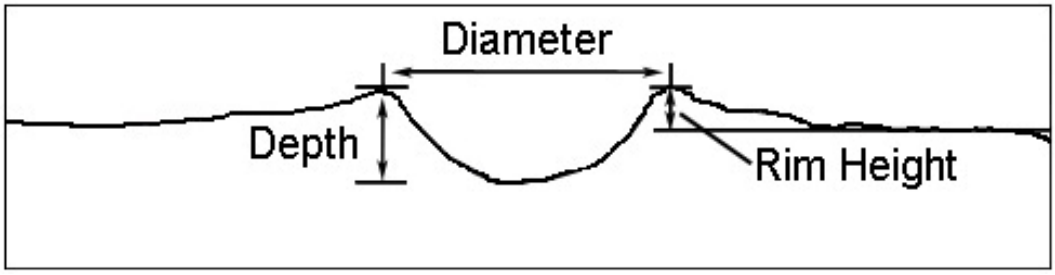

Figure 35: *Crater morphometric parameters including rim-to-rim diameter, rim-to-floor depth, and rim height relative to the average surrounding terrain overlain on a topographic profile of Crater 1 with a vertical exaggeration of 10.*

The center point of the best-fit circle was transferred to the paper with a traced rim of the crater. This point represents the "center of gravity" as defined by *Murray and Guest* [1970]. A total of 32 radii with equal spacing and orientation were drawn from the center of gravity to the crater rim. The equation of *Oberbeck et al.* [1972] was used to calculate the crater circularity:

$$C = 1 + \frac{\sum_{i=1}^{N} | R - r_i |}{NR} \qquad \text{(Eq. 7)}$$

where r_i is equal to the dimension of the ith crater radius measured from the rim to the center of gravity, N is equal to the number of radii measurements, and R is the mean radius, presented in the following equation:

$$R = \sum_{i=1}^{N} \frac{r_i}{N} \qquad \text{(Eq. 8)}$$

Sixteen diameters (using the 32 radii) were averaged to calculate a mean diameter for each crater as a comparison to the results of the circle method described above. This diameter will hereafter be referred to as the *measured diameter*. The crater rim height was measured as the vertical distance from the average surrounding terrain to the crater rim. A mean rim height for each crater

was calculated by averaging the measured rim heights from each topographic profile across the crater. The d/D and rim-to-diameter (r/D) ratios were calculated for each crater using the circle and measured diameters. The morphometric properties of each crater are included in Table 6 (Appendix C).

In addition to the calculation of morphometric properties, a quantitative analysis of aeolian deposition within each crater was conducted. An outline of the location of bedforms present within the craters was traced onto graphing paper. Then, the percentage of the area of the crater floor with bedforms was calculated for comparison to the morphometric properties of the craters. In addition, the average orientations (azimuths) of the bedforms (parallel to the crest) were measured for each crater. These measurements are included in Table 7 (Appendix C).

4.2 Results and Discussion

The collection of morphometric parameters for 41 craters near the Spirit rover landing site in Gusev Crater allowed the calculation of the d/D and r/D ratio for each crater. Based on the data in Table 6 (Appendix C), the crater d/D ratios range from 0.029 to 0.076 with an average of 0.056. Nearly all craters within the data set contained asymmetric deposits of aeolian sediment (Fig. 2) on the northwest portions of the crater floors. However, six craters with d/D ratios <0.045 contained little to no deposits. Terrestrial analog field work at the Amboy lava field including real-time wind measurements and assessments of active sediment deposition in four craters indicated reverse flow or stagnant wind flow

occurs in craters with d/D ratios ≥0.05. Reverse flow is expected to cease within a d/D range of 0.02 to 0.05, resulting in wind movement directly over the crater floor in the downwind direction. In addition, wind tunnel simulations indicated reverse flow occurs in craters with scaled d/D ratios ≥0.033. Visual observations of a crater model with a scaled d/D of ~0.02 did not indicate reverse flow, similar to the results of field studies; therefore, reverse flow appears to cease within a scaled d/D range of 0.02 to 0.033. Based on these results and the calculated crater morphometries and sediment characteristics within the small craters on Mars, reverse flow likely occurs in craters with d/D ratios above 0.045, indicating winds from the northwest.

Wind tunnel simulations show that craters with higher d/D ratios collected more sediment throughout the deposition runs with deposits covering more of the crater floor (Fig. 29 – 31). In addition, during grid runs, deeper craters experienced reverse flow over a larger area of the crater floor. This observation was also noted in the field following sediment drift observations within Crater 20 (highest d/D ratio) indicating upwind sediment movement throughout the entire crater floor. Therefore, it appears that deeper craters experience more reverse flow leading to larger deposits on the crater floors because it is more difficult for sediment to escape the crater. The quantitative analysis of bedforms for craters on Mars indicated a direct correlation between the d/D ratio and the percentage of the area of the crater floor that is covered with bedforms (Fig. 36). There did not appear to be a strong correlation between the r/D ratio and the percentage of the

area of the crater floor with bedforms (Fig. 36) based on the R^2 (coefficient of variation) value of 0.44. According to *Steel and Torrie* [1960], the R^2 value indicates a measure of the goodness of fit for the regression line with a perfect correlation between data sets when $R^2 = 1$. Wind tunnel simulations with the shallowest model (Model #6, d/D ratio = 0.020), indicated a slight asymmetric distribution of sediment on the upwind side of the crater floor without reverse flow. This could indicate that the rim height plays a minor role in the location and/or amount of windblown sediments within craters. Therefore, future work should include a systematic analysis of the rim height to determine the impact of this morphometric parameter on the deposits within the crater floor.

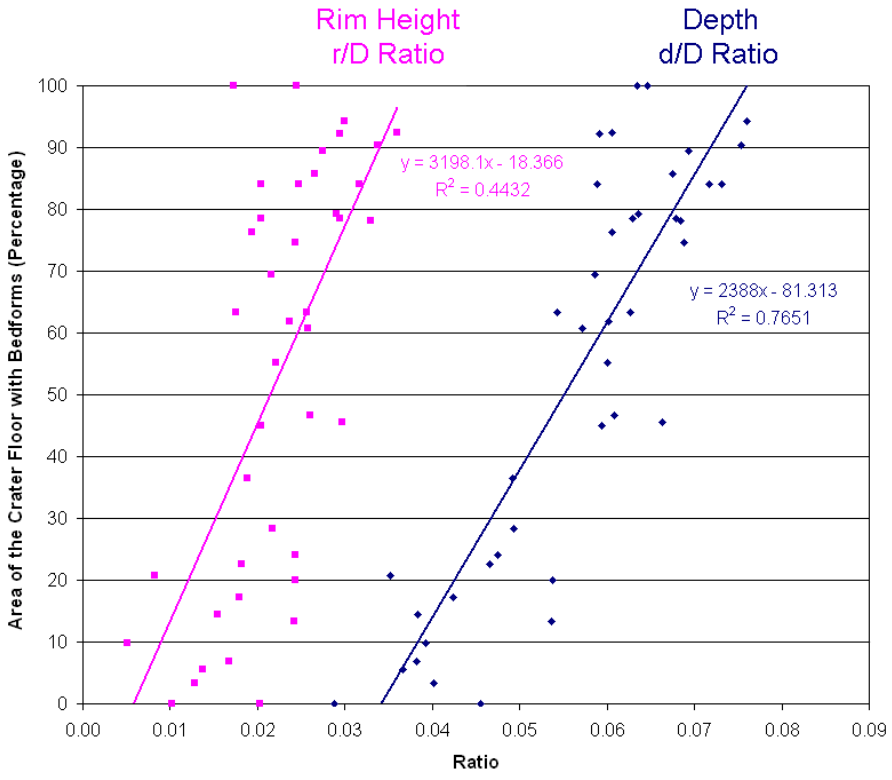

Figure 36: *depth-to-diameter (d/D) ratio and rim height-to-diameter (r/D) ratio vs the area of the crater floor (percentage) with bedforms for 41 craters near the Spirit landing site in Gusev Crater, Mars.*

Wind flow over topography can have many different forms, including flow over a negative step or backward-facing step (slope facing away from the predominant wind direction) such as a scarp (Fig. 37). If wind tunnel simulations indicate the rim height does not play a significant role in the depositional patterns within craters, the method presented here (sediment deposition as a function of depth) could be expanded to include areas on Mars with rimless depressions or negative steps.

Backward-facing step systems have been studied in great detail in fluid dynamics [*Eaton and Johnson,* 1981; *Schetz and Fuhs*, 1999]. As wind moves over a backward-facing step, the boundary layer detaches to form a shear layer which reattaches at a length L (reattachment length). Due to a strong adverse pressure gradient, an area of reverse flow is formed upwind of the reattachment length [*Schetz and Fuhs*, 1999]. According to *Schetz and Fuhs* [1999], L is influenced by the state of the boundary layer (laminar, turbulent) before detachment. For laminar flow, L is generally 6-6.5 times the step-height, h, compared to 7.5 times for highly turbulent flow. In addition, when there is an increase in the overall adverse pressure gradient, as is expected in areas with reverse flow, the length of reattachment increases [*Schetz and Fuhs*, 1999]. Although L in laminar flow is greatly influenced by the Reynold's number, it is relatively constant (~7.5) when air flow is turbulent [*Schetz and Fuhs*, 1999], indicating that the atmospheric density and kinematic viscosity do not play a significant role in the reattachment length.

The estimated reattachment lengths for the craters on Mars were measured as the distance from the northwest crater rim to the farthest extent of bedforms within the crater (Table 8, Appendix C). Based on these measurements, many of the reattachment lengths are much higher than those estimated for turbulent flow [*Eaton and Johnston*, 1981], with an average L of 8.14. This could be due to the presence of the far crater wall, which is not included in the backward-facing step model. As air is deflected back up the crater wall, this could increase the area available for reattachment (Fig. 37), in turn allowing for longer reattachment lengths. In addition the atmospheric pressure on Mars is less than one-hundredth of the pressure at sea level on Earth and the gravity on Mars is 38% that of the Earth which could play a role in the reattachment lengths. Overall, it appears as the simple backward-facing step model may not be applicable to a crater, which is likely more complex in nature.

Future research should include an evaluation of the backward-facing step model in the wind tunnel under terrestrial and Mars conditions and through computer modeling to determine the necessary parameters for reverse flow (fluid velocity, step-height, angle of slope, etc.) over a step as well as how the parameters affect the reattachment length. These parameters can then be compared to craters on Mars to determine which craters should experience reverse flow given their wall slopes and d/D ratios. It is important to note that two craters with different wall slopes (Fig. 38) could have the same d/D ratio which may play an important role in the wind flow over the crater. Therefore, wind tunnel

simulations with craters models exhibiting different wall slopes should be conducted to determine the effect of this parameter on the patterns of deposition.

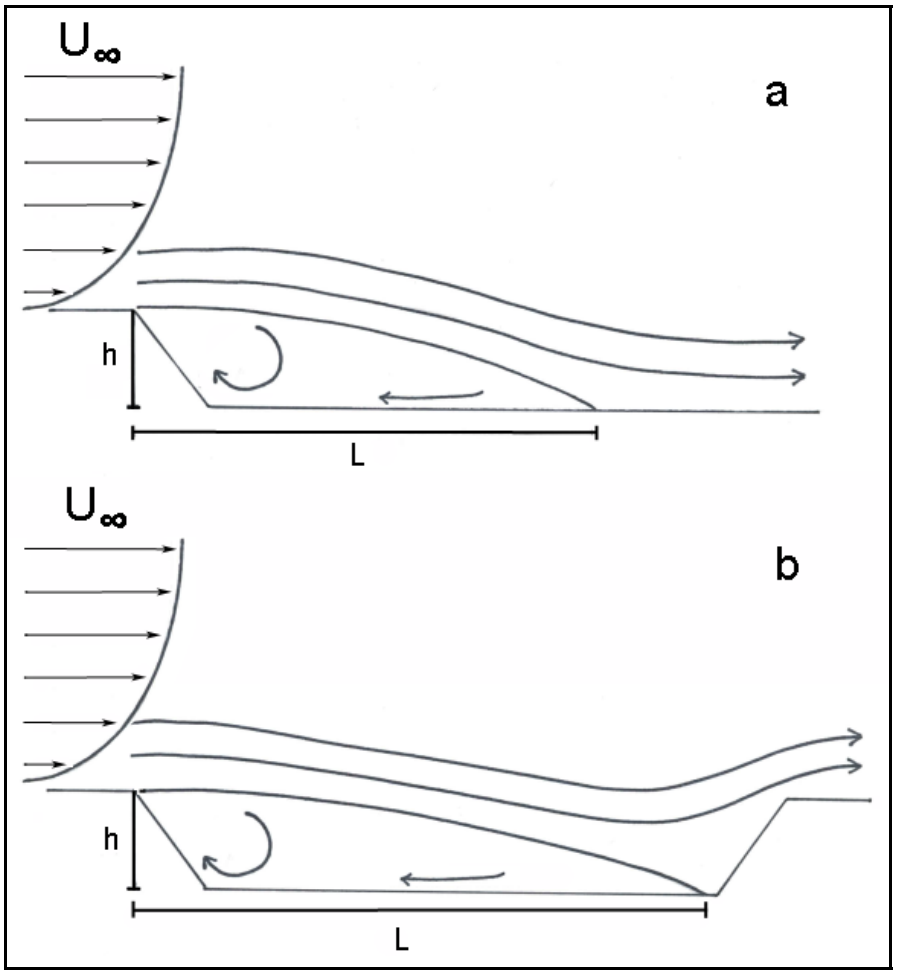

Figure 37: *(a) Flow separation and reattachment over a negative step or backward-facing step and (b) flow separation with estimated reattachment within a crater. Adverse pressure gradients cause reverse flow in both scenarios. L, h, and U_∞ represent the reattachment length, step height, and fluid velocity, respectively.*

The eastern edge of the pressure plateau at the Amboy lava field (Fig. 21 and 22) provides an analog for the backward-facing step model under natural conditions. The terrain slopes to the east with active sediment against the wall indicating deposition due to stagnant wind or reverse wind flow. Future field

research should include real-time wind measurements and sediment drift observations in this area with dyed sand piles to determine if reverse flow exists due to the slope of the terrain.

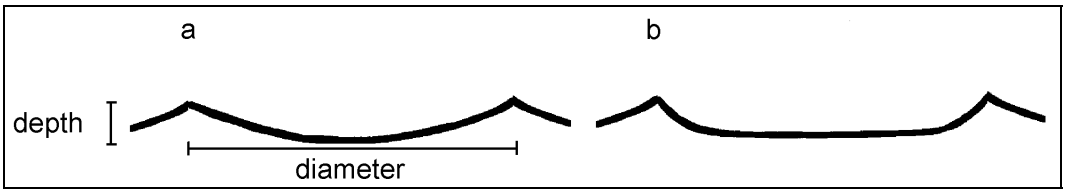

Figure 38: *(a) Crater with low angle wall slopes and (b) crater with high angle wall slopes with the same d/D ratio.*

Crater circularities were calculated for Amboy and Gusev craters to determine if the shape of the crater affected the location/amount of bedforms within craters. Based on these calculations, the Amboy craters had circularity values ranging from 1.02 to 1.20 with an average of 1.1 while Gusev craters ranged from 1.02 to 1.09 with an average of 1.05 (Table 6, Appendix C). Therefore, the craters in Gusev were generally more circular in shape than the endogenic craters at the Amboy lava field. However, there did not appear to be any correlation between the circularity of the craters and the presence of bedforms or their characteristics for either location. Although circularity could have important implications for the origin of a crater (endogenic, exogenic), these preliminary results suggest that circularity does not play a major role in sediment distributions within craters. Further research including a detailed study of crater circularities for larger craters than those found in Gusev as well as wind tunnel simulations with scaled models should be conducted to expand the data set used or determining the role of circularity in the distribution of sediment within craters.

In addition to the bedforms located within the craters on Mars, bedforms on the surrounding plains are visible. Measurements across one bedform, Serpent, indicated the slip face with an angle of 32° (angle of repose) was located on the southeast side of the bedform, indicating winds from the northwest [*Greeley et al.*, 2008]. In addition, larger bedforms termed "rim ripples" [*Sullivan et al.*, 2008] are often located on the northwest portions of the crater rims and are bright (high albedo) in HiRISE images. Two opposing hypotheses have been presented for the formation of these bedforms, including winds from the northwest or southeast. Although no direct measurements have been made across the crater rim bedforms, they appear slightly asymmetric (Fig. 2) with an apparent slip face on the southeast side, suggesting prevailing winds from the northwest. The presence of the bedforms on the northwest part of the crater rim could be due to the increased energy needed to move sediment up and onto the crater rim, resulting in deposition. However, if the crater rim bedforms receive enough energy, they could feed sediment to the craters. In contrast, *Sullivan et al.* [2008] suggest rare, strong winds (4-5 m/s) from the southeast cause bedform migration from within the craters up and over the northwest crater rim. Once the bedforms have migrated out of the crater, they stall in a saltation trajectory shadow and accumulate over time. With the current available data, it is not possible to determine which of the hypotheses involving the rim bedforms is correct. However, it is important to note that with additional topographic information, their presence could likely provide additional support for either case.

Bedforms located on the plains between craters appear symmetric in HiRISE images and are oriented west-southwest to east-northeast based on the crest axis of the bedform. *Greeley et al.* [2006a] suggest winds blow perpendicular to the axis, from northwest to southeast due to a slight asymmetry (slip face on the southeast side) of the bedform "Serpent" as measured by the Spirit rover. However, linear bedforms can also occur, forming parallel to the resultant direction of two wind directions (Fig. 39), which could indicate winds from the northwest and southwest. Although linear bedforms are possible in this area, there is not strong evidence (wind tails, facets, grooves, etc) to suggest formative winds from the west/southwest. Increased topographic resolution across these bedforms and/or additional data collection from rovers in the plains area is needed to determine the winds necessary to form these features.

4.3 Conclusions and Future Research

Terrestrial analog field work at the Amboy lava field, Mojave Desert, California, included real-time wind measurements and assessments of active sediment deposition in four small (<100 m) craters. Results indicate that reverse flow or stagnant wind and deposition on the upwind side of the crater floor occurs in craters with d/D ratios ≥0.05. Reverse flow is expected to cease within a d/D range of 0.02 to 0.05, resulting in wind movement directly over the crater floor in the downwind direction with no asymmetric sediment deposit.

Wind tunnel simulations indicated reverse flow in craters with d/D ratios ≥0.033, resulting in sediment deposition in the upwind portion of the crater floor.

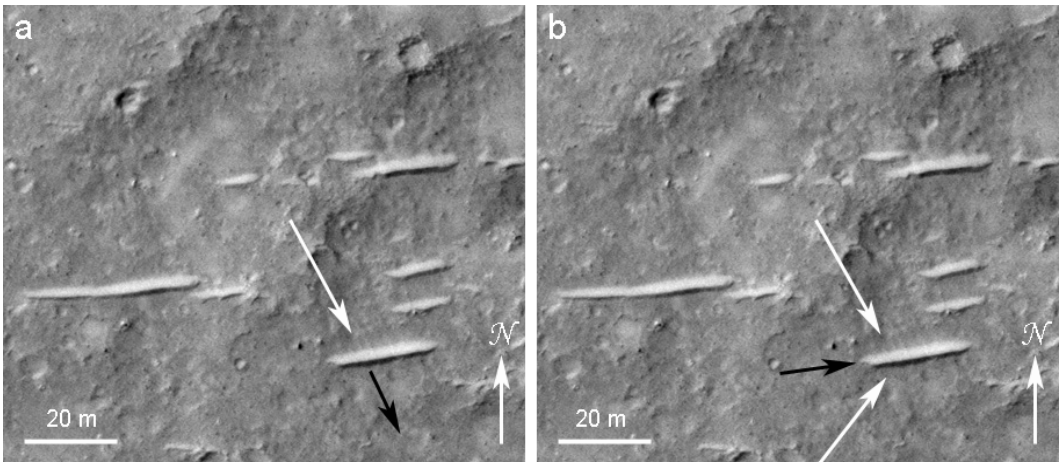

Figure 39: *Mars Reconnaissance Orbiter High Resolution Imaging Science Experiment (HiRISE) image (PSP_001513_1655) showing bedforms on the plains near the Spirit landing site in Gusev Crater, Mars. White arrows indicate the wind direction associated with a) transverse bedforms (forming perpendicular to the prevailing wind from the northwest) and b) linear bedforms (forming parallel to the overall direction of two competing wind directions from northwest and west). Black arrows indicate the direction of bedform migration.*

Craters with asymmetric aeolian deposits near the Mars Spirit landing site have d/D ratios of 0.034 to 0.076, suggesting reverse flow occurs in these craters. Thus, the position of windblown sediments in the northwest part of the crater floors indicates prevailing winds during deposition or redistribution of sediments was from the northwest to the southeast, consistent with late afternoon winds as predicted by the MRAMS circulation model.

This research has provided the initial analysis of sediment deposition as a function of crater morphometry. Future work should include the following:

1. Continued monitoring of the weather at the Amboy field site with the Davis Vantage Vue Weather Station. The initial results of a statistical correlation between Barstow and Amboy suggest the wind speed data are highly correlated. Therefore, continued monitoring over a period of 1-2 years will

allow for an analysis of seasonal variations and could yield a model for extrapolating historical Amboy data from the archival Barstow records.

2. Wind observation at Amboy over one-minute intervals which would allow a record of gusts for comparison to the Barstow data set.
3. An analysis of the sand-moving winds at the Amboy field site. Wind speeds during periods of active sand movement should be recorded from field observations to obtain a range of wind speeds necessary for saltation. These data should be compared to the wind speeds collected and extrapolated from the computational model in 1 (above) to determine the amount of time Amboy is experiencing active sediment movement, if there are changes over seasons, and what direction the active sediment-moving winds are from.
4. Wind tunnel simulations and computer modeling under terrestrial and Mars conditions for a backward-facing step model to determine the parameters necessary for reverse flow. In addition, field studies should include real-time wind measurements and sediment drift observations near the eastern edge of the pressure plateau for comparison to wind tunnel simulations.
5. Wind tunnel simulations with three craters, including a significant raised rim, slightly raised rim, and no rim should be conducted to determine the location and characteristics of deposition within craters as a function of rim height. Additionally, systematic analyses of crater wall slope and the sharpness of the crater rim should be completed to determine the implications of these parameters on wind flow over craters. The wind tunnel simulations presented

in this research should be conducted under Mars conditions to determine the effect of atmospheric pressure and gravity on the sediment deposits.

6. All models should be rotated 90 degrees and 180 degrees following the deposition runs to determine the effect of different wind directions (erosion, redistribution) on the sediment.
7. An analysis of the effect of crater circularity on deposition should be conducted in the wind tunnel to determine the effect of crater shape on the location and characteristics of sediment distribution within craters.

Aeolian processes are common on the surface of Mars and can lead to a determination of wind direction from features such as wind streaks and bedforms. These geologic features can then be used to confirm wind directions estimated with atmospheric modeling techniques (MGGM, MRAMS). However, if bedforms and wind streaks are absent or ambiguous in shape, the technique presented in this paper can be used to determine local wind patterns. In addition, this technique allows for an analysis of the wind patterns on the scale of meters rather than kilometers and could be used for researching wind flow around small scale features such as hills. Although the future work listed above would enhance the findings of this research, the technique used to determine wind patterns will not be affected and should be extended to other areas of Mars with similar features.

REFERENCES

Adler, J. E. M and J. W. Salisbury (1969), Circularity of Lunar Craters, *Icarus* 10, 37 – 52.

Arvidson, R. (1974), Wind-Blown Streaks, Splotches, and Associated Craters on Mars: Statistical Analysis of Mariner 9 Photographs, *Icarus* 21, 12 – 27.

Arvidson, R. (1979), Changes at the Viking Landing Sites over Short and Long Timescales, *Lunar and Planet. Sci. X*, Abstract 1019.

Bagnold, R. A. (1941), *The Physics of Blown Sand and Desert Dunes*, Methuen and Co., London, England.

Bellucci, G., F. Altieri, J. P. Bibring, and the OMEGA Team (2004), The OMEGA Instrument on board Mars Express: First results, *Memorie della Societa Astronomica Italiana Supplement*, Vol. 5, 27 – 32.

Boyce, J. M., P. Mouginis-Mark, and H. Garbeil (2004), Predicted Effects of Surface Processes on Martian Impact Crater Depth/Diameter Relationships, *Lunar and Planet. Sci. XXXV*, Abstract 1816.

Boyce, J. M., P. Mouginis-Mark, H. Garbeil, and L. L. Tornabene (2005), Ancient oceans in the northern lowlands of Mars: Evidence from impact crater depth/diameter relationships, *J. of Geophys. Res.,* Vol. 110(E03008), doi:10.1029/2004JE002328.

Boyce, J. M., P. Mouginis-Mark, H. Garbeil, and L. L. Tornabene (2006), Deep impact craters in the Isidis and southwestern Utopia Planitia regions of Mars: High target material strength as a possible cause, *Geophys. Res. Lett.,* Vol. 33(L06202), doi:10.1029/2005GL024462.

Bridges, N. T., P. E. Geissler, A. S. McEwen, B. J. Thomson, F. C. Chuang, K. E. Herkenhoff, L. P. Keszthelyi, and S. Martinez-Alonso (2007), Windy Mars: A dynamic planet as seen by the HiRISE camera, *Geophys. Res. Lett.*, Vol. 34(L23205), doi:10.1029/2007GL031445.

Christensen, P.R., B.M. Jakosky, H.H. Kieffer, M.C. Malin, H.Y. McSween, Jr., K. Nealson, G.L. Mehall, S.H. Silverman, S. Ferry, M. Caplinger, and M. Ravine (2004), The Thermal Emission Imaging System (THEMIS) for the Mars 2001 Odyssey Mission, *Space Science Reviews*, 110, 85 – 130.

Christensen, P. R. and S. W. Ruff (2004), Formation of the hematite-bearing unit in Meridiani Planum: Evidence for deposition in standing water, *J. of Geophys. Res.*, Vol. 109(E08003), doi:10.1029/2003JE002233.

Cintala, M. J., J. W. Head, and T. A. Mutch (1976), Martian crater depth/diameter relationships: Comparison with the Moon and Mercury, *Proc. Lunar Sci. Conf XII*, 3575 – 3587.

Cutts, J. A. and R. S. U. Smith (1973), Eolian deposits and dunes on Mars, *J. of Geophys. Res.*, Vol. 78, 4139 – 4154.

De Hon, R. A. D (1981), Selenographic distribution of apparent crater depth, *Proc. Lunar Planet. Sci.,* 12B, 639 – 650.

Eaton, J. K. and J. P. Johnson (1981), A Review of Research on Subsonic Turbulent Flow Reattachment, *American Institute of Aeronautics and Astronautics*, Vol. 19(9), 1093 – 1100.

Edgett, K. S., and M. C. Malin (2000), New Views of Mars Aeolian Activity, Materials, and Surface Properties: Three Vignettes From the Mars Global Surveyor Mars Orbiter Camera, *J. of Geophys. Res.*, Vol. 105, 1623 – 1650.

Fenton, L. K. (2006), Dune migration and slip face advancement in the Rabe Crater dune field, Mars, *Geophys. Res. Lett.*, Vol. 33(L20201), doi:10.1029/2006GL027133.

Fenton, L. K., J. L. Bandfield, and A. W. Ward (2003), Aeolian processes in Proctor Crater on Mars: Sedimentary history as analyzed from multiple data sets, *J. of Geophys. Res.*, Vol. 108(E12), 5129, doi:10.1029/2002 JE002015.

Garvin, J. B., S. H. Sakimoto, J. J. Frawley, and C. Schnetzler (2000), North Polar Region Craterforms on Mars: Geometric Characteristics from the Mars Orbiter Laser Altimeter, *Icarus* 144, 329 – 352.

Golombek, M. P., R. A. Cook, T. Economou, W. M. Folkner, A. F. C. Haldemann, P. H. Kallemeyn, J. M. Knudsen, R. M. Manning, H. J. Moore, T. J. Parker, R. Rieder, J. T. Schofield, P. H. Smith and R. M. Vaughan (1997), Overview of the Mars Pathfinder Mission and Assessment of Landing Site Predictions, *Science*, Vol. 278, 1743 – 1748, doi:10.1126/science.278.5344.1743.

Golombek, M. P., L. S. Crumpler, J. A. Grant, R. Greeley, N. A. Cabrol, T. J. Parker, J. W. Rice Jr., J. G. Ward, R. E. Arvidson, J. E. Moersch, R. L. Fergason, P. R. Christensen, A. Castaño, R. Castaño, A. F. C. Haldemanm, R. Li, J. F. Bell III, and S. W. Squyres (2006a), Geology of the Gusev cratered plains from the Spirit rover transverse, *J. of Geophys. Res.*, Vol. 111(E02S07), doi:10.1029/2005JE002503.

Golombek, M. P., J. A. Grant, L. S. Crumpler, R. Greeley, R. E. Arvidson, J. F. Bell III, C. M. Weitz, R. Sullivan, P. R. Christensen, L. A. Soderblom, and S. W. Squyres (2006b), Erosion rates at the Mars Exploration Rover landing sites and long-term climate change on Mars, *J. of Geophys. Res.*, Vol. 111(E12S10), doi:10.1029/2006JE002754.

Golombek, M. P., J. A. Grant, T. J. Parker, D. M. Kass, J. A. Crisp, S. W. Squyres, A. F. C. Haldemann, M. Adler, W. J. Lee, N. T. Bridges, R. E. Arvidson, M. H. Carr, R. L. Kirk, P. C. Knocke, R. B. Roncoli, C. M. Weitz, J. T. Schofield, R. W. Zurek, P. R. Christensen, R. L. Fergason, F. S. Anderson, and J. W. Rice Jr. (2003), Selection of the Mars Exploration Rover landing sites, *J. of Geophys. Res.*, Vol. 108(E12), 8072, doi:10.1029 /2003JE002074.

Grant, J. A., R. E. Arvidson, L. S. Crumpler, M. P. Golombek, B. Hahn, A. F. C. Haldemann, R. Li, L. A. Soderblom, S. W. Squyres, S. P. Wright, and W. A. Watters (2006), Crater gradation in Gusev crater and Meridiani Planum, Mars, *J. of Geophys. Res.*,Vol. 111(E02S08), doi:10.1029/2005 JE002456.

Grant, J. A. and P. H. Shultz (1987), Possible Tornado-Like Tracks on Mars, *Science*, Vol. 237, 883-885.

Greeley, R., R. E. Arvidson, P. W. Barlett, D. Blaney, N. A. Cabrol, P. R. Christensen, R. L. Fergason, M. P. Golombek, G. A. Landis, M. T. Lemmon, S. M. McLennan, J. N. Maki, T. Michaels, J. E. Moersch, L. D. V. Neakrase, S. C. R. Rafkin, L. Richter, S. W. Squyres, P. A. de Souza Jr., R. J. Sullivan, S. D. Thompson, and P. L. Whelley (2006a), Gusev crater: Wind-related features and processes observed by the Mars Exploration Rover Spirit, *J. of Geophys. Res.*, Vol. 111(E02S09), doi:10.1029/2005JE002491.

Greeley, R., M. R. Balme, J. D. Iversen, S. Metzger, R. Mickelson, J. Phoreman, and B. White (2003), Martian dust devils: Laboratory simulations of particle threshold, *J. Geophys. Res.*, 108(E5), doi:10.1029/2002JE001987.

Greeley, R. and J. D. Iversen (1978), Field guide to Amboy lava flows, San Bernardino County, California, in *Aeolian Features of Southern California: A comparative planetary geology guidebook,* NASA, 24-52.

Greeley, R. and J. D. Iversen (1987), *Wind as a Geological Process on Earth, Mars, Venus, and Titan*, Cambridge Univ. Press, New York.

Greeley, R. and J. D. Iversen (1986), Aeolian processes and features at Amboy Lava Field, California, in *Physics of desertification*, edited by F. El-Baz, and M. H. A. Hassan, 290 – 317, Martinus Nijhof, The Hague.

Greeley, R., J. D., Iversen, J. B. Pollack, N. Udovich, and B. White (1974), Wind tunnel studies of Martian aeolian processes, *Proc. R. Soc. Lond. A.*, 341, 331 – 360.

Greeley, R., M. D. Kraft, R. O. Kuzmin, and N. T. Bridges (2000), Mars Pathfinder landing site: Evidence for a change in wind regime from lander and orbiter data, *J. of Geophys. Res.*, Vol. 105, 1829 – 1840.

Greeley, R., M. Kraft, R. Sullivan, G. Wilson, N. Bridges, K. Herkenhoff, R. O. Kuzmin, M. Malin, and W. Ward (1999), Aeolian features and processes at the Mars Pathfinder landing site, *J. of Geophys. Res.*, 104, 8473 – 8584.

Greeley, R., R. O. Kuzmin, S. C. R. Rafkin, T. I. Michaels, and R. Haberle (2003), Wind-related features in Gusev crater, Mars, *J. of Geophys. Res.*, Vol. 108(E12), 8077, doi:10.1029/2002JE002006.

Greeley, R. and A. Skypeck (1993), Martian Aeolian Features and Deposits: Comparisons with General Circulation Model Results, *J. of Geophys. Res.*, Vol. 98(E2), 3183 – 3196.

Greeley, R., R. Leach, B. White, J. Iversen, and J. Pollack (1980), Threshold wind speeds for sand on Mars: Wind tunnel simulations, *Geophys. Res. Lett.*, Vol. 7, 121 – 124.

Greeley, R., P. L. Whelley, R. E. Arvidson, N. A. Cabrol, D. J. Foley, B. J. Franklin, P. G. Geissler, M. P. Golombek, R. O. Kuzmin, G. A. Landis, M. T. Lemmon, L. D. V. Neakrase, S. W. Squyres, and S. D. Thompson (2006b), Active dust devils in Gusev crater, Mars: Observations from the Mars Exploration Rover Spirit, *J. of Geophys. Res.*, Vol. 111(E12S09), doi:10.1029/2006JE002743.

Greeley, R., P. L., Whelley, L. D. V. Neakrase, R. E. Arvidson, N. T. Bridges, N. A. Cabrol, P. R. Christensen, K. Di, D. J. Foley, M. P. Golombek, K.

Herkenhoff, A. Knudson, R. O. Kuzmin, R. Li, T. Michaels, S. W. Squyres, R. Sullivan, and S. D. Thompson (2008), Columbia Hills, Mars: Aeolian features seen from the ground and Orbit, *J. of Geophys. Res.*, Vol. 113(E06S06), doi:10.1029/2007JE002971.

Haberle, R. M., J. B. Pollack, J. R. Barnes, R. W. Zurek, C. B. Leovy, J. R. Murphy, H. Lee, and J. Schaeffer (1993), Mars atmospheric dynamics as simulated by the NASA-Ames general circulation model, *J. of Geophys. Res.*, Vol. 98, 3093 – 3123.

Iversen, J. D. and R. Greeley (1978), Atmospheric and Wind Tunnel Experiments of the Amboy Crater Sand-Covered Lava Flow, *Engineering Research Institute*, Iowa State University, Report 78235.

Iversen, J. D., R. Greeley, B. R. White, and J. B. Pollack (1976), The Effect of Vertical Distortion in the Modeling of Sedimentation Phenomena: Martian Crater Wake Streaks, *J. of Geophys. Res.*, Vol. 81(26), 4846 – 4586.

Iversen, J. D. and B. R. White (1982), Saltation threshold on Earth, Mars and Venus, *Sedimentology* 29, 111 –119.

Kienenberger, R. L. and R. Greeley (2011), Distribution of Windblown Sediment in Small Craters on Mars: Field Analog Studies at Amboy Crater, California. *Lunar and Planet. Sci. XLII*, Abstract 1053.

Kienenberger, R. L. and R. Greeley (2011), Distribution of Windblown Sediment in Small Craters on Mars: Field Analog Studies at Amboy Crater, California. *Planet. Space Sci.*, Manuscript accepted for publication.

Kim, J. R. and J. P. Muller (2009), Multi-resolution topographic data extraction from Martian stereo imagery, *Plan. Space Sci.*, 57, 2095 – 2112, doi:10.1016/j.pss.2009.09.024.

Kirk, R. L., E., Howington-Kraus, M. R. Rosiek, J. A. Anderson, B. A. Archinal, K. J. Becker, D. A. Cook, D. M. Galuszka, P. E. Geissler, T. M. Hare, I. M. Holmberg, L. P. Keszthelyi, B. L. Redding, W. A. Delamere, D. Gallagher, J. D. Chapel, E. M. Eliason, R. King, and A. S. McEwen (2008), Ultrahigh resolution topographic mapping of Mars with MRO HiRISE stereo images: Meter-scale slopes of candidate Phoenix landing sites, *J. of Geophys. Res.*, Vol. 113(E00A24), doi:10.1029/2007JE003000.

Kunter, M. H, C. J. Nachtsheim, J. Neter, and W. Li (2005), *Applied Linear Statistical Models, 5th Edition,* McGraw-Hill, New York, New York. 83 – 87.

Kuzmin, R. O., R. Greeley, S. R. Rafkin, and R. M. Haberle (2001), Wind related modification of small impact craters on Mars, *Icarus* 161, 66 – 89.

Malin, M. C., M. H. Carr, G. E. Danielson, M. E. Davies, W. K. Hartmann, A. P. Ingersoll, P. B. James, H. Masursky, A. S. McEwen, L. A. Soderblom, P. Thomas, J. Veverka, M. A. Caplinger, M. A. Ravine, T. A. Soulanille, and J. L. Warren (1998), Early Views of the Martian Surface from the Mars Orbiter Camera of Mars Global Surveyor, *Science* 279, 1681.

McCauley, J. F. (1973), Mariner 9 Evidence for Wind Erosion in the Equatorial and Mid-Latitude Regions of Mars, *J. of Geophys. Res.*, Vol. 78(20), 4123 – 4137.

McCauley, J. F., C. S. Breed, F. EI-Baz, M. I. Whitney, M. J. Grolier, and A. W. Ward (1979), Pitted and fluted rocks in the western desert of Egypt: Viking comparisons, *J. of Geophys. Res.*, Vol. 84, 8222 – 8232.

McEwen, A. S., E. M. Eliason, J. W. Bergstrom, N. T. Bridges, C. J. Hansen, W. A. Delamere, J. A. Grant, V. C. Gulick, K. E. Herkenhoff, L. Keszthelyi, R. L. Kirk, M. T. Mellon, S. W. Squyres, N. Thomas, and C. M. Weitz (2007), Mars Reconnaissance Orbiter's High Resolution Imaging Science Experiment (HiRISE), *J. of Geophys. Res.*, Vol. 112(E05S02), doi:10.102 9/2005JE002605.

McEwen, A. S., B. S. Preblich, E. P. Turtle, N. A. Artemieva, M. P. Golombek, M. Hurst, R. L. Kirk, D. M. Burr, and P. R. Christensen (2005), The rayed crater Zunil and interpretations of small impact craters on Mars, *Icarus* 176, 351 – 381, doi:10.1016/j.icarus.2005.02.009.

Melosh, H. J. (1989), *Impact Cratering,* Oxford Univ. Press, New York City, New York.

Murray, J. B. and J. E. Guest (1970), Circularities of Craters and Related Structures on Earth and Moon, *Modern Geology*, Vol. 1, 149 – 159.

Murchie, S. R. Arvidson, P. Bedini, K. Beisser, J.-P. Bibring, J. Bishop, J. Boldt, P. Cavender, T. Choo, R. T. Clancy, E. H. Darlington, D. Des Marais, R. Espiritu, D. Fort, R. Green, E. Guinness, J. Hayes, C. Hash, K. Heffernan, J. Hemmler, G. Heyler, D. Humm, J. Hutcheson, N. Izenberg, R. Lee, J. Lees, D. Lohr, E. Malaret, T. Martin, J. A. McGovern, P. McGuire, R. Morris, J. Mustard, S. Pelkey, E. Rhodes, M. Robinson, T. Roush, E. Schaefer, G. Seagrave, F. Seelos, P. Silverglate, S. Slavney, M. Smith, W.-J. Shyong, K. Strohbehn, H. Taylor, P. Thompson, B. Tossman, M. Wirzburger, and M. Wolff (2007), Compact Reconnaissance Imaging

Spectrometer for Mars (CRISM) on Mars Reconnaissance Orbiter (MRO), *J. Geophys. Res.*, Vol. 112, doi:10.1029/2006JE002682.

Mutch, T. A., A. B. Binder, F. O. Huck, E. C. Levinthai, S. Liebes, Jr., E. C. Morris, W. R. Patterson, J. B. Pollack, C. Sagan, and G. R. Taylor (1976), The surface of Mars: The view from the Viking 1 lander, *Science*, 193, 791 – 801.

Oberbeck, V. R., M. Aoyagi, and J. B. Murray (1972), Circularity of Martian Craters, *Modern Geology*, Vol. 3, 195 – 199.

Parker, R. B. (1963), Recent volcanism at Amboy Crater, San Bernardino County, California, *Calif. Div. Min. Geol. Spec. Rept*. 76, 23.

Parsons, R. A. and F. Nimmo (2009), North-south asymmetry in Martian crater slopes, *J. of Geophys. Res.*, Vol. 114(E02002), doi:10.1029/2007JE00 3006.

Pike, R. J. (1980), Control of crater morphology by gravity and target type: Mars, Earth, Moon, *Lunar and Planet. Sci. XI*, 2159 – 2189.

Pollack, J. B. D., R. M. Haberle, J. Schaeffer, and H. Lee (1990), Simulations of the general circulation of the Martian atmosphere, *J. of Geophys. Res.*, Vol. 95, 1447 – 1474.

Rafkin, S. C. R., R. M. Haberle, and T. I. Michaels (2001), The Mars Regional Atmospheric Modeling System: Model description and selected simulations, *Icarus* 151, 228 – 256.

Reynolds, O. (1883), An experimental investigation of the circumstances which determine whether the motion of water shall be direct or sinuous, and of the law of resistance in parallel channels, *Phil. Trans. R. Soc. Lond*, 174, 935 – 982.

Ronca, L. B. and J. W. Salisbury (1966), Lunar History as Suggested by the Circularity Index of Lunar Craters, *Icarus* 5, 130-138.

Rudas, T. (2008), *Handbook of Probability: Theory and Applications*, Sage Publications, Inc., Thousand Oaks, CA, 155.

Ryan, J. A., R. M. Henry, S. L. Hess, C. B. Leovy, J. E. Tillman, and C. Walcek (1978), Mars Meteorology: Three Seasons at the Surface, *Geophys. Res. Lett.*, 5, 715.

Ryan, J. A. and R. D. Lucich (1983), Possible dust devils, vortices on Mars, *J. of Geophys. Res.*, Vol. 88, 11005 – 11011.

Sagan, C., J. Veverka, P. Fox, and R. Dubisch (1972), Variable Features on Mars: Preliminary Mariner 9 Television Results, *Icarus* 17, 346 – 372.

Schetz, J. A. and A. E. Fuhs (1999), *Fundamentals of Fluid Mechanics*, John Wiley & Sons, New York, New York.

Schultz, M. H. (1973), *Spline Analysis*, Prentice-Hall, Inc., Englewood Cliffs, New Jersey.

Squyres, S. W., R. E. Arvidson, J. F. Bell III, J. Brückner, N. A. Cabrol, W. Calvin, M. H. Carr, P. R. Christensen, B. C. Clark, L. Crumpler, D. J. Des Marais, C. d'Uston, T. Economou, J. Farmer, W. Farrand, W. Folkner, M. Golombek, S. Gorevan, J. A. Grant, R. Greeley, J. Grotzinger, L. Haskin, K. E. Herkenhoff, S. Hviid, J. Johnson, G. Klingelhöfer, A. Knoll, G. Landis, M. Lemmon, R. Li, M. B. Madsen, M. C. Malin, S. M. McLennan, H. Y. McSween, D. W. Ming, J. Moersch, R. V. Morris, T. Parker, J. W. Rice Jr., L. Richter, R. Rieder, M. Sims, M. Smith, P. Smith, L. A. Soderblom, R. Sullivan, H. Wänke, T. Wdowiak, M. Wolff, and A. Yen (2004), The Spirit Rover's Athena Science Investigation at Gusev Crater, Mars, *Science*, Vol. 305(5685), 794 – 799, doi:10.1126/science.3050794.

Steel, R. G. D. and J. H. Torrie (1960), *Principles and Procedures of Statistics*, McGraw-Hill, New York.

Sullivan, R., R. Arvidson, J. F. Bell III, R. Gellert, M. Golombek, K. Herkenhoff, J. Johnson, S. Thompson, P. Whelley, and J. Wray (2008), Wind-driven particle mobility on Mars: insights from Mars Exploration Rover observations at "El Dorado" and surroundings at Gusev Crater, *J. Geophys. Res.*, Vol. 113(E06S07), doi:10.1029/2008JE003101.

Thomas, P. and J. Veverka (1979), Seasonal and secular variation of wind streaks on Mars: An analysis of Mariner 9 and Viking data, *J. of Geophys. Res.*, Vol. 84(B14), 8131 – 8146, doi:10.1029/JB084iB14p08131.

Thomas, P., J. Veverka, S. Lee, and A. Bloom (1981), Classification of Wind Streaks on Mars, *Icarus* 45, 124-153.

Tsoar, H., R. Greeley, and A. R. Peterfreund (1979), MARS: The North Polar Sand Sea and Related Wind Patterns, *J. of Geophys. Res.*, Vol. 84(B14), 8167 – 8180, doi:10.1029/JB084iB14p08167.

White, B. R. (1981), Low-Reynolds-Number Turbulent Boundary Layers, *J. Fluid Engng*, Trans. ASME, 103, 624 – 630.

APPENDIX A

ASOS USER'S GUIDE

This appendix includes Chapter 3 of the National Weather Service Automated Surface Observing System (ASOS) User's Guide which provides definitions and algorithms for the weather parameters collected at Barstow, California.

CHAPTER THREE

3.0 Automating the Objective Weather Elements

The "objective" weather elements are defined as ambient and dew point temperature, wind, pressure, and precipitation accumulation. These elements are classified as "objective" because they are more simply and directly measured and are easier to automate than other elements. This chapter describes how ASOS reports objective elements.

3.1 Ambient and Dew Point Temperature

Ambient and dew point temperature reports are among the most widely disseminated of all the weather elements in the surface observation. Because of keen public interest, nearly all radio and most television stations report temperature and humidity at least once an hour. Ambient and dew point temperature are vital in determining aircraft performance and loading characteristics and are critical for accurate weather forecasts. To meet these needs, ASOS provides a 5-minute average ambient air and dew point temperature every minute.

3.1.1 Ambient/Dew Point Temperature Sensor

Both the manual and automated temperature sensors directly measure the ambient dry-bulb and the dew point temperatures. The hygrothermometer used in the ASOS is a modern version of the fully automated "HO-83" hygrothermometer, first used operationally in 1985. This instrument uses a platinum wire Resistive Temperature Device (RTD) to measure ambient temperature and a chilled mirror to determine dew point temperature.

The RTD operates on the principle that electric resistance in a wire varies with temperature. This RTD is located in the stream of aspirated air entering the sensing unit and assumes the ambient air temperature.

To determine dew point temperature, a mirror is cooled by a thermoelectric or Peltier cooler until dew or frost begins to condense on the mirror surface. The body of the mirror contains a platinum wire RTD, similar to that used for ambient temperature. This RTD assumes the mirror's temperature, which is held at the dew point temperature.

Figure 5. ASOS Hygrothermometer

When this condition occurs, the mirror's surface is in vapor pressure equilibrium with the surrounding air (i.e., has reached the saturation vapor pressure). The temperature required to maintain this equilibrium is, by definition, the dew point temperature.

Optical techniques are used to detect the presence of surface condensation. Within the hygrothermometer, a beam of light from a small Light Emitting Diode (LED) is directed at the surface of the mirror at a 45 degree angle. Two photo-resistors are mounted to receive the reflected light. The "direct" sensor is placed at the reflection angle and receives a high degree of light when the mirror is clear. The indirect sensor is placed to receive light scattered when the mirror is clouded with visible condensation, (i.e., dew or frost formation).

In normal operation, a feedback loop controls an electric heat pump running through a cooling-heating cycle, which cools the mirror until dew or frost is formed; it then heats the mirror until the condensate (dew or frost) is evaporated or sublimed. This cycle nominally takes about 1 minute to complete.

As the mirror's cloudiness increases, the "direct" sensor receives less light and the "indirect" sensor receives more light. When the ratio of indirect to direct light reaches an adaptive criterion value, the mirror is considered to be at the dew point temperature. The adaptive criterion value (ratio of indirect to direct light) is adjusted once a day to compensate for residual contamination on the mirror due to dust and other airborne particulates.

Table 1. Temperature Sensor—Range, Accuracy Resolution

Parameter	Range	RMSE	Max Error	Resolution
Ambient	**-80°F to -58°F**	**1.8°F**	**± 3.6°F**	**0.1°F**
Temperature	-58°F to +122°F	0.9°F	± 1.8°F	
	+122°F to +130°F	1.8°F	± 3.6°F	
Dew Point	-80°F to -0.4°F	3.1°F to 7.9°F	4.5°F to 13.9°F	0.1°F
Temperature	-0.4°F to +32°F	2.0°F to 7.9°F	3.4°F to 13.9°F	
	+32°F to +86°F	1.1°F to 4.7°F	2.0°F to 7.9°F	

Since a clean mirror needs relatively less indirect light to determine when dew has formed than a dirty mirror, the mirror is heated once a day to recalibrate the reference reflection expected from a dry mirror. This procedure compensates for a possible dirty or contaminated mirror and redefines adaptive criterion value used to determine when dew or frost has occurred. This once per day recalibration nominally takes about 15 minutes.

The ASOS hygrothermometer meets all NWS specifications for measuring range, accuracy, and resolution. The specifications for accuracy are given in Root Mean Square Error (RMSE) and Maximum (MAX) Error. Specifications are listed in Table 1.

The RMSE for Dew Point Temperature is given as a range of values and is dependent on the Ambient Temperature minus the Dew Point Temperature value (i.e., Dew Point Depression [DD]). The low end of the RMSE and MAX Error range is for a DD of 0°F; the high end of the Error range is for a DD of 63°F.

3.1.2 Ambient Temperature/Dew Point Temperature Algorithm

Both ambient temperature and dew point temperature are considered conservative elements (i.e., continuous in space, and slowly and smoothly changing in time). Based on this characteristic, time-averaging over a short period is the preferred method of measurement.

The ASOS hygrothermometer continually measures the ambient temperature and dew point temperature and provides sample values approximately six times per minute. Processing algorithms in the hygrothermometer use these samples to determine a 1-minute average temperature and dew point valid for a 60-second period ending at M+00. These data are passed to the ACU for further processing.

Once each minute the ACU calculates the 5-minute average ambient temperature and dew point temperature from the 1-minute average observations (provided at least 4 valid 1-minute averages are available). These 5-minute averages are rounded to the nearest degree Fahrenheit, converted to the nearest 0.1 degree Celsius, and reported once each minute as the 5-minute average ambient and dew point temperatures. All mid-point temperature values are rounded *up* (e.g., +3.5°F rounds up to +4.0°F; -3.5°F rounds up to -3.0°F; while -3.6 °F rounds to -4.0 °F).

The ACU performs all temperature averaging functions. It also performs a number of data quality tests on the ambient and dew point temperatures, including upper and lower limit checks, a rate of change check, and a cross comparison. The current 1-minute ambient and dew point temperature are compared against these limits. The upper and lower limits are +130°F to -80°F for ambient temperature and +86°F to -80°F for dew point temperature.

If the current 1-minute ambient or dew point temperature differs from the last respective, non-missing, 1-minute reading in the previous 2 minutes by more than 10°F, it is marked as "missing." The current 1-minute ambient temperature is also compared against the current 1-minute dew point temperature to ensure the dew point is not higher. If the dew point temperature exceeds the ambient temperature by 2°F or less, the dew point temperature is set equal to the ambient temperature. If the dew point temperature exceeds the ambient temperature by more than 2°F, the 1-minute dew point temperature is set to "missing."

If, within the past 5 minutes, there are at least four valid (i.e., non-missing) 1-minute ambient and dew point temperatures, the respective 5-minute averages are computed and reported in degrees Celsius in the OMO and METAR. If there are less than four valid 1-minute average ambient or dew point temperatures within the past 5 minutes, ASOS does not compute the current 5-minute average for ambient or dew point temperature. When this occurs, ASOS uses the most recent 5-minute average value calculated within the past 15 minutes.

If the ASOS has not recorded a valid 5-minute average ambient or dew point temperature within the past 15-minutes, no ambient or dew point temperature is reported and the sensor failure notation is entered into the ASOS system maintenance log (SYSLOG). This 15-minute "hold-off" allows the daily 15-minute calibration heat cycle to occur without adverse affect. The current 1-minute average ambient temperature and the 5-minute average ambient temperature are updated once each minute and stored in memory for 12 hours. These stored data are used in further computation:

- Once each minute, ASOS uses the running 5-minute average ambient temperature to update the hourly maximum and minimum ambient temperatures. At the end of the hour (H+59), the cumulative maximum and minimum ambient temperatures for the hour and the minute(s) they occurred are stored in memory for 24 hours.

- At synoptic hour (00, 06, 12, and 18 UTC) reporting times, the current 6-hour maximum and minimum ambient temperatures are computed from the hourly maximum and minimum ambient temperatures in tenths of degrees Celsius, and included as remarks ("$1s_nT_xT_xT_x$" for maximum temperature, and "$2s_nT_nT_nT_n$"for minimum temperature) in the current synoptic hourly METAR.

- The current 12-hour average ambient temperature is also computed once each minute from the current and previous 12-hour reported 5-minute average temperature (this value is used for calculating current sea-level pressure).

- Once each hour (at the hourly METAR report time) the current hourly ambient temperature and dew point temperature are reported in the METAR Remarks section, to the nearest tenth of a degree Celsius, in the form "$Ts_nT'T'T's_nT'_dT'_dT'_d$"

- Once each minute, ASOS computes the highest and lowest ambient temperatures, so far for the current calendar day, in tenths of degrees Celsius. The calendar day maximum and minimum ambient temperatures are reported in the midnight, LST hourly METAR remarks ($4s_nT_xT_xT_xs_nT_nT_nT_n$), and are stored in memory for 31 days as part of the Daily Summary Product. The "midnight, LST hourly METAR" is usually transmitted before 23:59 LST. Therefore, there may occasionally be a discrepancy between the maximum and minimum temperatures reported in the "4" group and the daily maximum and minimum temperatures reported in the ASOS Daily Summary Message (DSM) which runs from 00:00 to 23:59 LST (see Section 5.6 for details).

- Once each day (at 23:59 LST), the highest and lowest ambient temperatures for the current month, along with the date(s) of occurrence, are computed and stored in memory until the end of the following month. On the first day of the following month, ASOS outputs the Monthly Maximum Temperature and date(s) of occurrence, plus the Monthly Minimum Temperature and date(s) of occurrence[7].

Additional temperature parameters are derived from the Calendar Day and Monthly Maximum and Minimum Temperature data. These data may be reported in the daily and/or monthly summary messages, as appropriate.

The daily data include: calendar day average ambient temperature, the latest daytime maximum temperature (LDT), the latest nighttime minimum temperature (LNT), departure of calendar day average ambient temperature from normal, and heating degree days (HDD) or cooling degree days (CDD).

The monthly data include: average monthly temperature, average monthly maximum and minimum temperature, number of days maximum temperature exceeded a set maximum temperature threshold (90°F in the 48 contiguous United States and Hawaii, and 70°F in Alaska), number of days maximum temperature $\leq$ 32°F, number of days minimum temperature $\leq$ 32°F, number of days minimum temperature $\leq$ 0°F, monthly heating degree days, and monthly cooling degree days.

Relative humidity is calculated using the 5-minute average ambient (dry-bulb) temperature and dew point temperature. The 5-minute average temperature is also used to process other algorithms, specifically sky condition (obscuration determination), present weather (freezing rain determination, and snow - rain discrimination), obscurations (freezing fog, fog, mist, haze discrimination), and pressure (sea-level pressure, pressure altitude, and density altitude calculation).

3.1.3 Ambient Temperature/ Dew Point Temperature Strengths and Limitations

Although the methodology of determining the ambient temperature and dew point temperature is not new, substantial improvements have been achieved by ASOS in measuring temperature and dew point by increasing the

[7]These data are contained in the Monthly Summary message issued by ASOS.

sensor aspiration and siting the sensors away from buildings and heat islands. Furthermore, ASOS's continuous monitoring, self-diagnostics, and application of quality control algorithms ensure that any ambient temperature/ dew point temperature degradation trend is reported before sensor performance falls below performance standards.

At times, however, the reported dew point temperature may become stuck at around zero degrees Celsius. At other times, it may not be representative because of excessive mirror contamination due to dust or other atmospheric aerosols. An aggressive preventative maintenance program is conducted that includes periodic cleaning of the mirror surface. Furthermore, a planned product improvement effort is underway to find a more reliable alternative for measuring Dew Point temperature (see Section 7.2.2 for details).

3.2 Wind

The rotating cup anemometer and the simple wind vane are the principal indicators of wind speed and direction. Until the mid 1940s, the electrical contacting anemometer was the standard wind measuring instrument. Since then, the "F420" series of instruments have become the standard for wind measurement in the U.S. A basic system of this series consists of a cup-driven Direct Current (DC) generator with an output calibrated in knots and a vane coupled to an indicator by means of a DC synchro-system. The ASOS uses a modern automated version of the F420, in which electro-magnetic signals generated by the rotating cup and wind vane are directly converted into reportable values by ASOS.

Before ASOS, airport wind sensors were generally exposed 20 feet above ground level. With modern, high-performance aircraft, this standard no longer applies. Now, current federal standards for siting meteorological equipment specify (with some variance permitted) a height of 10 meters (32.8 feet). Typical ASOS wind sensor heights are 33 feet or 27 feet, depending on local site-specific restrictions or requirements. Figure 6 shows the ASOS anemometer. The ASOS will report the following wind related parameters.

Wind Direction: ASOS reports a 2-minute average of 5-second average wind directions once a minute (i.e., 24 samples each minute) for distribution through the OMO and computer-generated voice messages. The current 2-minute average wind direction is updated on selected OID screen displays once every minute and included in the transmitted METAR/SPECI messages. The direction from which the wind is blowing is reported to the nearest 10 degree increment (e.g., 274 degrees is reported as 270 degrees). Wind direction is reported relative to *true north* in the METAR/SPECI message, in the daily/monthly summaries, and on all video displays. Wind direction is reported relative to *magnetic north* in the computer-generated voice messages, and on the OID "AUX" data display screen. See section 3.2.2.1 for details.

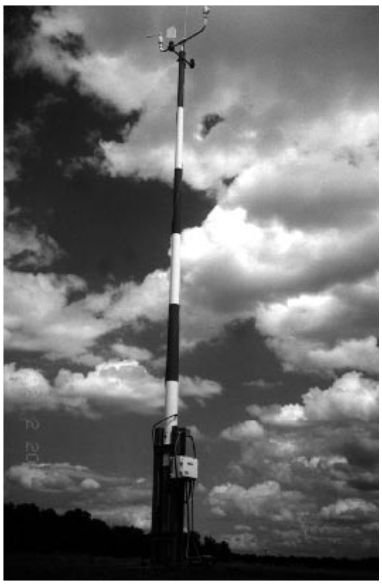

Figure 6. ASOS Anemometer

Wind Speed: A 2-minute average is updated once every 5 seconds and is reported once every minute in the OMO and computer-generated voice messages, and included in the METAR/SPECI message and various OID screen displays. See Section 3.2.2.1 for details.

Wind Gust: This is a basic component of wind character and is updated every 5 seconds. It is appended to and reported with the basic wind observation only when appropriate conditions for reporting wind gust exist (see definition in Section 3.2.2.2). Wind gust information is included in the current OMO, computer-generated voice messages, the METAR/SPECI, and OID displays.

Wind Shift: This remark is reported in the OMO and the METAR/SPECI when appropriate. See Section 3.2.2.2a for details.

Variable Wind Direction: This data element is reported in the OMO and the METAR/SPECI when appropriate. See Section 3.2.2.2b for details.

Table 2. Wind Sensor—Range, Accuracy, Resolution

Parameter	Range	Accuracy	Resolution
Wind Speed	0 to 125 knots	± 2 knots - or - 5% (whichever is greater)	1 knot
Wind Direction	0 to 359 degrees	± 5 degrees when wind speed is ≥ 5 knots	nearest degree

Squall: Although squall is a basic component of wind character and, under appropriate conditions is updated every 5 seconds, it is reported in the *present weather* section of the METAR/SPECI observation; direction and speed values are indicated in the wind group. See Section 3.2.2.2c for details.

Peak Wind: This remark is reported in the scheduled hourly METAR, as appropriate. It is the greatest 5-second average wind exceeding 25 knots which has been observed since the previously scheduled hourly METAR.

Daily Peak Wind: This value is reported in the Daily Summary message (see Section 5.6.1). It is the greatest 5-second average wind speed observed (converted to miles per hour) during the 24-hour calendar day beginning at 5-seconds past midnight, Local Standard Time (LST), (00:00:05 LST) and ending at midnight (00:00:00 LST) the next day.

Fastest 2-Minute Wind: This value is reported in the Daily Summary message. It is the fastest 2-minute average wind speed (in miles per hour) observed over the 24-hour calendar day.

3.2.1 Wind Sensor

The ASOS wind sensor (Figure 6) employs a "light chopper," electro-optical method to determine wind speed and convert it to appropriate electro-magnetic signals. Wind sensor measurements conform to the Range, Accuracy, Resolution specifications described in Table 2. In addition, the sensor's starting threshold for response to wind direction and wind speed is 2 knots. Winds measured at 2-knots or less are reported as calm.

3.2.2 Wind Algorithm

The basic method of observing wind direction and speed is to take a fixed point, time averaged measurement. The ASOS algorithm uses a 2-minute period to obtain the current average wind direction and speed. In both cases, ASOS obtains the wind character (i.e., gusts and present weather squalls) and the peak wind by comparing the difference between the average wind speed with the maximum "instantaneous" wind speed observed over a specified time interval. When this difference exceeds a prescribed value, the appropriate additional wind information is included in the observation. The ASOS wind shift remark is determined from the difference between the current 10-minute average (of 2-minute average winds) and the 10-minute average (of 2-minute average winds) from 15 minutes ago, provided the intervening 2-minute average wind speeds are greater than 9 knots. Within ASOS, all average wind directions and speeds are rounded up to the nearest degree and knot, respectively.

3.2.2.1 Wind Direction and Speed

In the past, observers monitored an analog or digital wind dial over a short period to determine the average wind direction and speed for the observation. Most sites also had a wind recorder device to provide a continuous documented record of measured wind direction and speed. The observer often used this device to determine the maximum instantaneous wind speed over the 10-minute period before completing the observation. The observer used visual/mental averaging and ultimate human judgement to create an observation of wind. This method was not always consistent from site to site or from one observer to another.

ASOS continuously and objectively measures wind direction and speed once every second, far more frequently, consistently, and accurately than an observer could. Every

ASOS processes data identically, which provides site-to-site consistency unknown in past records. Five-second wind direction and wind speed averages are computed from the 1-second measurements. These 5-second averages are rounded to the nearest degree and nearest knot and are retained for 2 minutes. These five-second averages are the fundamental units used to compute reportable wind values and are, in effect, the ASOS equivalent to the manual "instantaneous" wind observation.

Every 5 seconds a running 2-minute average wind (direction and speed) is computed and used to further compute wind character. If the computed 2-minute average wind speed is 2 knots or less, the 2-minute average wind direction and speed is reported as "calm" (00000KT).

Once each minute the current 2-minute average wind is stored in memory for 12 hours and made available for reporting in the OMO, the computer generated voice messages (i.e., the ground-to-air radio and telephone dial-in message), the METAR/SPECI reports, and OID displays.

3.2.2.2 Wind Character

Wind Character information is added to the METAR after the Wind Direction and Speed data when the variability in the steady state wind exceeds threshold criteria. Wind Character components include Wind Gusts and Variable Wind. Although Wind Squalls are reported as a Present Weather phenomena in METAR, they are also discussed here for comparison and contrast.

Both the manual procedure and the ASOS algorithm determine Wind Character by examining the maximum "instantaneous" wind speed over the 10-minute period immediately preceding the observation. The manual procedure requires a visual examination and interpretation of the dial readings or recorder to determine "instantaneous" wind speed. The ASOS algorithm, by contrast, relies on objective 5-second averages of 1-second wind measurements.

3.2.2.2a Gusts

In the **manual procedure**, a gust is reported when an observer sees rapid fluctuations in sensor wind speed indications with a variation of 10 knots or more between peaks and lulls during the 10-minutes before the observation. The reported gust is taken from the maximum "instantaneous" wind speed observed during this period. The average 2-minute wind is used to report wind direction and wind speed. Conceivably, an average 2-minute wind speed as low as 3 knots (observed in the last minute) may be reported with a gust of 10 knots (observed in the last 10 minutes). Observations of 5 knots with gusts of 10 to 15 knots, however, are the more common minimum values reported.

The **ASOS algorithm** also relies on a 10-minute observation period to determine gusts, but uses it in a different way. Once every 5 seconds, the ASOS computes the greatest 5-second average wind speed (and corresponding direction) during the past minute, and once each minute stores this information in memory for 12 hours.

Once every 5 seconds the ASOS computes the current 2-minute average wind speed and compares it with the greatest 5-second average wind speed during the past minute. If the current 2-minute average wind speed is equal to or greater than 9 knots and the greatest 5-second average wind speed (during the past minute) exceeds the current 2-minute average speed by 5-knots or more, then the greatest 5-second average speed observed during the past minute is stored in memory as a gust for 10 minutes.

Once every 5 seconds, the ASOS compares the highest gust stored in memory for the past 10 minutes with the current 2-minute average wind speed. If the difference between the two is 3 knots or more, the current reported wind speed is greater than 2 knots, and the highest gust exceeds the minimum 5-second wind speed in the past 10 minutes by 10 knots or more, then the highest gust stored in memory is designated as the reportable gust. This value is appended to the current wind direction and speed reported in the OMO, computer-generated voice messages, and the METAR/SPECI reports. The minimum gust speed reported by ASOS is 14 knots. Wind speeds from 3 knots and 11 knots may be reported with gusts to 14 knots. For example, a 2-minute average wind of 240 degrees at 10 knots with gusts to 20 knots is reported as: "24010G20KT."

3.2.2.2b Variable Wind

Both the manual procedure and the ASOS algorithm use the same definition for determining a variable wind but use different methods for reporting it. In both cases, a variable wind is reported when the wind direction varies by 60 degrees or more during the 2-minute evaluation period before the observation. If the 2-minute wind speed is 6 knots or less, than a variable wind direction indicator (VRB) is included in the basic wind group; if the 2-minute wind speed is greater than 6 knots, then a variable wind direction group is appended to the basic wind group in the body of the METAR/SPECI report.

The basis for the manual determination of a variable wind is simply a visual interpretation of the wind instrument reading during the 2-minute evaluation period. The ASOS algorithm by contrast compares the range of 5-sec-

ond average wind directions during the past 2 minutes (24 samples).

In either case, if the current 2-minute average wind speed is 6 knots or less, the wind direction and speed is reported as "VRBff," where "ff" is the current 2-minute average wind speed in knots. For example, a variable wind at 3 knots is encoded as "VRB03."

If the current 2-minute average wind speed is greater than 6 knots, then the current wind direction and speed are placed in the body of the report and followed by a variability indicator in the form "$d_nd_nd_nVd_xd_xd_x$," where $d_nd_nd_n$ is the minimum, and $d_xd_xd_x$ is the maximum variable wind direction during the past 2-minutes. For example, a current 2-minute wind of 270 degrees at 10 knots that varies from 240 degrees to 300 degrees is coded as: 27010 240V300.

3.2.2.2c Squalls

In the **manual procedure**, observers report a squall when wind speed suddenly increases by at least 16 knots and speed is sustained at 22 knots or more for at least 1 minute. Observers manually determine a squall by visually examining the indicated or recorded "instantaneous" wind speed. The reported squall value is taken from the maximum "instantaneous" wind speed sustained for at least 1 minute. Although squalls are measured as a parameter of wind, they are reported as an element in the present weather field of the METAR/SPECI report.

ASOS algorithm by contrast, computes a potential squall value once every 5 seconds. If the current 2-minute wind speed (measured every five seconds) is greater than or equal to 22 knots and exceeds the 2-minute average wind speed computed two minutes ago by 16-knots or more, then the highest 5-second average wind speed during the last 2-minutes is stored in memory as a squall for 10 minutes. Only the current squall or non-squall default value is stored in memory. The stored squall value is reported as "SQ" in the present weather field if the current 2-minute average wind speed is greater than 2 knots, and if the squall value exceeds the current 2-minute average wind speed by more than 3 knots.

According to this algorithm, a squall may continue to be reported by the ASOS for up to 10 minutes after the squall is written to memory, provided the above minimum wind-speed, squall reporting conditions are met. The minimum wind speed - squall combination reported by ASOS is a wind speed of 3 knots, with a squall of 22 knots.

3.2.2.3 Wind Remarks

The ASOS will include Wind Shift and Peak Wind remarks in the METAR/SPECI reports when appropriate.

3.2.2.3a Wind Shift

Both the manual procedure and the ASOS algorithm use the same definition of a wind shift as described in the FMH-1: "A wind shift is indicated by a change in wind direction of 45 degrees or more in less than 15 minutes with sustained winds of 10 knots or more throughout the wind shift."

The observer relies on his alertness and a visual estimate of the 2-minute average wind to determine the onset of a wind shift. A Frontal Passage (FROPA) remark may be appended to the wind shift remark when the wind shift is associated with a frontal passage. This determination of course is based on human judgement.

The ASOS, on the other hand, determines a wind shift by first making sure that minimum wind speed and direction change criteria are met. These checks are made to ensure that light, variable winds are not erroneously reported as a wind shift.

The wind *speed* criterion requires that all 2-minute average wind speeds computed each minute over the past 15 minutes are greater than 9 knots. If this criterion is met, then the current 10-minute average wind *direction* derived from ten one-minute-observations is compared to a similar 10-minute average wind direction from 15 minutes ago. If the wind directions differ by 45 degrees or more, then a wind shift is encoded.

The wind shift remark generated by the ASOS in the METAR report is: "WSHFT hhmm," where "hhmm" is the Universal Coordinated Time (UTC) of when the shift began (15 minutes ago). Once the wind shift remark is reported, it will continue to be included in all subsequent reports (including long-line dissemination of ASOS generated SPECI) through the next scheduled hourly METAR. The ASOS, of course, is unaware of distant phenomena and synoptic scale weather patterns and consequently cannot confidently determine if a frontal passage (FROPA) remark should be appended to the wind shift remark. Therefore, FROPA is not reported by ASOS. At attended sites however, this remark may be added by the Observer in accordance with agency reporting policy.

3.2.2.3b Peak Wind

The Peak Wind, by definition, is the highest instantaneous wind speed observed or recorded since the last scheduled hourly observation (METAR). The Peak Wind direction, speed and time of occurrence are reported in METAR remarks as: "PK WND dddff(f)/(hh)mm," where ddd = direction (true) in tens of degrees, ff(f) = wind speed in knots, and (hh)mm = (hour) minutes past current hour of most recent occurrence of the reported peak wind. The "hh" indicator is included only when the peak wind occurred in the previous hour since the last METAR.

The manual procedure requires a Peak Wind to be reported when the maximum *instantaneous* wind speed since the last METAR exceeds 25 knots.

In ASOS, the Peak Wind is determined from the highest observed 5-second average wind speed which exceeds 25 knots since the last generated METAR, whether transmitted or not (FIBI).

3.2.3 Wind Strengths and Limitations

The major strength of the ASOS in reporting winds is the consistency of measurements. While Observers rely on perception and human judgement to interpret wind instruments, automated systems rely on digital second-by-second measurements that are processed identically from time-to-time and place-to-place.

One limitation in the automated observation is a lag in reporting wind shifts (in METAR remarks). The wind shift algorithm cannot rely on external clues used by the observer (like thunder or snow showers) for early collateral assurance of a wind shift - frontal passage occurrence. It must therefore wait the full 15-minutes required in the definition of wind shift before outputting a remark. Although highly unlikely, a wind shift and variable wind remark may both be generated and included on the same METAR under conditions of light and variable winds which just barely meet the wind shift reporting criteria, or when a FROPA has occurred in the preceding 10-15 minutes. To be more responsive to operational needs, the wind reporting algorithm has been tuned to prevent excessive, frequent reporting of a wind shift once a report is issued and when a variable wind condition exists.

3.3 Pressure

Atmospheric pressure is the most important surface weather element for aircraft operations since it provides the means of establishing the height of an aircraft above the ground. It is the only element that cannot be directly observed or qualitatively sensed by the observer or pilot. As a result, pressure has always been carefully measured and the operational sensor routinely compared to some reference standard.

All the currently computed pressure elements will continue to be reported by the ASOS with the same or higher level of precision as the human report. The pressure parameters available from ASOS are:

- Sensor Pressure
- Altimeter Setting
- Pressure Remarks
- Sea-Level Pressure
- Density Altitude
- Pressure Altitude
- Pressure Change/Tendency
- Station Pressure

Because accurate pressure is critical, three separate and independent pressure sensors are used at towered airport locations. At other locations, two pressure sensors are used. The ASOS algorithm compares the pressure sensors' readings and issues a pressure report only when there is acceptable agreement between at least two sensors.

3.3.1 Pressure Sensor

The ASOS pressure measurement instrument consists of redundant digital pressure transducers, which use capacitive sensors, one side of which is permanently evacuated to a vacuum to make it a barometric pressure sensor. Advanced microcomputer electronics and sophisticated firmware provide reliable performance. The barometers are located on a tray at the bottom of the ACU and are exposed to the ambient air pressure. In cases when the ACU is installed in pressurized buildings, this exposure is through a port connected to an outside static pressure vent. Figure 7 shows the pressure sensors in the ACU. The specified operational characteristics for these sensors are:

- Range: 16.9 - 31.5 inches of mercury
- Accuracy: ± 0.02 inches of mercury
- Resolution: 0.003 inches of mercury (measurement); 0.005 inches of mercury (reporting)

3.3.2 Pressure Algorithm

A sophisticated algorithm routinely computes and updates the pressure report for each pressure sensor once a minute from readings obtained every 10 seconds from each

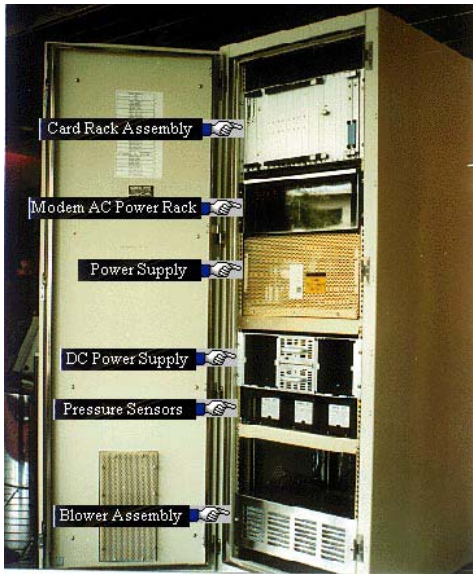

Figure 7. ASOS Pressure Sensor

sensor. If one or more of the 6 pressure readings obtained from each sensor in the past minute is missing, then the 1-minute pressure value for that sensor is marked as "missing" and the sensor is logged as "inoperative." The current 1-minute pressure values from each sensor are then compared against each other and absolute differences computed. The lowest 1-minute sensor pressure value obtained from a pair of sensors, whose pressure difference is 0.04 inch or less, is the designated ASOS pressure to be reported at the end of the minute. This pressure value is then used to compute an altimeter setting and other derived pressure values.

A sensor whose 1-minute sensor value differs by more than 0.04 inch from another operational sensor is automatically logged as "inoperative" and the sensor pressure value set to "missing." This will cause a maintenance check indicator to be appended to all subsequent ASOS METAR/SPECI reports until the sensor is returned to an "operational" status. Once a pressure sensor is logged as inoperative, it can only be returned to an "operational" status by a maintenance technician. If one of the sensors (at two-sensor locations), or if two of the sensors (at three-sensor locations) are logged as "inoperative," then the designated ASOS pressure elements are all omitted in the METAR/SPECI reports.

3.3.3 Pressure Strengths and Limitations

The pressure sensors are the most reliable and accurate sensor in ASOS. The only limitation (if one can call it that) is that pressure remarks will be reported more often in ASOS METAR messages than in manual METAR messages simply because of the continuous weather watch which ASOS provides.

3.4 Precipitation Accumulation

Accurate liquid-equivalent precipitation accumulation measurements are essential for hydrological, flood forecasting, and agriculture applications. For aviation purposes, freezing or frozen precipitation accumulation measurements provide a quantitative dimension to the qualitative detection and reporting of freezing or frozen precipitation by other ASOS sensors.

Basic manual measurements of precipitation accumulation in the U.S. have traditionally relied on the Standard 8-inch Gauge. This consists of an 8-inch cylinder with an inverted funnel orifice leading to a graduated inner cylinder at the base of the funnel neck. The inner cylinder is used to measure liquid precipitation accumulation. When freezing or frozen precipitation is expected or is occurring, the funnel and inner cylinder are removed. Frozen precipitation captured in the outer cylinder are periodically melted indoors to measure the liquid-equivalent of frozen precipitation (LEFP).

In the early development of an automated precipitation accumulation gauge, it was recognized that automated measurement of liquid and LEFP each presented a unique challenge, so, a separate specification was written for each type of precipitation. The automated Heated Tipping Bucket (HTB) technology from the 1970s was adopted and modified to meet these needs. Over the years, many improvements were made and incorporated into ASOS. Early versions of the heated gauge applied excessive heat creating excessive evaporation and the under-reporting of the liquid-equivalent mass.

The current version of the HTB gauge applies less heat over a longer heating cycle, thus yielding a more accurate mass measurement of frozen precipitation. Changes in the tipping bucket inner design also have improved overall performance in liquid precipitation events. These improvements have resulted in the ASOS HTB becoming a very capable liquid precipitation accumulation gauge in all but the most extreme heavy rainfall events. However, some

deficiencies still remain in its ability to fully measure precipitation accumulation during the cold-season LEFP events. Consequently, the ASOS HTB is primarily used to measure liquid accumulation. Alternative solutions are being pursued to provide LEFP information. These solutions include: (1) Provision of separate LEFP reports through existing manual supplementary observing networks from event-driven Supplementary Data Observations and schedule-driven Supplementary Climate Data reports, and (2) Development of a follow-on All-Weather Precipitation Accumulation Gauge for ASOS (see Section 7.2.4).

3.4.1 Heated Tipping Bucket (HTB) Precipitation Gauge

The ASOS HTB shown in Figure 8 consists of 6 main components:

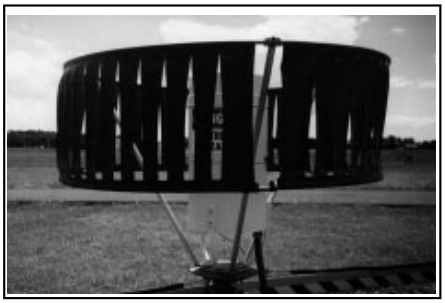

Figure 8. ASOS Heated Tipping Bucket

- A wind shield that surrounds the HTB and protects it against blowing snow from falling into the HTB collector funnel (the wind shield is installed on the ASOS HTB in climates where the snowfall is $\geq$ 20% of the annual precipitation accumulation)
- A 12-inch diameter collector funnel
- A pivoting dual chamber tipping bucket. This bucket tips when one chamber is filled with 0.01 inch of liquid precipitation, thus emptying the contents into a drain pan and exposing the other chamber to the precipitation gathered by the collector funnel
- An electronic switch which counts the number of tips per minute
- A drain pan and a drain tube
- Heating elements to prevent freeze-up during cold weather.

The HTB has 2 heating elements. One heating element is wrapped around the underside of the collector funnel, and the other around the drain tube. Each heater is separately thermostatically controlled to maintain a temperature of 40°F. A master thermostat regulates electric power to both heating elements. Power is turned on when the temperature falls below 40°F and is turned off when the temperature falls below -20°F. Power is not turned on again until the temperature rises above -12°F. Power is turned off when the temperature is at or above 40°F.

The HTB has a precipitation accumulation range of 0 to 10.00 inches per hour, a resolution of 0.01 inch (i.e., one tip) and an accuracy of ± 0.02 inch or 4% of the hourly total (whichever is greater).

3.4.2 Precipitation Accumulation Algorithm

The precipitation accumulation algorithm obtains precipitation accumulation data from the HTB precipitation gauge once each minute. These data are valid for discrete 60-second periods ending at M+00. The ASOS algorithm corrects the tipping bucket measurement, particularly during periods of high rainfall rates. Each minute the measured rainfall is adjusted using the following equation:

$$C = A\,(1 + .60A)$$

In this equation, C = the calculated rainfall amount and A = the measured amount from the tipping bucket. All calculations are performed internally using floating point until rounded for final output each minute.

If a 1-minute precipitation accumulation output is missing and the precipitation identifier sensor (discussed in Section 4.3) is either inoperative or concurrently reports precipitation, then the associated METAR precipitation remarks/messages will either be omitted (Prrrr remark is deleted), or contain a "/ " (e.g., 6////, 7////). Furthermore, when the precipitation accumulation sensor is inoperative, a "PNO" remark will be appended to the METAR to indicate that precipitation accumulation information is not available. In SHEF, missing precipitation accumulation data will be reported as "M" in place of the missing value. When available, the output data are used each minute by the algorithm to compile a variety of cumulative precipitation remarks/messages. These include:

METAR hourly message, "Prrrr" remark: In this message "rrrr" is the liquid equivalent of all precipitation (in hundredths of an inch) which has occurred since computation of the Prrrr remark for the last scheduled hourly

METAR message. The "rrrr" is the sum of all 1-minute precipitation accumulations calculated during this period. If any of the required constituent 1-minute precipitation accumulation calculations are missing, the remark is omitted and "PNO" is appended to the remarks section. If no precipitation has occurred since the last scheduled hourly METAR, the Prrrr remark will not be reported. If only a trace of precipitation has occurred, the Prrrr remark will report "P0000."

METAR 3- and 6-hourly report, "6RRRR" precipitation accumulation remark: "RRRR" is the amount of precipitation, in hundredths of an inch, which has accumulated in the past 3- or 6-hours. Three-hourly amounts are reported in the 03, 09, 15, and 21 UTC METAR reports. Six-hourly amounts are reported in the 00, 06, 12, and 18 UTC METAR reports.

If any of the constituent hourly Prrrr remarks are missing, the 6RRRR remark is encoded as 6////.

METAR 24-Hour "7RRRR" precipitation accumulation remark: "RRRR" in this message is the amount of liquid equivalent in hundredths of an inch accumulated over the last 24-hours. This remark is reported with the 1200 UTC METAR provided there has been at least 0.01 inch of precipitation in the past 24-hours (i.e., since the last 1200 UTC METAR). The precipitation accumulation reported in the 7RRRR remarks is compiled from the hourly precipitation computations. If any hourly amount is missing during the 24-hour period, the 7RRRR remark is encoded as 7////.

SHEF 15-Minute Precipitation Criteria message: These messages are generated when the current 15-minute period accumulation exceeds the locally established precipitation accumulation onset threshold and will cease when the accumulation for the current interval falls below the termination threshold. The precipitation accumulations for the four most recent discrete 15-minute periods (ending at H+00, H+15, H+30 and H+45) are chronologically listed in these messages.

These messages are issued in ".E" SHEF message format, and are initially disseminated through the NWS or the FAA communications networks to the NWS Telecommunications Gateway (NWSTG) and the System Monitoring and Coordination Center (SMCC) where they are made available for redistribution to NWS offices and compilation on the daily Service Records Retention System (SRRS) tape for the National Climatic Data Center (NCDC). These messages are identified within the NWS by their RR6 AFOS/AWIPS header: "CCCRR6XXX," where "CCC" is the originating AFOS node, "RR6" is the designation for SHEF 15-minute messages originating from ASOS and "XXX" is the ASOS location identifier (see Section 5.5.1 for details).

All SHEF data from FAA sites are contained in a "collective" (a group of individual messages bundled together) and are identified by the collective header "NMCRR7NKA." The precipitation accumulation for each 15-minute period is derived from the sum of the 1-minute precipitation accumulation calculations within each discrete 15-minute period. If any of the constituent 1-minute precipitation accumulation calculations are missing, the value encoded in the SHEF 15-minute precipitation criteria message for the entire 15-minute period is "M."

SHEF Hourly Routine Precipitation message: The precipitation accumulation period for this message is 60 minutes. The end time (in minutes past the hour) is set at H+00. These messages are issued once an hour at the time specified to support calibration of the precipitation processing at the designated WSR-88D Radar Product Generator.

These SHEF messages contain an hourly precipitation accumulation. They are issued in ".A" SHEF message format and are made available and distributed in the same manner as the SHEF 15-Minute Precipitation Criteria messages. The messages are identified within the NWS by their RR7 AFOS/AWIPS header: "CCCRR7XXX." All SHEF data from FAA sites are contained in a collective and are identified by the collective header "NMCRR7NKA." These messages are further distinguished from the 15-Minute Precipitation Criteria messages by message type identification within the body of the message (see Section 5.5.2 for further details).

The SHEF Hourly Routine Precipitation accumulation is derived from the sum of the 1-minute precipitation accumulation calculations during the latest discrete 60-minute period. If any of the constituent 1-minute precipitation accumulation calculations are missing, the SHEF Hourly Precipitation message will report the precipitation accumulation as "PPH M" (see Section 5.5.2).

Daily and Monthly cumulative precipitation totals: These precipitation totals are summed each minute and included along with other data in the Daily Summary and Monthly Summary Products/messages.

The information in the Daily Summary is valid for the 24-hour period beginning at 00:00 LST and ending at 23:59 LST. This message is issued on the following calendar day at programmable transmission times (see Section 5.6 for further details).

The Monthly Summary message is valid for the calendar month. This message is issued on the first day of the following month at a time specified by the system manager. The Monthly Summary message contains the amount(s) and date(s) of the maximum 24-hour precipitation accumulation during the calendar month; the number of calendar days with precipitation equal to or greater than 0.01, 0.10, 0.50 and 1.00 inches respectively; and departure of monthly cumulative precipitation totals from normal. Other parameters are also included in the Daily and Monthly Summary messages. See Sections 5.6.1 and 5.6.2 for further details.

3.4.3 Precipitation Accumulation Strengths and Limitations

There are well known problems (referenced in Section 3.4) associated with a HTB precipitation gauge. A major problem occurs during high rainfall rate events when the tipping bucket cannot keep up with the water flow and under-reports the accumulation. The ASOS software corrects for the HTB bias to under report precipitation accumulation during most heavy rainfall events (greater than 1.80 inch per hour); however, during extremely heavy rainfall events (greater than 10 inches per hour), the HTB may still under-report the total rainfall accumulation.

During freezing conditions, the application of heat to melt snow and prevent gauge icing also induces evaporation or sublimation, especially during light freezing rain or snow events at temperatures near 32°F. This results in a tendency to under-report freezing or frozen precipitation accumulation.

The tendency to under-report accumulation during freezing rain or snow events is moderated by using a less intense heat source to melt the frozen precipitation from the tipping bucket at a slower rate. The slower heating rate however, can sometimes allow unmelted snow to bridge over the heated funnel surface and form a snow cap over the orifice opening which prevents any further accretion into the gauge.

At some time after the precipitation event ends, under bright sunshine and/or warming ambient temperature, the snow cap melts and falls into the gauge. This causes a delayed accumulation to be registered and falsely reported at a time when no precipitation is occurring. "False tips" may also be caused by dew, frost, or heavy fog.

APPENDIX B

WIND TUNNEL MODEL PREPARATION

Model Preparation

Recipe for dyed sand
2/3 gallon 120 μm white (silica) sand
4 caps of opaque purple Dykem dye (Part number 81763)

Directions for preparation
Fill a gallon plastic Ziploc bag with 2/3 gallon of sand and place 4 caps of dye into the bag. Close and shake/mix until the dye has been worked into the sand. Repeat steps (will need approximately 3 gallons for an entire floor. Pour all sand into a concrete mixer and let run for 1 hour until thoroughly mixed. Sieve out any large particles or clumps.

Recipe for glue base
120 ml Elmer's wood glue
140 ml water
This recipe should be doubled if preparing glue for the entire wind tunnel floor.

Procedure for sanding the model or floor
Fill a spray gun with the prepared glue and coat the model/floor three times with glue. Then, quickly sand the model/floor with the dyed sand using a sieve until all glue has been thoroughly covered with sand. Allow the model/floor to dry for 1 day. Once the model/floor is dry, tip up or use compressed air to remove loose sand. A small amount of glue pooling is common after the first coating of glue/sand.

Repeat the entire process to even out. You will need to make more glue for this. A total of two coats of glue and sand is usually acceptable.

Procedure for cleaning the model/floor
Soak the model in water for a few minutes. The sand and glue should wash off easily.

APPENDIX C

TABLES

Run #	Model #	Start Date	Type of run	Velocity (m/s)	Duration (hours)
CA-10-001	1	29 April 2010	deposition	4-6	1.0
				6-8	111.0
				8-9	28.5
CA-10-002	1	6 May 2010	erosion	5-7	21.5
				7-9	66.5
CA-10-005	1	15 June 2010	grid	3-9	0.5
CA-10-013	3	8 September 2010	deposition	4-6	306.5
				6-8	211.0
				8-9	49
CA-10-015	4	6 October 2010	deposition	4-5	174.0
CA-10-018	5	19 October 2010	deposition	4-5	332.0
CA-10-020	6	11 November 2010	deposition	4-5	192.0
CA-10-021	6	19 November 2010	deposition	5-6	96.8
CA-10-022	6	23 November 2010	deposition	6-7	143.0
CA-10-023	6	30 November 2010	deposition	7-8	72.0
CA-10-025	2	17 December 2010	deposition	4-5	264.0

Table 5: *Summary of wind tunnel simulations*

Crater	Depth (m)	Circle Diameter (m)	Measured Diameter (m)	Rim Height (m)	d/D Ratio (Circle)	d/D Ratio (Measured)	r/D Ratio (Circle)	r/D Ratio (Measured)	Circularity
C_1655_0001	5.80	114.43	117.47	2.55	0.051	0.049	0.022	0.022	1.060
C_1655_0002	5.00	95.19	92.15	2.36	0.053	0.054	0.025	0.026	1.049
C_1655_0003	7.80	125.56	124.44	2.18	0.062	0.063	0.017	0.018	1.035
C_1655_0004	8.80	129.14	132.57	3.94	0.068	0.066	0.031	0.030	1.030
C_1655_0005	5.30	80.00	78.05	2.30	0.066	0.068	0.029	0.029	1.041
C_1655_0006	9.80	142.35	142.35	3.47	0.069	0.069	0.024	0.024	1.030
C_1655_0007	12.90	181.18	180.00	5.71	0.071	0.072	0.032	0.032	1.050
C_1655_0009	6.30	114.94	117.24	2.86	0.055	0.054	0.025	0.024	1.048
C_1655_0010	3.85	108.42	105.26	1.44	0.036	0.037	0.013	0.014	1.046
C_1655_0011	6.18	132.63	132.63	2.42	0.047	0.047	0.018	0.018	1.038
C_1655_0012	6.00	102.11	101.05	2.06	0.059	0.059	0.020	0.020	1.050
C_1655_0013	8.50	142.35	141.18	3.35	0.060	0.060	0.024	0.024	1.049
C_1655_0014	6.90	117.65	117.65	2.54	0.059	0.059	0.022	0.022	1.052
C_1655_0015	4.30	92.63	90.53	2.20	0.046	0.047	0.024	0.024	1.063
C_1655_0016	5.20	86.32	88.42	1.81	0.060	0.059	0.021	0.020	1.080
C_1655_0017	6.10	83.04	81.01	2.73	0.073	0.075	0.033	0.034	1.052
C_1655_0018	5.60	83.04	83.04	2.21	0.067	0.067	0.027	0.027	1.037
C_1655_0019	5.00	65.82	65.82	1.97	0.076	0.076	0.030	0.030	1.027
C_1655_0020	4.45	65.82	68.86	1.19	0.068	0.065	0.018	0.017	1.048
C_1655_0021	3.50	56.52	59.13	1.74	0.062	0.059	0.031	0.029	1.042
C_1655_0022	3.90	64.37	64.37	1.25	0.061	0.061	0.019	0.019	1.050
C_1655_0023	7.40	125.56	122.22	4.39	0.059	0.061	0.035	0.036	1.023
C_1655_0024	3.80	80.92	77.24	1.45	0.047	0.049	0.018	0.019	1.066
C_1655_0025	4.50	69.89	70.80	2.06	0.064	0.064	0.029	0.029	1.058
C_1655_0026	3.10	55.17	54.25	1.40	0.056	0.057	0.025	0.026	1.030
C_1655_0027	3.20	55.17	53.33	1.18	0.058	0.060	0.021	0.022	1.042
C_1655_0028	6.70	97.47	96.55	2.65	0.069	0.069	0.027	0.027	1.041
C_1655_0029	6.80	125.56	126.67	3.07	0.054	0.054	0.024	0.024	1.082
C_1655_0030	4.80	75.40	76.32	1.56	0.064	0.063	0.021	0.020	1.063
C_1655_0031	3.90	51.49	53.33	1.32	0.076	0.073	0.026	0.025	1.058
C_1655_0032	4.10	91.95	90.11	1.83	0.045	0.045	0.020	0.020	1.050
C_1655_0033	11.10	163.53	162.35	5.36	0.068	0.068	0.033	0.033	1.034
C_1655_0034	10.60	181.18	174.12	4.54	0.059	0.061	0.025	0.026	1.049
C_1655_0035	8.80	140.80	138.67	3.39	0.063	0.063	0.024	0.024	1.038
C_1655_0036	7.99	209.88	208.64	3.22	0.038	0.038	0.015	0.015	1.036
C_1655_0037	3.90	105.26	102.11	1.71	0.037	0.038	0.016	0.017	1.060
C_1655_0038	2.74	95.35	95.35	0.97	0.029	0.029	0.010	0.010	1.047
C_1655_0039	5.81	140.70	137.21	2.46	0.041	0.042	0.017	0.018	1.045
C_1655_0040	2.65	68.60	67.44	0.34	0.039	0.039	0.005	0.0050	1.041
C_1655_0041	6.33	158.82	157.65	2.02	0.040	0.040	0.013	0.013	1.040
C_1655_0042	3.12	91.95	88.51	0.73	0.034	0.035	0.008	0.0082	1.094

Table 6: *Morphometric properties of craters near the Spirit landing site in Gusev Crater, Mars. d, D, r, and m represent the following parameters in order: depth, diameter, rim height, meters.*

Crater	Area of the crater floor with Bedforms (%)	Bedform Orientation (degrees)
C_1655_0001	28.4	51
C_1655_0002	63.4	73
C_1655_0003	63.4	64
C_1655_0004	45.5	63
C_1655_0005	78.5	66
C_1655_0006	74.6	50
C_1655_0007	84.0	50
C_1655_0009	20.0	53
C_1655_0010	5.6	76
C_1655_0011	22.5	57
C_1655_0012	45.0	55
C_1655_0013	61.8	65
C_1655_0014	69.5	40
C_1655_0015	24.1	51
C_1655_0016	15.9	45
C_1655_0017	90.3	60
C_1655_0018	85.7	64
C_1655_0019	94.2	53
C_1655_0020	100	54
C_1655_0021	92.3	59
C_1655_0022	76.3	73
C_1655_0023	92.4	45
C_1655_0024	36.4	61
C_1655_0025	79.3	58
C_1655_0026	60.7	56
C_1655_0027	55.2	48
C_1655_0028	89.4	68
C_1655_0029	13.4	81
C_1655_0030	78.5	43
C_1655_0031	84.1	45
C_1655_0032	0.0	-
C_1655_0033	78.2	29
C_1655_0034	46.6	61
C_1655_0035	100	75
C_1655_0036	14.5	57
C_1655_0037	6.8	92
C_1655_0038	0.0	-
C_1655_0039	17.3	51
C_1655_0040	9.9	53
C_1655_0041	3.3	76
C_1655_0042	20.8	76

Table 7: *Characteristics of bedforms within craters near the Spirit landing site in Gusev Crater, Mars.*

Crater	Depth (m)	Reattachment Length (m)	Reattachment Length (% of Crater Diameter)	Reattachment Length/Depth
C_1655_0001	5.80	39	33.20	6.72
C_1655_0002	5.00	56	60.77	11.20
C_1655_0003	7.80	60	48.22	7.69
C_1655_0004	8.80	71	53.56	8.07
C_1655_0005	5.30	57	73.03	10.75
C_1655_0006	9.80	91	63.93	9.29
C_1655_0007	12.90	82	45.56	6.36
C_1655_0009	6.30	44	37.53	6.98
C_1655_0010	3.85	0	0.00	0.00
C_1655_0011	6.18	42	31.67	6.80
C_1655_0012	6.00	41	40.57	6.83
C_1655_0013	8.50	53	37.54	6.24
C_1655_0014	6.90	65	55.25	9.42
C_1655_0015	4.30	26	28.72	6.05
C_1655_0016	5.20	76	85.95	14.62
C_1655_0017	6.10	69	85.17	11.31
C_1655_0018	5.60	75	90.32	13.39
C_1655_0019	5.00	55	83.56	11.00
C_1655_0020	4.45	68	98.75	15.28
C_1655_0021	3.50	52	87.94	14.86
C_1655_0022	3.90	50	77.68	12.82
C_1655_0023	7.40	101	82.64	13.65
C_1655_0024	3.80	29	37.55	7.63
C_1655_0025	4.50	60	84.75	13.33
C_1655_0026	3.10	26	47.93	8.39
C_1655_0027	3.20	30	56.25	9.38
C_1655_0028	6.70	82	84.93	12.24
C_1655_0029	6.80	23	17.76	3.31
C_1655_0030	4.80	64	83.86	13.33
C_1655_0031	3.90	46	86.26	11.79
C_1655_0032	4.10	0	0.00	0.00
C_1655_0033	11.10	94	57.90	8.47
C_1655_0034	10.60	94	53.99	8.87
C_1655_0035	8.80	124	89.42	14.09
C_1655_0036	7.99	51	24.44	6.38
C_1655_0037	3.90	0	0.00	0.00
C_1655_0038	2.74	0	0.00	0.00
C_1655_0039	5.81	29	21.14	4.99
C_1655_0040	2.65	0	0.00	0.00
C_1655_0041	6.33	24	15.22	3.79
C_1655_0042	3.12	21	23.73	6.73

Table 8: *Flow reattachment lengths within craters near the Spirit landing site in Gusev Crater, Mars.*